1983

The reduction of nitric oxide with carbon monoxide on the Rh(100) single crystal surface

Ronald Eugene Hendershot
Iowa State University

Recommended Citation

Hendershot, Ronald Eugene, "The reduction of nitric oxide with carbon monoxide on the Rh(100) single crystal surface " (1983). *Retrospective Theses and Dissertations*. 8477.
https://lib.dr.iastate.edu/rtd/8477

INFORMATION TO USERS

This reproduction was made from a copy of a document sent to us for microfilming. While the most advanced technology has been used to photograph and reproduce this document, the quality of the reproduction is heavily dependent upon the quality of the material submitted.

The following explanation of techniques is provided to help clarify markings or notations which may appear on this reproduction.

1. The sign or "target" for pages apparently lacking from the document photographed is "Missing Page(s)". If it was possible to obtain the missing page(s) or section, they are spliced into the film along with adjacent pages. This may have necessitated cutting through an image and duplicating adjacent pages to assure complete continuity.
2. When an image on the film is obliterated with a round black mark, it is an indication of either blurred copy because of movement during exposure, duplicate copy, or copyrighted materials that should not have been filmed. For blurred pages, a good image of the page can be found in the adjacent frame. If copyrighted materials were deleted, a target note will appear listing the pages in the adjacent frame.
3. When a map, drawing or chart, etc., is part of the material being photographed, a definite method of "sectioning" the material has been followed. It is customary to begin filming at the upper left hand corner of a large sheet and to continue from left to right in equal sections with small overlaps. If necessary, sectioning is continued again—beginning below the first row and continuing on until complete.
4. For illustrations that cannot be satisfactorily reproduced by xerographic means, photographic prints can be purchased at additional cost and inserted into your xerographic copy. These prints are available upon request from the Dissertations Customer Services Department.
5. Some pages in any document may have indistinct print. In all cases the best available copy has been filmed.

University
Microfilms
International

300 N. Zeeb Road
Ann Arbor, MI 48106

8407076

Hendershot, Ronald Eugene

THE REDUCTION OF NITRIC OXIDE WITH CARBON MONOXIDE ON THE RHODIUM(100) SINGLE CRYSTAL SURFACE

Iowa State University PH.D. 1983

University
Microfilms
International 300 N. Zeeb Road, Ann Arbor, MI 48106

The reduction of nitric oxide with carbon monoxide on the Rh(100) single crystal surface

by

Ronald Eugene Hendershot

A Dissertation Submitted to the
Graduate Faculty in Partial Fulfillment of the
Requirements for the Degree of
DOCTOR OF PHILOSOPHY

Department: Chemistry
Major: Physical Chemistry

Approved:

Signature was redacted for privacy.

In Charge of Major Work

Signature was redacted for privacy.

For the Major Department

Signature was redacted for privacy.

For the Graduate College

Iowa State University
Ames, Iowa

1983

TABLE OF CONTENTS

INTRODUCTION

The reduction of nitric oxide emissions plays a key role in our efforts to improve air quality. The primary sources of nitric oxide are combustion processes. The nitric oxide produced in this manner is partially converted to nitrogen dioxide by reaction with atmospheric oxygen. It is this mixture of nitric oxide and nitrogen dioxide which is usually denoted as NO_x. The two main sources of nitric oxide production are gasoline powered automobiles and electric power stations (1). The total man-made emission of nitric oxide amounts to 53×10^6 tons/year, and this should be compared to the amount of nitric oxide produced naturally by biological action, which is 501×10^6 tons/year (2). The problem occurs when large amounts of nitric oxide are produced in a small local environment, such as that produced by automobiles in an urban location. Once produced, this NO_x interacts with other pollutants typically found in an urban environment, such as hydrocarbons and sulfur dioxide, and sunlight, resulting in photochemical smog.

This effect has led to a series of legislative decisions culminating in the Clean Air Act of 1970, which dictated a 90% reduction in emissions by 1975. These laws produced a vast amount of catalyst research, in an effort to discover a catalytic system efficient enough to remove carbon monoxide, nitric oxide, and unburned hydrocarbons from automobile and smokestack emissions. As a means to this end, literally thousands of materials have been tested for catalytic activity, under countless sets of initial conditions. This effort has revealed that, with respect to the reduction of nitric oxide, the transition metal oxides and the noble metals have the most catalytic activity. The current problem is that, of these two classes of catalysts, only the noble metals are effective enough, in terms of both activity and selectivity, to be used in a practical catalytic converter. These materials are extremely expensive, and the only known sources of significant supply are South Africa and the USSR. There is clearly a need to develop alternative processes, most probably catalytic, which will reduce nitric oxide emissions without relying on noble metal catalysts. In addition to these problems, the catalytic converters currently in use will not operate in a feedstream that contains an excess of oxygen (3). This limitation renders even noble metal catalytic systems unable to reduce nitric oxide emissions from diesel engines, nonnuclear power plants, or industrial furnaces.

The solution to this problem has evaded the best efforts of thousands of researchers, and is not due to a lack of effort so much as to a lack of fundamental understanding of the basic chemical processes involved in the reduction of nitric oxide. In particular, the best catalyst for the reduction of nitric oxide emissions, from a practical standpoint, is rhodium metal (4). Yet, there has been comparatively little research directed at the fundamental processes occurring during the reduction of nitric oxide to nitrogen on rhodium catalysts. It is clear that the shot-gun approach to finding a catalytic solution to the nitric oxide reduction problem (i.e., the random testing of catalysts from the pool of known substances) should be replaced by directed efforts at understanding the fundamental processes involved in the reduction of nitric oxide. This work, therefore, was motivated by this lack of fundamental understanding of nitric oxide reduction processes on rhodium catalysts.

The objective of this work is to develop a fundamental understanding of the reduction of nitric oxide on rhodium metal. The typical exhaust stream contains many components other than nitric oxide; these include carbon monoxide, hydrogen, water, hydrocarbons, oxygen, nitrogen, and carbon dioxide (5). This large number of components, the relatively high temperatures of exhaust streams (320-800°C (5)), and a noble metal catalyst (such as rhodium), leads to a complicated interrelated set of chemical reactions. In an effort to characterize this system, it is necessary to first study its component parts. This work was, therefore, directed toward understanding the mechanism of the reduction of nitric oxide with carbon monoxide on a well-characterized single crystal rhodium surface. The balanced chemical equations relevant to this investigation are:

$$2\ NO + 2\ CO \Longleftrightarrow N_2 + 2\ CO_2 \qquad (1)$$

$$2\ NO + CO \Longleftrightarrow N_2O + CO_2 \quad . \qquad (2)$$

This study utilized several techniques, including steady-state kinetics, thermal desorption spectroscopy (TDS), low energy electron diffraction (LEED), and Auger electron spectroscopy (AES). The main objective of this work is the development of a mechanism for the reduction of nitric oxide with carbon monoxide on the Rh(100) single crystal surface, that is consistent with the global steady-state kinetics. The above surface spectroscopies will be used to characterize the interaction of the reactants and products with the catalyst surface.

LITERATURE REVIEW

This literature review has been divided into two sections. The first section reviews the current understanding of the adsorption-desorption processes, of the reactants and the products, in the reaction between nitric oxide and carbon monoxide. It has been the accumulated experience of scientists who study heterogeneous catalytic reactions, that the chemisorption of at least one of the reactants is an important first step in the catalytic process. It is for this reason, that it is important to first understand the adsorption-desorption processes, that occur during the reduction of nitric oxide with carbon monoxide. The second section reviews the current understanding of the mechanism of the reduction of nitric oxide with carbon monoxide. This latter review will show that no mechanism for the reduction of nitric oxide with carbon monoxide on rhodium metal is well established.

Reactant/Product-Catalyst Interactions

The adsorption of nitric oxide on rhodium surfaces has been extensively reported in the literature. These studies have included both well-characterized single crystal surfaces and supported catalysts, and have utilized a number of surface analysis techniques. In particular, the chemisorption of nitric oxide has been studied on polycrystalline rhodium wire (6), and the Rh(100) (7), Rh(111) (7), Rh(110) (8), Rh(331) (9,10), and Rh(755) (9) single crystal surfaces. These studies have utilized a variety of surface techniques, including Auger electron spectroscopy (AES), low energy electron diffraction (LEED), x-ray photoelectron spectroscopy (XPS), and thermal desorption spectroscopy (TDS). In addition to these studies, the chemisorption of nitric oxide has been studied on supported rhodium catalysts, for example, Rh/Al_2O_3 (11-15), Rh/SiO_2 (15), and Rh/TiO_2 (15). These studies have utilized infrared spectroscopy (IR) and inelastic electron tunneling spectroscopy (IETS). The general result of these studies is that nitric oxide adsorption is dissociative on rhodium surfaces at low coverages, and molecular at higher coverages. Since, as mentioned above, the adsorption-desorption phenomena of nitric oxide have been reviewed previously for transition metals (1,4,16), only a brief summary of the adsorption behavior of nitric oxide on rhodium metal will be given in this review.

The adsorption of nitric oxide at 330 K on polycrystalline rhodium wire has been studied by Campbell and White (6). These authors report experiments utilizing flash desorption spectroscopy (FSD). They report that after clean rhodium was exposed to NO(g) at 330 K, three species, namely N_2, O_2, and NO, desorbed from the surface during the thermal desorption experiment. The molecular nitric oxide did not appear in the TDS spectrum until very high exposures, on the order of 1.0 Langmuir (L) (i.e., 1.0 Langmuir = 1.3332×10^{-4} Pa sec), and this peak reached a maximum at 430 K. Molecular oxygen desorbed in a broad single peak, which reached a maximum at about 1000 K. At a saturation exposure of nitric oxide, about 2.25 L, nitrogen desorbed in a broad peak, which consisted of desorption from two distinct surface states, with the indication of a third state as a high temperature shoulder. The two states were denoted as β_1 and β_2, and reached maxima at 480 K and 650 K, respectively. The β_2 state populated prior to the β_1 state, which appeared at the same coverage as the molecular nitric oxide peak, at 430 K. No order analysis was performed, because the nitrogen desorption spectra were obtained from the less intense nitrogen peak, at m/e = 14, instead of the molecular nitrogen peak at m/e = 28, due to interferences from background carbon monoxide, also at m/e = 28. In addition to the intensity problems associated with the m/e = 14 mass spectrometer peak, the nitrogen desorption peak, as measured by the m/e = 14 peak, was adjusted to take into account the overlapping cracking fragment from molecular nitric oxide, which also occurs at m/e = 14. This procedure yields peak shapes with considerable error, and precludes an order analysis (6).

The extent of dissociation is difficult to measure from the peak areas of thermal desorption spectra, because dissociation is most probably occurring during the flash in temperature. Campbell and White (6) estimated the extent of dissocation of nitric oxide on polycrystalline rhodium wire, by titrating a saturated nitric oxide overlayer with carbon monoxide at 330 K. This procedure produced a small carbon dioxide transient peak. After measuring mass spectrometer sensitivity, and the system pumping speed for carbon dioxide, the amount of O (ads) can be calculated. The result of this analysis indicated that, at saturation exposure of nitric oxide, approximately 30% of the adsorbed nitric oxide had dissociated, and the remaining 70% exists as molecular nitric oxide on the polycrystalline rhodium wire sample (6).

The adsorption of nitric oxide on the Rh(100) and Rh(111) single crystal surfaces has been reported by Castner et al. (7). On the Rh(100) surface, nitric oxide adsorbs with a high sticking probability, and forms a c(2 x 2) ordered overlayer. Two ordered overlayers were reported on the Rh(111) surface. At exposures greater than 0.1 L, and less than 1.0 L, nitric oxide formed a c(4 x 2) structure which transformed into a p(2 x 2) ordered overlayer at exposures greater than 1.0 L (7). These authors comment that the thermal desorption spectra of adsorbed nitric oxide from these surfaces was "complex", and they did not report these results (7).

The adsorption of nitric oxide on the Rh(110) surface has been studied utilizing TDS, AES, LEED, and XPS by Baird et al. (8). These authors report that nitric oxide is chemisorbed dissociatively on the Rh(110) surface for exposures less than 0.5 L, forming an ordered (2 x 1) overlayer. This pattern reached maximum intensity at 0.5 L exposure. A XPS analysis of this overlayer yielded one principal peak at 397.4 eV, in the N 1s region, and a broad peak centered at 530.5 eV, in the oxygen 1s region. These peaks were assigned to atomic nitrogen and oxygen from dissociatively chemisorbed nitric oxide (8). At exposures greater than 0.5 L, the background intensity of the (2 x 1) LEED pattern increased, and several new features appeared in the XPS spectrum. Specifically, a broad peak appeared at about 400.0 eV, in the nitrogen 1s region, and the oxygen 1s peak at 530.5 eV exhibited an increase in intensity at 531 eV. In addition to these new features in the XPS spectrum, a UPS analysis showed three new peaks at 14.5, 9.2, and 2.5 eV below the Fermi level. These new UPS and XPS features were attributed to molecular nitric oxide adsorption (8). The UPS peaks at 14.5, 9.2, and 2.5 eV were assigned to the 4σ, 1π - 5σ, and $2\pi^*$ molecular orbitals of nondissociatively chemisorbed nitric oxide (8). The thermal desorption spectra reported for the Rh(110) surface are similar to the TDS results reported for polycrystalline rhodium wire (6), as discussed previously. At exposures of 0.5 L or less, no molecular nitric oxide desorbed during the thermal desorption experiment, and the molecular nitrogen desorption peak reached a maximum at 613 K (8). This peak decreased in intensity as exposure was increased above 0.5 L, and peaks at 468 K and 523 K gradually increased in intensity, reaching maximum peak areas at about 10 L. This effect is attributed to the hindering of dinitrogen formation at low exposures of nitric oxide by adsorbed oxygen; thus, the unusually high T_{max} value for molecular nitrogen desorption at low coverages (8). At saturation exposure of nitric oxide on the Rh(110) surface, a flash desorption experiment yielded three desorption products. The first, a molecular nitric oxide peak, reached a maximum at about 433 K, and was quite low in intensity. The second desorption product was molecular nitrogen, and had peaks with maxima at 468 K and 523 K. The last desorption product was molecular oxygen, which desorbed in a broad peak centered at 1073 K (8). The molecular nitrogen peak at 468 K was attributed to the decomposition, during the flash desorption experiment, of molecularly adsorbed nitric oxide. This interpretation also accounted for the low intensity of the molecular nitric oxide peak (8). This evidence clearly illustrates that nitric oxide is dissociatively adsorbed at low coverages, and molecularly adsorbed at high coverages on the Rh(110) surfaces.

The behavior of nitric oxide adsorption on stepped rhodium surfaces followed the same pattern as that established for polycrystalline rhodium wire and the Rh(110) single crystal surface. On the Rh(331) surface, no ordered overlayers were formed after adsorption of nitric oxide at room temperature (9). However, a (2 x 2) ordered overlayer formed upon nitric oxide adsorption on the Rh(755) surface at room temperature (9). This overlayer was similar to the (2 x 2) ordered overlayer, discussed previously, on the Rh(111) surface (7) and, thus, was assumed to represent ordering on the (111) terraces of the Rh(755) surface (9). Thermal desorption results reported for the Rh(331) and Rh(755) stepped surfaces (9) are similar to those discussed above for the Rh(110) surface (8). For these stepped surfaces, no molecular nitric oxide desorbed during the thermal desorption experiments for exposures less than 1 L. At saturation coverage, nitric oxide exhibited a first order desorption peak at 175°C, and a low temperature peak at 150°C (9). The low temperature desorption peak was not detected until the (2 x 2) structure had formed. Castner and Somorjai (9) also reported the desorption of nitrous oxide (i.e., N_2O, m/e = 44) from the Rh(755) surface after low nitric oxide exposures. At exposures less than 0.5 L, nitrous oxide desorbed in a second order peak at about 210°C, and at higher exposures of nitric oxide, on the order of 1.0 L, a second nitrous oxide desorption peak appeared at about 150°C (9). These authors comment that the low temperature desorption peaks, for both molecular nitrogen and nitrous oxide, occur at the same exposure which results in the appearance of the molecular nitric oxide desorption peak, but draw no other conclusions concerning the origin of the unusual nitrous oxide desorption peaks (9). These results lead to the conclusion that nitric oxide adsorbs dissociatively on the Rh(331) and Rh(755) surfaces at exposures below 1 L, and associately adsorbs on these surfaces at exposures above 1 L.

The chemisorption of nitric oxide on the Rh(331) stepped surface was examined in a later study by Dubois, using AES and high resolution electron energy loss spectroscopy (HREELS) (10). The HREELS spectrum taken after the adsorption of 1 L of nitric oxide on the Rh(331) surface showed three energy loss peaks. These peaks appear at 403, 1704, and 1815 cm^{-1}, and their relative position and intensity was found to be independent of gas exposure from 0.1 to 10.0 L (10). The loss peaks were assigned to molecular chemisorbed nitric oxide. The loss peak at 1704 cm^{-1} was assigned to the N-O stretching vibration of a molecularly adsorbed nitric oxide, with the Rh-N=O bond being bent relative to the surface normal (10). The loss at 1815 cm^{-1} was assigned to a linear nitrosyl species, and the loss at 403 cm^{-1} was assigned to the Rh-N bending mode, characteristic of an associatively adsorbed species in a bent configuration (10). Absent from the HREELS spectrum, taken after a 1 L exposure of nitric oxide at room temperature, is any loss feature characteristic of a rhodium-oxygen interaction. This implies that nitric oxide does not dissociate upon adsorption at room temperature on the Rh(331) surface. After a 1 L exposure of NO, the sample was flashed to

450 K, the molecularly adsorbed nitric oxide dissociated, and the surface nitrogen desorbed as molecular nitrogen, leaving behind a surface oxide (10). This was confirmed by both HREELS and AES. This surface oxide had an energy loss peak at 520 cm^{-1}, which was extremely similar to the energy loss feature produced by a surface oxide, formed by a 1 L exposure of oxygen at 300 K to the Rh(331) surface (10). These results clearly indicate that nitric oxide molecularly adsorbs on the Rh(331) surface, at room temperature, and dissociates only upon heating the sample to 450 K. This conclusion is in contrast to the results of nitric oxide adsorption study on the Rh(331) surface, as reported by Castner and Somorjai (9).

The interaction of nitric oxide with supported rhodium catalysts has been reported previously (11-15). These studies have utilized infrared spectroscopy (IR) and inelastic electron tunneling spectroscopy (IETS) to examine the interaction of nitric oxide with rhodium supported on various transition metal oxides, predominantly Al_2O_3. While the sensitivity and spectral range of the IR technique is limited with respect to surface analysis, as compared to HREELS, useful information concerning the interaction of nitric oxide with the rhodium catalyst is still obtainable.

The adsorption of nitric oxide on alumina-supported rhodium has been examined by several groups (11-14). Arai and Tominaga (14) examined the adsorption of nitric oxide at a pressure of 6.6×10^3 Pa, and at several temperatures. They reported that room temperature adsorption of nitric oxide yields two intense absorption bands, at 1830 and

1740 cm^{-1}, and a weak band at 1910 cm^{-1}. As the adsorption temperature was increased, the first two bands decreased in intensity, while the weak band, at 1910 cm^{-1}, increased dramatically in intensity. These bands, at 1910, 1830, and 1740 cm^{-1}, were assigned to adsorbed Rh-NO^+, Rh-NO, and Rh-NO^- species, respectively. Identical results were published by Solymosi and Sarkany (11). Since the spectral range of the IR technique, as applied to adsorbates on supported metal catalysts, is limited to frequencies greater than 1200 cm^{-1}, the question of dissociative chemisorption could not be addressed.

The adsorption of nitric oxide on Rh/Al_2O_3 has also been studied using IETS, and a preliminary report was published by Cheveîgne et al. (13). The advantage of this technique is its wide spectral range (200-4000 cm^{-1}), and its resolution (<4 cm^{-1}), but this technique suffers from two severe disadvantages. First, spectra must be recorded with the sample at 4.2 K or less, and second, a counter electrode, typically lead, must be deposited over the adsorbed overlayer. The effects of these two constraints on the state of the adsorbate is a subject of controversy. Cheveigne et al. (13) reported that, after adsorption of nitric oxide during the evaporation of a 25 Å rhodium substrate, no molecularly adsorbed nitric oxide could be detected. These authors were able to detect and assign the Rh-N stretch at 460 cm^{-1}, which they claim originated from the dissociative chemisorption of nitric oxide. They comment that the lack of the expected Rh-O stretch at 520 cm^{-1} (10) was due to the reaction of this species with background carbon monoxide to form carbon dioxide, which subsequently desorbed (13).

The effect of the catalyst support on the adsorption of nitric oxide has been reported by Rives-Arnau and Munuera (15). These authors examined two supports, namely SiO_2 and TiO_2. They found that the adsorption of nitric oxide was strongly affected by the nature of the support material. On Rh/TiO_2, the 300 K adsorption isotherm for nitric oxide showed dramatically greater adsorption than that on Rh/SiO_2 (15). The infrared analysis of nitric oxide adsorbed on Rh/SiO_2 showed a weak band at 1720 cm^{-1}; due to support interferences, bands in the range of 2000-1800 cm^{-1} could not be detected. The band at 1720 cm^{-1} was assigned to a $Rh\text{-}NO^-$ species, in agreement with the results discussed previously (11,14). On the Rh/TiO_2 catalyst, nitric oxide adsorption produced bands at 1815 and 1900 cm^{-1}. The low intensity of these bands, despite the fact that the amount of nitric oxide adsorbed on the Rh/TiO_2 catalyst was much greater than on the Rh/SiO_2 catalyst, led these authors to conclude that a dissociative adsorption of nitric oxide was occurring on the Rh/TiO_2 catalyst, promoted by the strong metal-support interactions (SMSI) between the rhodium particles and the TiO_2 support (15). This (SMSI) effect is usually rationalized as leading to an increase in the electron donor capacity of the rhodium particles, which in turn weakens the N-O bond of the adsorbate, via backbonding of the metal d-electrons into the anti-bonding orbitals of the adsorbate, thus enhancing dissociation of the adsorbed nitric oxide (15).

Thus, the general trend for chemisorption of nitric oxide on rhodium surfaces is dissociative adsorption at low coverages, followed by molecular adsorption at higher coverages. The extent of dissociation depends upon the temperature and the surface structure of the rhodium metal. This behavior is exactly the expected result based upon the position of rhodium in the periodic table. Broden et al. (17) has recently interpreted this trend semiquantitatively for the adsorption behavior of carbon monoxide, nitrogen, and nitric oxide, in terms of the energy separation of the 1π and 4σ levels in the adsorbed diatomic molecule, as measured by UPS. In addition to this analysis, the calculations of Miyazaki and Yasumori (18) also support this general trend of adsorption behavior of nitric oxide on rhodium metal. Periodic trends of chemisorption on transition metal surfaces have also been investigated by Benziger (19). This author examined the thermodynamic effects of adsorption, via heats of formation, of transition metal nitrides, carbides, and oxides. Using this approach, Benziger (19) was also able to correlate the position of a metal in the periodic table, with the type of adsorption, molecular versus dissociative, for nitric oxide, nitrogen, and carbon monoxide.

The interaction of carbon monoxide with transition metals is one of the most studied adsorbate-surface systems in surface science. In particular, the adsorption of carbon monoxide on rhodium metal has been studied extensively, and was most recently reviewed by Dubois and Somorjai (20). The adsorption of carbon monoxide has been recently studied on supported rhodium catalysts (11,12,14,15,21,22), polycrystalline rhodium wire (6,23,24), and on the Rh(100) (7,25), Rh(110) (8), Rh(111) (7,20,26-30), Rh(331) (9,10), and Rh(755) (9) single crystal surfaces. Since the adsorption of carbon monoxide on rhodium metal has been reviewed recently (20), only those results pertinent to this study will be discussed in the following section.

The adsorption-desorption behavior of carbon monoxide on polycrystalline rhodium wire has been most recently reported by Campbell and White (24). These authors found that carbon monoxide adsorbs with simple, first order Langmuir-type kinetics, with an initial sticking probability of 0.5 at 300 K (24). Thermal desorption experiments showed that the desorption of carbon monoxide from polycrystalline rhodium wire was kinetically first order in adsorption density, with an activation energy for desorption of 134 kJ/mole, assuming a value for the pre-exponential factor of 10^{13} sec^{-1} (24). These authors thoroughly examined the adsorption-desorption processes, at several temperatures, in an attempt to find evidence for dissociation of carbon monoxide on their polycrystalline rhodium wire surface. The results of these experiments indicate that dissociation of carbon monoxide on polycrystalline rhodium wire is not an important process (24).

The adsorption of carbon monoxide on the Rh(100) and Rh(111) single crystal surfaces has been extensively studied by several authors (7, 20,25,26-30). Castner, Sexton, and Somorjai reported a series of carbon monoxide ordered overlayers, on both the Rh(100) and Rh(111) surfaces (7). On both surfaces, carbon monoxide forms an initial ordered overlayer at low coverage, with this overlayer compressing, at higher coverages, into an ordered structure with hexagonal symmetry. In particular, on the Rh(111) surface, carbon monoxide forms a $(\sqrt{3} \times \sqrt{3})R30°$ ordered overlayer at an exposure of 0.5 L (7). This overlayer corresponds to a coverage of approximately 1/3 of a monolayer of carbon monoxide. Koestner et al. (27) examined the structure of the $(\sqrt{3} \times \sqrt{3})R30°$ ordered overlayer, by measuring intensity versus beam voltage profiles for several independent diffraction events. Utilizing a dynamical LEED formalism, these authors determined that the $(\sqrt{3} \times \sqrt{3})R30°$ ordered overlayer corresponded to carbon monoxide adsorbed perpendicular to the surface, with the carbon end down at an atop site (27). The overlayer interatomic distances were found to be d(Rh-C) = 1.95 ± 0.1 Å, and d(C-O) = 1.07 ± 0.1 Å (27). At carbon monoxide coverages between 1/3 and 3/4, a structure designated a "split" (2 x 2) formed, which is an overlayer with hexagonal symmetry (7). Finally, at saturation coverage of about 3/4, a compressed hexagonal overlayer with true (2 x 2) symmetry formed on the Rh(111) surface (7). These three ordered overlayers were subsequently examined by Dubois and Somorjai (20) utilizing HREELS. These authors report that at low coverages, carbon monoxide bonds, carbon end down, linearly, atop individual rhodium atoms, with ν(Rh-C) = 480 cm^{-1} and ν(C-O) = 1990 cm^{-1} (20). At higher coverages, a bridge bonded species forms, with ν(Rh-C) = 400 cm^{-1} and ν(C-O) = 1870 cm^{-1}, and this species appears at the same coverage corresponding to the "split" (2 x 2) LEED pattern on the Rh(111) surface (7,20). At saturation coverage of carbon monoxide (i.e., $\theta = 0.75$; (2 x 2) LEED pattern), the ratio of atop to bridged carbon monoxide is approximately 2:1, as calculated from peak area ratios in the HREELS spectrum (20). Thermal desorption analysis at saturation coverage yields two desorption peaks that differ in binding energy to the surface by approximately

4 kcal/mole, with the bridge bonded species being the state with the lower binding energy (20).

Similar results have been reported for the Rh(100) surface (7,25). At low coverages, a c(2 x 2) ordered overlayer forms on the Rh(100) surface, and a single peak was observed in the thermal desorption spectrum. At exposures above 1 L, a compressed hexagonal "split" (2 x 1) ordered overlayer forms, and a second peak, with lower binding energy, appears in the thermal desorption spectrum (7). This second peak is presumably due to the formation of a bridge bonded species on the Rh(100) surface. A preliminary HREELS study, reported by Dubois (25), also found evidence for two forms of carbon monoxide bonding to the Rh(100) surface. Dubois reported Rh-CO stretching vibrations at 358 and 428 cm^{-1}, and C-O stretching vibrations at 1920 and 2030 cm^{-1}, for carbon monoxide adsorbed in the bridge and linear atop sites, respectively (25). Thermal desorption from the Rh(100) and Rh(111) surface yielded peaks corresponding only to molecularly adsorbed carbon monoxide, and no evidence for dissociation of the carbon monoxide molecule, on these surfaces, was reported (7,20,25).

The adsorption of carbon monoxide on the Rh(110) surface has been studied, utilizing XPS, UPS, LEED, and TDS (8,31). Exposure of the Rh(110) surface to carbon monoxide yielded a (2 x 1) LEED pattern (8). The XPS spectrum for this adsorbate showed two peaks in the carbon 1s region, at 285.4 and 283.4 eV, while the oxygen 1s region contained a single peak at 531.3 eV. The UPS spectrum contained two strong peaks at 7.6 and 10.6 eV below the Fermi level, and these were assigned to the

4σ and 1π - 5σ molecular orbitals of molecularly adsorbed carbon monoxide (8). Thermal desorption experiments yielded a single desorption peak at low coverage, located at 240°C. At higher coverages, this peak broadened on the low temperature side, possibly indicating population of a second adsorption site (8).

The adsorption of carbon monoxide has also been examined on stepped rhodium single crystal surfaces. Castner and Somorjai (9) examined the adsorption of carbon monoxide on the Rh(755) and Rh(331) single crystal surfaces with AES, LEED, and TDS. On the Rh(755), surface carbon monoxide forms a $(\sqrt{3} \times \sqrt{3})R30°$ structure on the (111) terraces, at a 3 L exposure (9). After increasing the background pressure to 1.3×10^{-3} Pa, a (2 x 2) structure forms on the (111) terraces. Thermal desorption spectra were the same for both the Rh(331) and Rh(755) surfaces, and were similar to the desorption from the Rh(111) and Rh(100) surfaces (7,9). Using AES, together with TDS, these authors reported that a carbon residue was left on the surface after the normal desorption of molecular carbon monoxide (9). This carbon remained on the surface until 800°C, at which time it diffused into the bulk. After pretreatment of these surfaces with oxygen (1.3×10^{-4} Pa O_2, 800°C), the residual surface carbon desorbed as carbon monoxide, between 500 to 600°C (9). Castner and Somorjai (9) claim that this residual carbon is due to dissociated carbon monoxide, produced by the step atoms, during the flash desorption process. Dubois et al. (10) reported HREELS spectra of carbon monoxide adsorbed on the Rh(331) stepped surface. At exposures on the order of 0.1 L of carbon monoxide, the HREELS spectrum showed two energy loss peaks, one at 430 cm^{-1} and the other at 2060 cm^{-1} (10). These losses were assigned to the Rh-CO stretch and the C-O stretch of a linearly bonded carbon monoxide species. At higher exposures, an additional mode appeared at 1930 cm^{-1}, and this was attributed to carbon monoxide molecularly adsorbed at, or near, the step edge (9).

The general behavior of carbon monoxide chemisorbed to transition metals has been recently reviewed by Broden et al. (17). These authors correlate the position of a metal in the periodic table with the ability to dissociatively chemisorb carbon monoxide. It was determined that the electronic nature of the metal itself is the primary factor in determining the nature of the chemisorption, and the metal surface geometry is only a second order effect (17). In other words, the metal surface geometry is important in determining associative versus dissociative adsorption, only for those metals that border the electronic effect dividing line in the periodic table, for these two modes of chemisorption. For the fifth row elements on the periodic chart, this line lies between ruthenium and technetium. Thus, these authors predict molecular chemisorption on all crystal planes of rhodium metal (17).

The subject of dissociative chemisorption of carbon monoxide on rhodium surfaces is the subject of much controversy (28-30). Yates, Williams, and Weinberg (28) have utilized isotopic mixing, AES, and TDS, to calculate the maximum probability for dissociation to be less than 1×10^{-4} per collision, with the Rh(111) surface in the temperature range between 300 to 870 K. These authors argue that this low probability of dissociation also precludes dissociation on stepped rhodium surfaces, in this temperature range, since this Rh(111) crystal was misaligned by 0.5° (28). Castner et al. (29) subsequently reported TDS experiments on the Rh(111) surface. After annealing an oxygen pre-treated Rh(111) surface in 1.3 x 10^{-5} Pa carbon monoxide at 670 K for 10 minutes, and cooling in vacuum, the TDS spectrum clearly showed evidence for a high temperature carbon monoxide desorption peak (29). It is this high temperature peak, which is claimed to arise from the recombination of adsorbed atomic carbon and atomic oxygen, that indicates dissociation of carbon monoxide. In a reply to the work of Castner et al. (29), Yates, Williams, and Weinberg (30) claim that such a low concentration of atomic carbon is the result of electron beam dissociation of the adsorbed carbon monoxide, in the case of the Rh(331) investigation (9), and due to hydrocarbon impurities, in the case of the TDS experiment on the Rh(111) surface (29). Additional work, based on field emission from a clean rhodium tip, led to estimates that the probability for dissociation per collision on any crystal plane of rhodium is below 1 x 10^{-8} at temperatures up to 1000 K (32). The final outcome of this controversy has yet to be determined.

The adsorption of carbon monoxide on supported rhodium catalysts has also been studied extensively, in particular on Rh/Al_2O_3 (11,12,14, 21,22), Rh/SiO_2 (15), and Rh/TiO_2 (15). These studies have utilized IR spectroscopy. Solymosi and Sarkany (11) examined the adsorption of carbon monoxide on Rh/Al_2O_3 at several temperatures. After adsorption of carbon monoxide at 25°C, bands were observed at 2105, 2035, 1880, 1648, 1452, and 1230 cm^{-1}. The two strongest bands, at 2105 and

2035 cm^{-1}, were about equal in intensity, and were assigned to the twin carbon monoxide (i.e., two CO molecules bonded to the same rhodium atom) asymmetric and symmetric stretches, respectively (11). The band at 1880 cm^{-1} was assigned to a bridge bonded carbon monoxide, and the remaining bands were assigned to C-O stretches in various carbonate species. An additional band appeared at 2073 cm^{-1}, when carbon monoxide was adsorbed at 170°C, and was attributed to a C-O stretch in a carbon monoxide bound linearly to a single rhodium atom (11). Rives-Arnau and Munuera (15) examined metal support interactions and their effect on carbon monoxide chemisorption. The adsorption isotherms for carbon monoxide on the Rh/SiO_2 and Rh/TiO_2 were identical (15). Analysis of carbon monoxide adsorption with IR revealed a strong band at 2070 cm^{-1} on Rh/SiO_2 and 2020 cm^{-1} on Rh/TiO_2. These bands were assigned to a carbon monoxide bound linearly to a single rhodium atom (15). Solymosi and Erdohelyi (21) examined the adsorption of carbon monoxide on Rh/Al_2O_3, with a pulsed micro-catalytic system, in order to determine the extent of dissociative adsorption. They concluded that carbon monoxide does dissociate on supported rhodium, however, the extent of dissociation is less than that which occurs on supported Ni or Fe catalysts (21).

In general, the adsorption of carbon monoxide on well-characterized rhodium surfaces (i.e., foil, wire, single crystal surface) is primarily molecular. The adsorption occurs generally in two sites, namely linear atop sites and bridge sites. The atop adsorption state is populated first during the adsorption process, followed by population of the bridged bonded state. These states differ in binding energy by 4 kcal/mole. On rhodium metal surfaces, the extent of carbon monoxide dissociation is quite small, and its occurrence is still the subject of controversy. On supported catalysts, several other modes of adsorption have been observed, with the twin mode being dominant on Rh/Al_2O_3. The dissociation of carbon monoxide on supported rhodium is a significant process (21), and a comparison between Rh/SiO_2 and Rh/TiO_2 catalysts indicates that carbon monoxide adsorption does not show a strong metal support interaction (15).

The adsorption of carbon dioxide has been studied on polycrystalline rhodium wire (24), and the Rh(111) (7,20), Rh(100) (7), Rh(331) (9), and Rh(755) (9) single crystal surfaces. These studies utilized the usual surface analysis techniques. In addition to these results, the adsorption of carbon dioxide on Rh/Al_2O_3 catalysts has also been examined utilizing IR spectroscopy (11,12). After adsorption of carbon dioxide on Rh/Al_2O_3, IR bands appeared at 1660, 1465, and 1232 cm^{-1} (11). The first two bands were assigned to carbonate species, and the source of the last band is unclear (11).

In general, the absorption-desorption characteristics of carbon dioxide are similar to those of carbon monoxide. For example, on both the Rh(111) and Rh(100) surfaces, carbon dioxide formed the same series of ordered overlayers as those formed by carbon monoxide, except that carbon dioxide required a 5-10 fold higher exposure to form the same ordered overlayer (7,20). Carbon dioxide dissociatively chemisorbed into adsorbed carbon monoxide and adsorbed oxygen ad-atoms on the Rh(111) and Rh(100) surfaces (7). Thermal desorption analysis of the carbon dioxide adsorbate gave the same results as carbon monoxide desorption, except for the factor of 5-10 higher exposure necessary for carbon dioxide. During the TDS experiments, carbon monoxide was the only gas detected desorbing from the surface (7). The adsorbed oxygen ad-atoms are believed to diffuse into the bulk (7), a process that has been shown to occur on the Rh(111) surface at temperatures above 400 K (33). Additional evidence for the dissociation of carbon dioxide on Rh(111) surfaces was reported by Dubois and Somorjai (34). These authors utilized isotopically labeled $^{13}CO_2$, with HREELS and TDS, to demonstrate that carbon dioxide dissociatively chemisorbs on rhodium surfaces.

The adsorption of carbon dioxide on stepped rhodium surfaces follows the same pattern as the chemisorption on flat rhodium surfaces. Carbon dioxide dissociatively chemisorbs on the Rh(331) and Rh(755) single crystal surfaces into adsorbed carbon monoxide and adsorbed oxygen ad-atoms (9). Both CO and CO_2 formed an identical series of LEED patterns, as a function of exposure, except for the 5 fold higher exposure necessary for carbon dioxide. As reported previously for Rh(111) and Rh(100) (7), no carbon dioxide was detected during thermal desorption experiments on the Rh(331) and Rh(755) surfaces, after any exposure to carbon dioxide (9). Thermal desorption spectra, taken after various carbon dioxide exposures, yielded two desorption peaks at m/e = 28. The low temperature desorption peak was identical to the carbon monoxide desorption peak found after exposure of the surface to carbon monoxide (9). The high temperature peak, also at m/e = 28, reached a maximum between 500 and 600°C, and was attributed to the recombination of surface carbon and surface oxygen. This desorption peak was observed after carbon dioxide adsorption, but not after carbon monoxide adsorption, and only for the stepped rhodium surfaces. This peak was not observed on the Rh(111) and Rh(100) surface, and provides additional evidence for the dissociation of CO on step sites. Castner and Somorjai (9) suggested that the additional oxygen ad-atom available, after the complete dissociation of adsorbed carbon dioxide, increased the recombination reaction between adsorbed carbon and adsorbed oxygen, to produce the high temperature carbon monoxide desorption peak. These effects suggest that adsorbed oxygen would rather diffuse into the bulk than react with adsorbed carbon, in the case of carbon monoxide adsorption on stepped rhodium surfaces.

The adsorption of carbon dioxide has been examined on polycrystalline rhodium wire (24). These authors utilized thermal desorption spectroscopy, and found that no carbon dioxide desorbed from the surface, after exposures up to 170 L (24). A small carbon monoxide peak was detected, during the flash desorption experiments on the rhodium wire, after exposure of this surface to carbon dioxide, but this was attributed solely to carbon monoxide adsorption from the background gas (24). These authors conclude, therefore, that carbon dioxide does not adsorb on polycrystalline rhodium wire. This result conflicts with the carbon dioxide adsorption results found on rhodium single crystals (7,9,20), and the source of this discrepancy is not clear.

The chemisorption of nitrogen on transition metals has recently been reviewed by Broden et al. (17). It is well-known that molecular nitrogen will not chemisorb on rhodium metal at 300 K (35,36), however, Mimeault and Hansen (35) have shown that thermally activated nitrogen will dissociatively chemisorb on rhodium surfaces. This nitrogen desorbed as N_2, at about 1000 K, and isotopic labeling experiments also indicated that the adsorption was dissociative (35). In a similar experiment, Campbell and White (6) thermally activated nitrogen to examine its adsorption-desorption characteristics on polycrystalline rhodium wire. These authors also report dissociative chemisorption of the thermally activated nitrogen, which desorbed as molecular nitrogen at 670 K during a flash desorption experiment. Dubois et al. (10) subsequently examined the adsorption-desorption properties of molecular nitrogen on the Rh(331) single-crystal surface. These authors were unable to detect adsorption of any nitrogen species, despite the relatively high exposure (i.e., 10^4L), and attempts to activate the nitrogen with ion gauge and mass spectrometer filaments (10). This lack of adsorption on this Rh(331) surface was attributed to the distance between the activation source, and the single crystal surface. In general, however, rhodium metal will not chemisorb molecular nitrogen, at any temperature or pressure (17).

Nitric Oxide Reduction-Mechanistic Studies

The reduction of nitric oxide has been studied extensively in recent years. This effort has utilized numerous techniques, to elucidate details of the mechanism of nitric oxide reduction, under a wide variety of process conditions. From a practical standpoint, the complexity is derived primarily from the large number of components typically present in the exhaust streams. In addition, these exhaust streams are also at relatively high temperatures, which, when coupled with a catalyst, have the potential for a wide variety of processes occurring simultaneously. Unfortunately, one of the most favored processes, in automobile exhausts, is the production of ammonia. This problem, however, can be controlled by careful catalyst design, coupled with stringent control of the air to fuel ratio in automobiles. The general topic of nitric oxide reduction has been recently reviewed by several authors (1,4,16). For this reason, only those studies pertinent to the reduction of nitric oxide with carbon monoxide will be reviewed here.

The nitric oxide molecule is quite unstable, in a thermodynamic sense, with respect to homogeneous decomposition. This is shown in Eq. 3, which has an equilibrium constant of 3×10^5 (4). The stability

$$NO \Longleftrightarrow 1/2\ N_2 + 1/2\ O_2 \qquad (3)$$

of this molecule is derived from the large activation energy (i.e., 335 kJ/mole) necessary for homogeneous decomposition (37). The heterogeneous decomposition of nitric oxide has also been examined over a wide variety of catalysts, typically transition metal oxides (38,39). In general, this reaction involves decomposition of nitric oxide on the transition metal oxide, desorbing molecular nitrogen, leaving adsorbed oxygen. It is this adsorbed oxygen, which requires high temperatures for recombination and desorption, that makes this process generally too slow to be of practical value for most exhaust streams. In the presence of a suitable reductant, however, this oxygen inhibition effect can be overcome.

The heterogeneous catalytic reduction of nitric oxide has been examined over a wide variety of catalysts. These can be classified into two groups, namely, base metal oxides and noble metal catalysts (1). In general, the noble metal catalysts have both higher activity, and greater selectivity towards nitrogen. It is for these reasons that practical automobile catalytic converters are based upon noble metal catalytic systems, and much of the fundamental research has also been directed toward noble metal catalytic reduction of nitric oxide (40-42). Several reductants are commonly available in automotive exhausts, including hydrogen, carbon monoxide, and hydrocarbons. The reduction of nitric oxide with hydrocarbons over most conventional catalysts is much slower than its reduction by other easily available reductants, and so is of little value (16). There are several possible reactions that can occur in the presence of NO, CO, and H_2. The most important reactions, with respect to nitric oxide reduction, are given in equations 4 thru 8. Clearly, Eqs. 4 and 6 are the desired processes. The production of water

$$NO + CO \Longleftrightarrow 1/2\ N_2 + CO_2 \qquad (4)$$

$$2\ NO + CO \Longleftrightarrow N_2O + CO_2 \qquad (5)$$

$$NO + H_2 \Longleftrightarrow 1/2\ N_2 + H_2O \qquad (6)$$

$$2\ NO + 5\ H_2 \Longleftrightarrow 2\ NH_3 + 2\ H_2O \qquad (7)$$

$$2\ NO + H_2 \Longleftrightarrow N_2O + H_2O \qquad (8)$$

from these processes, in the presence of CO, also allows for the water gas shift reaction to occur, as given in Eq. 9. In addition, the

$$CO + H_2O \Longleftrightarrow CO_2 + H_2 \qquad (9)$$

production of ammonia supplies two additional routes for the reduction of nitric oxide, as described in Eqs. 10 and 11.

$$6\ NO + 4\ NH_3 \Longleftrightarrow 5\ N_2 + 6\ H_2O \qquad (10)$$

$$8\ NO + 2\ NH_3 \Longleftrightarrow 5\ N_2O + 3\ H_2O \qquad (11)$$

Kobylinski and Taylor (40) have compared the relative rates of nitric oxide reduction by carbon monoxide, and by hydrogen, over several supported noble metal catalysts. Their results conclusively show that the reduction of nitric oxide with hydrogen is faster than the reduction of nitric oxide with carbon monoxide over supported Pd, Pt, and Rh catalysts (40). Only over supported Ru catalysts was the NO/CO process faster than the NO/H_2 process (40). In addition, ammonia was the major product produced in the reduction of nitric oxide with hydrogen over supported Pt and Pd, presumably via Eq. 7 (40). The supported Rh and Ru catalysts, on the other hand, were more selective in the reduction of nitric oxide, producing more molecular nitrogen, implying the dominance of Eq. 6, or possibly Eqs. 7 and 10. Although supported Ru catalysts show higher activity for the NO/CO process than for the NO/H_2 process, and higher selectivity for N_2 production versus NH_3 production, they suffer a serious disadvantage under practical conditions, due to the volatility of ruthenium oxide (4). The most practical catalyst for nitric oxide reduction is supported rhodium metal (41). The fundamental reason for the high selectivity of rhodium catalysts for N_2 versus NH_3 has not been established; Taylor and Klimisch (43) have suggested that the stronger chemisorption ability of Rh for nitric oxide, as compared to Pt and Pd, leads to a greater probability of adjacent adsorbed N-species, favoring N_2 production.

The reduction of nitric oxide with carbon monoxide over rhodium metal can result in two possible nitrogen-containing reaction products, namely nitrous oxide (N_2O) and nitrogen (N_2), as shown in Eqs. 4 and 5. The selectivity of nitric oxide reduction to nitrogen increases with increasing temperature and decreasing pressure. For example, Rives-Arnau and Munuera (15) found that the amount of nitrous oxide produced, in the reduction of nitric oxide with carbon monoxide, reached a maximum at roughly 500 K, and subsequently decreased with increasing temperature for Rh/SiO_2. In addition to these results, Iizuka and Lundsford (44) reported that a Rh Y-zeolite catalyst will selectively reduce nitric oxide with carbon monoxide to nitrous oxide at 408 K. On the other hand, unsupported rhodium catalysts will reduce nitric oxide with carbon monoxide selectively to nitrogen, at low total pressures (i.e., $<1.3 \times 10^{-5}$ Pa), and at relatively high temperatures (i.e., >450 K) (6,10).

Formation of an adsorbed isocyanate intermediate is a widely reported result of the interaction of nitric oxide with carbon monoxide on supported rhodium catalysts (11,12,14,15). One possible mechanism for the formation of this intermediate is given in Eq. 12 (45). This intermediate is typically detected, via its strong infrared absorption

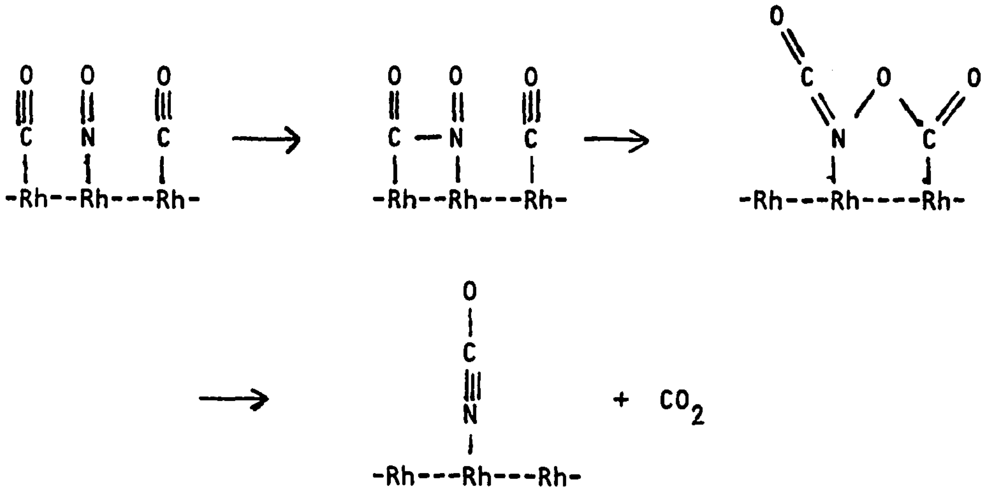

(12)

band at approximately 2269 cm^{-1}, as reported by Unland (12) for Rh/Al_2O_3. This intermediate has also been implicated as an important step in the formation of ammonia. Unland (12) reported a series of IR spectra for several noble metal catalysts, during a co-adsorption experiment for nitric oxide and carbon monoxide, at 400°C. These spectra illustrate that the intensity of the isocyanate absorption band was the lowest for the Ru/Al_2O_3 catalyst (12). Supported ruthenium is also the lowest producer of ammonia, in comparison with other noble metals, under practical conditions. The isocyanate intermediate has also been observed by Solymosi and Sarkany (11) on Rh/Al_2O_3, via an infrared absorption band at 2272 cm^{-1}. These authors report that this band quickly disappears, after the introduction of 1.3×10^3 Pa of water into the IR cell, at 170°C. Simultaneous with the disappearance of this band, ammonia production in the gas phase was observed (11). The isocyanate intermediate, therefore, is clearly important to the formation of ammonia over supported rhodium catalysts.

The effect of the catalyst support on the formation and stability of the isocyanate intermediate has been investigated by several authors (11,15). The position of the isocyanate absorption band is clearly dependent on the support. Solymosi and Sarkany (11) reported that this band appeared at 2210 cm^{-1} on Rh/TiO_2, 2235 cm^{-1} on Rh/MgO, 2272 cm^{-1} on Rh/Al_2O_3, and 2317 cm^{-1} on Rh/SiO_2. Similar results were reported for various supported Pt catalysts by Solymosi et al. (46). In addition, the stability of this isocyanate intermediate, as a function of the support, follows the sequence $Rh/TiO_2 < Rh/MgO < Rh/Al_2O_3 < Rh/SiO_2$. These results indicate that the formation and the stability of the isocyanate intermediate depends upon the support (11).

The reduction of nitric oxide with carbon monoxide has been studied on supported rhodium catalysts (14,15,44), polycrystalline rhodium wire (6), and the Rh(331) single crystal surface (10). In general, supported rhodium catalysts produce both molecular nitrogen and nitrous oxide as products in the reduction of nitric oxide with carbon monoxide. The amount of each depends upon the reactant pressures, temperature of the catalyst, and the nature of the catalyst support material. In particular, the reduction of nitric oxide with carbon monoxide was examined by Arai and Tominaga (14) on Rh/Al_2O_3. These authors found evidence, using IR, for the existence of a surface intermediate, consisting of a carbon monoxide and a nitric oxide molecule bound to a single rhodium atom, as shown in Eq. 13. This intermediate was proposed to decompose into an adsorbed nitrogen atom, by releasing CO_2, as shown in Eq. 14 (14). This

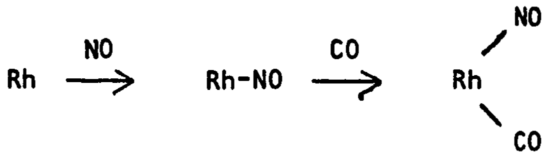

(13)

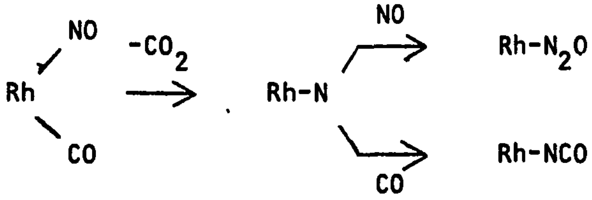

(14)

adsorbed nitrogen could then react with another gas phase nitric oxide, to form adsorbed nitrous oxide, or react with a gas phase carbon monoxide, to form an adsorbed isocyanate complex, also shown in Eq. 14 (14). This mechanistic scheme produced the adsorbates observed via infrared spectroscopy, and no attempt was made to quantitatively analyze the gas phase. Rives-Arnau and Munuera (15) examined the effect of the catalyst support on the activity and product distributions in the reduction of nitric oxide with carbon monoxide. The effect of temperature on the product distribution, for this reaction, suggested that the reduction of nitric oxide with carbon monoxide proceeded stepwise, as described in Eqs. 15 and 16 (15). Based upon the relative activities for nitric

$$CO + 2\ NO \longrightarrow CO_2 + N_2O \tag{15}$$

$$CO + N_2O \longrightarrow CO_2 + N_2 \tag{16}$$

oxide reduction of Rh/TiO_2 versus Rh/SiO_2, these authors concluded that the rate limiting step is the dissociative adsorption of nitric oxide on the catalyst surface. Rives-Arnau and Munüera (15) proposed the reaction mechanism given in equations 17 thru 20 to explain their results.

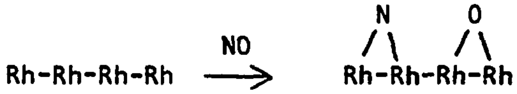
$$\text{Rh-Rh-Rh-Rh} \xrightarrow{\text{NO}} \overset{\text{N}}{\text{Rh-Rh}}\text{-}\overset{\text{O}}{\text{Rh-Rh}}$$
(17)

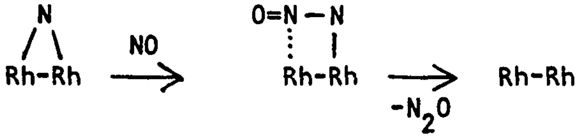
$$\overset{\text{N}}{\text{Rh-Rh}} \xrightarrow{\text{NO}} \overset{\text{O=N}-\text{N}}{\text{Rh-Rh}} \xrightarrow[-\text{N}_2\text{O}]{} \text{Rh-Rh}$$
(18)

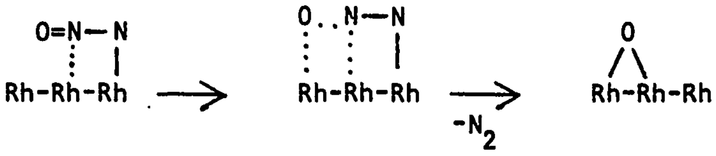
$$\overset{\text{O=N}-\text{N}}{\text{Rh-Rh-Rh}} \longrightarrow \overset{\text{O..N}-\text{N}}{\text{Rh-Rh-Rh}} \xrightarrow[-\text{N}_2]{} \overset{\text{O}}{\text{Rh-Rh}}\text{-Rh}$$
(19)

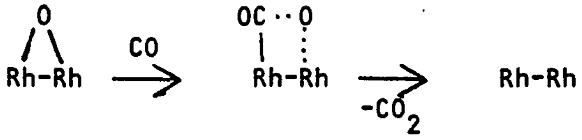
$$\overset{\text{O}}{\text{Rh-Rh}} \xrightarrow{\text{CO}} \overset{\text{OC}\cdots\text{O}}{\text{Rh-Rh}} \xrightarrow[-\text{CO}_2]{} \text{Rh-Rh}$$
(20)

The reduction of nitric oxide with carbon monoxide has been investigated over a polycrystalline rhodium wire (6). These authors reported preliminary steady-state kinetic results, as well as TDS analysis, following a co-adsorption experiment of nitric oxide and carbon monoxide. The steady-state reaction of nitric oxide with carbon monoxide on rhodium wire produced mostly CO_2 and N_2 (6). The reaction rate, of a one to one NO/CO mixture at a total pressure of 6.7×10^{-6} Pa, as a function of temperature, indicated that the reaction was strongly inhibited by adsorbed carbon monoxide at temperatures below 400 K (6). This effect was attributed to the blockage of surface sites by adsorbed carbon monoxide, inhibiting the dissociation of adsorbed molecular nitric oxide. At low temperatures (i.e., about 480 K), thermal desorption analysis indicated that the CO_2 product resulted from the Langmuir-Hinshelwood reaction between adsorbed oxygen and adsorbed carbon monoxide (6). At higher temperatures, the relatively high reaction rate implied the importance of a Rideal-Eley type mechanism between adsorbed oxygen and gas phase carbon monoxide (6).

Dubois et al. (10) examined the reduction of nitric oxide with carbon monoxide on the Rh(331) single crystal surface, utilizing HREELS and AES. The HREELS analysis of the co-adsorption, at 300 K, of CO and NO yielded a spectrum that was simply the sum of the HREELS spectra of the two separate reactants (10). This is significant, in that no surface isocyanate or Rh(NO)(CO) (see Eq. 13) intermediate was observed (10). Upon nitric oxide adsorption, at 700 K only adsorbed oxygen was present on the Rh(331) surface, and this adsorbate reacted quickly with gas phase (and/or adsorbed) carbon monoxide to form the carbon dioxide product (10). The authors propose the reaction mechanism given in Eqs. 21 and 22 to explain their results. In addition, they comment, that due to the

$$2\ NO\ (g) \longrightarrow N_2\ (g) + 2\ O\ (ads) \qquad (21)$$

$$2\ O\ (ads) + 2\ CO \longrightarrow 2\ CO_2\ (g) \qquad (22)$$

rapid reaction of CO with NO on the thoriated iridium mass spectrometer filaments, meaningful kinetic data could not be obtained (10).

It is clear from the above discussion that the mechanism of the reduction of nitric oxide with carbon monoxide on rhodium catalysts is not well-established. This lack of understanding centers mainly on the absence of a reported steady-state kinetic study on a well-characterized rhodium surface. In particular, the adsorption-desorption properties of nitric oxide on one of the simplest single crystal surfaces, namely the Rh(100), have yet to be fully characterized. All of this is rather surprising, and somewhat alarming, in light of the fact that rhodium metal is the principal element used for the reduction of nitric oxide in automobile catalytic converters! These facts have greatly contributed to the slow development of effective catalysts for the reduction of nitric oxide in exhaust emissions. It seems clear, from the work discussed above, that the reduction of nitric oxide with carbon monoxide proceeds via an oxygen intermediate at total pressures less than 1.3 x 10^{-5} Pa on stepped Rh(331) single crystal surface. However, it is questionable that this mechanism predominates under more realistic conditions. Therefore, the need for a mechanistic study of the reduction of nitric oxide with carbon monoxide, on well-characterized rhodium surfaces exists, and this fact formed the principal motivation behind this investigation.

EXPERIMENTAL

The reduction of nitric oxide with carbon monoxide on the Rh(100) single crystal surface was studied with a wide variety of experimental techniques. The main objective of this study was the development of a reaction mechanism that is consistent with the global kinetics, as measured over a wide range of initial conditions. The surface of the catalyst was characterized with Auger electron spectroscopy (AES) and low energy electron diffraction (LEED). In addition, thermal desorption spectroscopy (TDS) experiments were performed to examine the interaction of the reactants and products with the catalyst surface. This section will describe, in detail, the experimental procedures used for this investigation.

Reactor System Design

A clean metal surface is normally very reactive towards gas molecules striking it from the gas phase. It is clear, therefore, that in order to examine a catalytic reaction on a well-characterized metal surface, ultra-high vacuum (UHV) techniques must be employed. The principles behind the production of ultra-high vacuum are well-established (47), and these methods were applied in this study. The reactor system, as shown in Fig. 1, was constructed primarily of borosilicate glass (Pyrex), and 304 stainless steel. This system can be divided into three sections. The first section contains the quadrupole mass spectrometer and an ion pump, and is bounded by valves L1 and S1. This section has a base pressure of 3×10^{-8} Pa, and is pumped by a 3-stage mercury

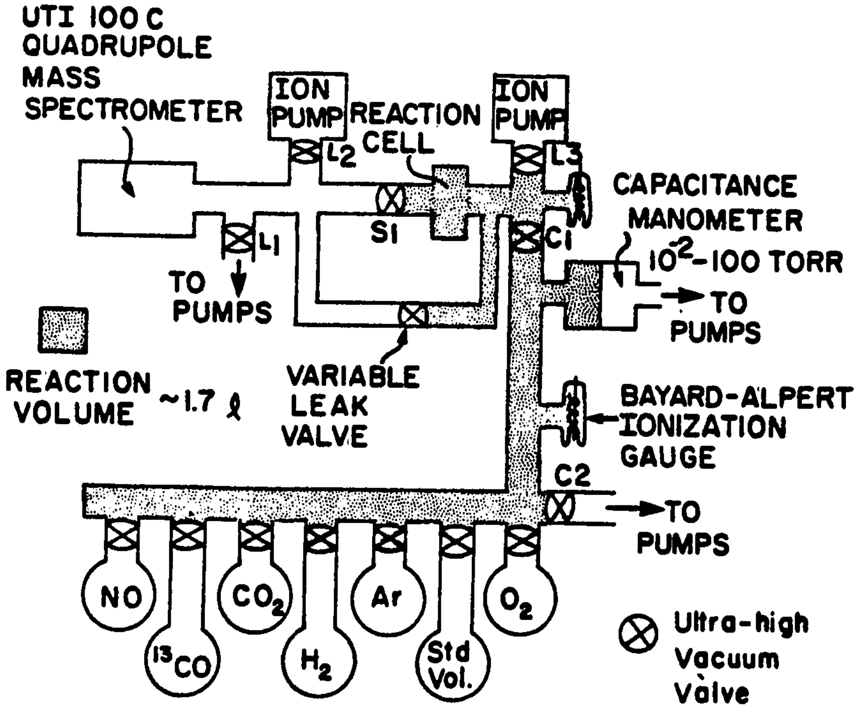

Figure 1. Schematic drawing of ultra-high vacuum system used for steady-state kinetic and thermal desorption experiments

diffusion pump in series with a 2-stage mercury diffusion pump. These pumps are separated from the UHV system by two liquid nitrogen (LN_2) traps, and are backed by a LN_2 trapped rotary oil pump. The second section, bounded by the variable leak valve and valves S1 and C1, contains the reaction cell and an ion pump. This section also has a base pressure of 3×10^{-8} Pa. The third section, bounded by valves C1 and C2, contains a gas manifold and a capacitance manometer. The gas manifold is pumped with two LN_2 trapped, 2-stage mercury diffusion pumps connected in series. These pumps are also backed by a liquid nitrogen trapped rotary oil pump. This section has a base pressure of 3×10^{-6} Pa. Each section contains a Bayard-Alpert ionization gauge suitable for pressure measurements in the range 0.1 to 1×10^{-8} Pa.

Only all metal ultra-high vacuum valves were used in the steady-state reactor system. A variable leak valve (Granville-Phillips, Model 203-012) was used to continuously sample the gas phase in the reaction cell. The conductance of this valve is continuously variable from 0.1 to 10^{-11} liters per second, which allows for a pressure ratio on the order of 10^{10}, between the differentially pumped mass spectrometer and the reaction cell. High conductance valves L1-L3 (Granville-Phillips, Model 204-010) were used to isolate the various sections of the system from the vacuum pumps for the purpose of kinetic studies, adsorption-desorption experiments, and for system maintenance. These valves had a relatively high conductance and, thus, did not seriously affect the system base pressure. Low conductance valves C1 and C2 (Granville-Phillips, Model 202-032) were used to isolate the gas manifold from the diffusion pumps, and to admit gases into the reaction cell region from the gas storage bulbs. A straight-through valve S1 (Varian, Model 951-5052) provided a line-of-site path from the single crystal reaction cell and the mass spectrometer ionization region. This geometry essentially eliminated wall effects during thermal desorption experiments.

A capacitance manometer (MKS, Model 170M-315BH-100) was used to accurately measure the partial pressure of the reactant gases. This pressure transducer was a differential capacitance manometer consisting of two regions separated by a thin metal diaphragm capable of measuring pressures in the range of 1.33 to 1.33×10^4 Pa. The capacitance manometer was thermostated at 50 ± 0.1°C with a solid state aluminum block heater (MKS, Model 170M-39). This manometer was factory calibrated against NBS traceable standards, and this calibration was supplied with the unit. This calibration was checked periodically with a McLeod Gauge (Consolidated Vacuum, Model GM-100A) using argon gas. This McLeod Gauge was capable of accurately measuring pressures in the range 0.133 to 133×10^3 Pa to within 5%. The calibration results were then fitted, via a linear least mean squares regression line, to Eq. 23 over the entire range of the McLeod Gauge. The result of this procedure

$$P_{\text{McLeod Gauge}} = A\, P_{\text{Capacitance Manometer}} + B \qquad (23)$$

indicated an agreement, to within 1%, between the capacitance manometer and the McLeod Gauge; thus, pressure was measured directly from the uncorrected capacitance manometer reading.

A quadrupole mass spectrometer (UTI, Model 100C) was used to directly monitor, via the variable leak valve, the gas phase composition in the catalytic reactor. This unit operated in the mass range 1-300 mass/charge units (m/e), and in the pressure range between 1×10^{-12} to 1×10^{-3} Pa. The product distribution during a reaction could be easily followed by scanning the mass range 1-50 m/e, and this was recorded on a 2-channel oscillographic recorder (Hewlett-Packard, Model 7402A) every 2.5 seconds. Alternately, for system maintenance and general survey scans, the mass spectrum was displayed on an oscilloscope (Gould, Model OS-300). Precise measurements of the reaction rate were accomplished utilizing a custom built microprocessor signal averager (Ames Laboratory Instrumentation Services). This unit operated using an analog to digital converter (Varian, Model V-2316) running at 5 Hz, to collect the peak height of a preselected m/e value. The average peak height was periodically printed on a digital thermal printer (Datel, Model DPP-7), and these data were subsequently entered into a minicomputer (Digital Equipment, Model VAX 11-780) for data reduction and kinetic modeling.

Rhodium Crystal Preparation

The Rh(100) single crystal sample was cut using spark erosion from a macroscopic single crystal rod obtained from Materials Research Corporation. The sample was aligned via the standard Laue x-ray backscattering methods prior to the cut, and this alignment was checked during every stage of sample preparation. The cut single crystal disc was mechanically polished to a mirror finish, and was within ∿1° of the desired alignment. The disc was essentially cylindrical in shape with a diameter of 7.0 mm, and was 0.75 mm thick. The total surface area of this sample was 0.93 cm^2, of which 82% consisted of the Rh(100) single crystal surface; the remaining 18% being edge area. The ideal surface structure of the Rh(100) single crystal face is shown in Fig. 2, where the dashed lines indicate the position of the atoms in the next layer. This surface has a simple square unit cell with a lattice parameter of 2.69 Å.

The Rh(100) single crystal disc was then mounted in the reaction cell as shown in Fig. 3. This was accomplished by spot-welding a 0.25 mm tungsten support wire directly on the sample, which was then spot-welded to a 1.1 mm tungsten support rod mounted in a pyrex dewar assembly. The temperature of the sample was monitored with a 0.076 mm tungsten/5% rhenium, tungsten/26% rhenium continuous thermal couple (Omega Engineering), which was also spot-welded directly onto the rhodium surface. The sample could be heated in two ways, as shown in Fig. 3, depending on the pressure in the reaction cell. The first method, useful at pressures less than 1×10^{-3} Pa, involved heating by electron bombardment. This was accomplished utilizing a thoriated iridium electron emitter, and a 400 volt accelerating potential supplied by a standard regulated power supply (Heath-Schlumberger, Model SP-2717). The temperature could be controlled, in the range 500 to 1500°C, via feedback control of the emission current from the emitter filament to the sample. The second method, useful at pressures up to 1.33×10^4 Pa (i.e., during catalytic reactions), involved simple radiant heat from a focused 1200 watt projector bulb. The temperature of the catalyst using this heating

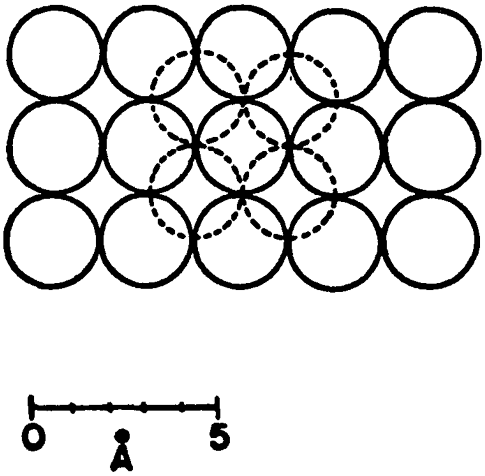

Figure 2. Ideal surface atom arrangement for the Rh(100) surface used in this investigation

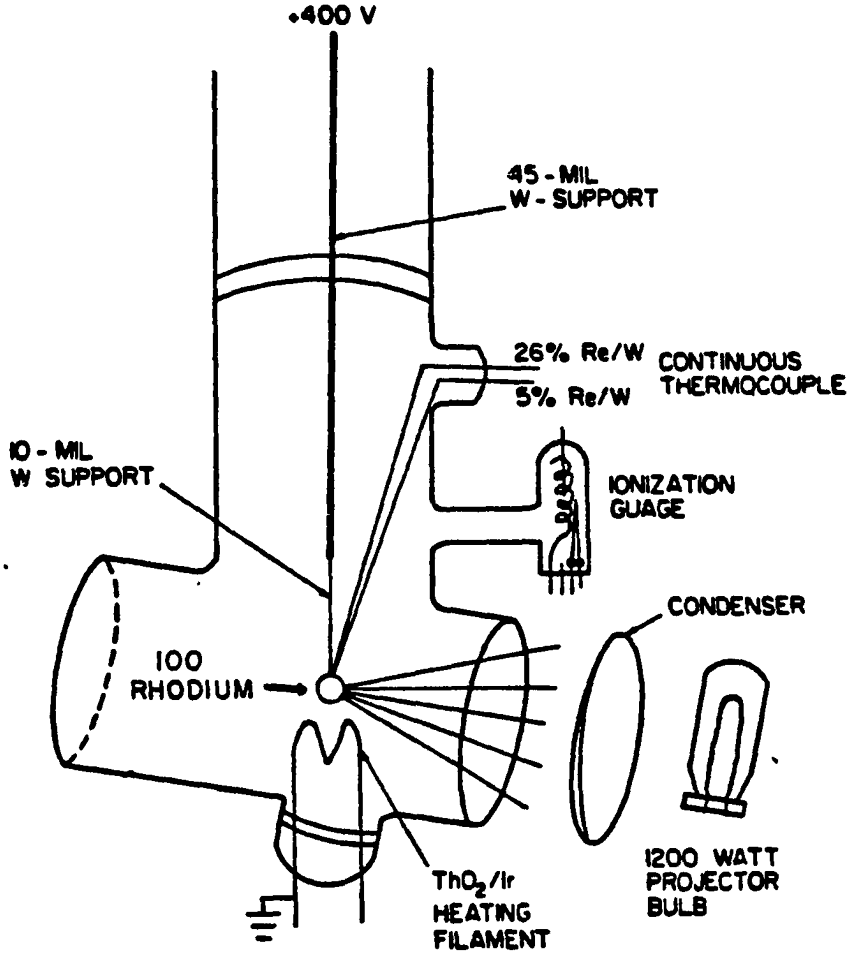

Figure 3. Schematic of reaction cell illustrating the two methods of sample heating

method was regulated, during a catalytic reaction, with a custom built feedback controller (Ames Laboratory Instrumentation Services), which compared the thermocouple emf with a preselected value, corresponding to the desired temperature.

The sample was initially cleaned by annealing in vacuum at 1000°C for several hours. The sample was then subjected to numerous cleaning techniques including oxidation, reduction, and high temperature annealing. The criterion for a clean sample, in this system, was necessarily that which produced a relatively high and reproducible reaction rate. Numerous procedures for the preparation of atomically clean rhodium surfaces have been reported in the literature (6-10,31), and a general review of cleaning procedures has recently been published (48). These cleaning procedures generally involve cycles of argon ion sputtering, heating in oxygen, high temperature annealing, and reduction with hydrogen. The exact procedure initially used in this investigation involved numerous cycles of oxidation (O_2, 7 x 10^{-2} Pa, 500°C, 10 minutes) and annealing (1000°C, 30 minutes). This procedure yielded a relatively low and irreproducible reaction rate, that varied erratically by as much as 50%. The reason for this will become apparent during the discussion of the surface characterization results. A subsequent procedure involving numerous cycles of reduction (H_2, 12.0 Pa, 415°C, 15 minutes) followed by high temperature annealing (650°C, 15 minutes), yielded reaction rates approximately an order of magnitude higher than those achieved by the former cleaning procedure. These reaction rates were extremely reproducible, regularly to within 10%, but varying by as much as 15%. The latter cleaning procedure is similar to that reported previously by Baird et al. (8) and the consequences, implications, and limitations of this approach will be discussed in detail in later sections.

During the cleaning process, it was discovered that the thoriated iridium filament, used for electron bombardment heating, interfered with the determination of the reaction rate on the rhodium metal sample. Iridium has been reported to be an effective catalyst for the reduction of nitric oxide with carbon monoxide (49,50). This effect was eliminated by removing the filament after the catalyst was cleaned. In addition to this problem, the thoriated iridium filaments initially used in the mass spectrometer, also interfered with the reaction rate measurement, although to a lesser extent. This effect has been previously noted by Dubois et al. (10), and was eliminated by replacing the thoriated iridium filaments with tungsten/3% rhenium filaments.

Kinetic Procedure

The reduction of nitric oxide with carbon monoxide on the Rh(100) single crystal catalysts was studied at a temperature of 415°C and in the pressure range of 1.33 to 6.7×10^3 Pa. During a reaction run, the catalyst temperature was maintained, to ±3K, utilizing the focused light from the projector bulb, as discussed previously. This heating method limited the temperature to a maximum of approximately 600°C, due to thermal conductivities of the reactant gases. The reaction was studied over the entire range of the available capacitance manometer, and in order to achieve a measurable reaction rate over this wide pressure variation, a catalyst temperature of 415°C was used for the collection of reactant and product order data.

The reduction of nitric oxide with carbon monoxide on rhodium metal produces three possible products, namely N_2, N_2O, and CO_2, as shown in Eqs. 1 and 2. It is clear that under normal circumstances the separation of the nitrous oxide and carbon dioxide products, both with m/e = 44, would be difficult using a mass spectrometer with unit resolution. It is for this reason that labeled carbon-13 monoxide was used as a reductant during this mechanistic investigation. This method allowed for the easy separation of all the possible reaction products and reactants, namely N_2 (m/e = 28), N_2O (m/e = 44), NO (m/e = 30), ^{13}CO (m/e = 29), and $^{13}CO_2$ (m/e = 45). In general, to continuously monitor the progress of the reaction as a function of time, the change in the peak height of the $^{13}CO_2$ was recorded. The reason for this selection will become clear shortly. It is well-established (6,51,52) that nitric oxide interacts quite strongly with the interior glass and metal walls of a well-baked ultra-high vacuum system. This results in both a low pumping speed for nitric oxide and a relatively high nitric oxide background partial pressure. In addition to this problem, nitric oxide will heterogeneously decompose on hot metal surfaces, such as those present in the mass spectrometer ionizer region, to nitrogen and oxygen. These complications make the peak at m/e = 30 relatively useless as a measure of the progress of the reaction. The high background of the m/e = 28 peak, as well as the contribution to this peak by the above mentioned nitric oxide heterogeneous decomposition reaction, make the use of this peak undesirable as a measure of the extent of the reaction. In addition, the high initial peak heights of the reactant peaks at m/e = 29 and m/e = 30 also preclude their use, since this would require the small difference between two large numbers to obtain the reaction rate. Product distribution analysis clearly indicated that, under the reaction conditions used in this investigation, no detectable amount of gas phase nitrous oxide was produced, and only nitrogen and carbon-13 dioxide were detected as reaction products. This implies that the reduction of nitric oxide with carbon monoxide proceeded according to Eq. 1. Therefore, the reaction rate was generally monitored using the m/e = 45, $^{13}CO_2$ product peak.

The reaction rate was determined over a wide range of initial conditions, with each kinetic experiment being commonly denoted as a reaction run. The procedure generally used for these kinetic runs involved the following steps. First the catalyst was cleaned, prior to each kinetic run, as described above (H_2, 12.0 Pa, 415°C, 15 minutes, followed by 650°C, 15 minutes). The catalyst was then preheated to the desired reaction temperature, usually 415°C, with valves C1 and C2 (see Fig. 1) closed. The appropriate partial pressure of each reactant was admitted into the gas manifold, from the respective gas storage bulb, using the capacitance manometer to measure the partial pressures. With valves S1 and L1 closed and the variable leak valve previously opened to a calibrated position, the catalytic reaction was initiated by simply opening valve C2. The extent of the reaction was continuously monitored by the differentially pumped quadrupole mass spectrometer, which analyzed a small sample of the gas phase via the variable leak valve. This valve allowed only a small portion, generally less than 1%, of the reactor gas phase to be removed from the catalytic reaction cell during a kinetic run. The reaction cell, therefore, operated as a static batch reactor. This arrangement facilitated the measurement of the reaction product distribution, as well as the initial reaction rate. This reaction rate was determined from the slope of a linear least mean squares regression line, calculated from the time dependence of the m/e = 45 mass spectrometer peak height. Since only initial rates were measured, this peak at m/e = 45 had a linear time dependence. This kinetic procedure was repeated numerous times over a wide range of initial conditions, to obtain reactant and product order plots.

The above kinetic procedure yielded a system dependent reaction rate in units of amperes, of mass spectrometer ion current, per second. This reaction rate can be easily converted to units of molecules of product produced, per square centimeter of catalyst surface area per second, by using several known system parameters (53-55). These parameters include the total reaction volume, the mass spectrometer sensitivity, the catalyst surface area, and the temperature of the gas phase in the reaction cell. The volume of the catalytic reaction cell was determined by argon gas expansion using a standard volume, and measuring the pressure with the capacitance manometer. The total reaction volume (i.e., the shaded area shown in Fig. 1) was 1.99 liters. The mass spectrometer sensitivity was empirically determined, via a calibration between the mass spectrometer response and a known pressure of carbon dioxide, as measured by the capacitance manometer. This sensitivity was reproducible to within 10%, for a given set of system parameters (i.e., leak rate, electron multiplier gain, system pumping speed, etc.), and was checked periodically. The catalyst surface area was assumed to be the total geometric surface of the Rh(100) single crystal disc and was calculated to be 0.93 cm^2. The temperature of the gas phase was assumed to be 300 K.

The rate of the reduction of nitric oxide with carbon monoxide was measured over a wide range of initial conditions, in the range between 1.33 to 6.7×10^3 Pa. In general, the partial pressure dependence of the reaction rate was examined, by determining reactant and product orders over several orders of magnitude change in the respective partial pressure. These order plots were obtained at 415°C. In addition to these experiments, the temperature dependence of the reaction rate was examined over the range 250-550°C. These results will be discussed in a later section.

Thermal Desorption Procedure

The bonding states available to the reactants and products were examined with thermal desorption spectroscopy (TDS). The procedure used during the TDS experiments was as follows:

1. Cool the clean Rh(100) surface to 300 K.
2. Dose a known quantity of the desired gas into the reaction cell region, as measured in Langmuirs (L) (i.e., $1 \text{ L} = 1.3332 \times 10^{-4}$ Pa sec).

3. With valves S1 and L1 open, ramp the crystal temperature, from 300 to 1048 K, at ∿10 K/sec with the focused light beam, while differentially pumping the cell.
4. Monitor desorption peaks by observing total pressure and mass spectrometer ion currents as functions of temperature.
5. Repeat the procedure for various exposures of the sample.

The above procedure was modified slightly due to the strong interaction of nitric oxide with the walls of the reaction cell. In particular, adsorption of nitric oxide on the flat glass lens on the end of the reaction cell interfered with the low exposure thermal desorption experiments. This problem manifested itself by a rapid NO desorption, and increase in the background NO partial pressure, simultaneously with the beginning of the temperature ramp. These phenomena are attributable to the thermal (and/or photon) desorption from the interior glass walls of the reaction cell, caused by the light generated by the projector light bulb. This effect was virtually eliminated by increasing the glass wall temperature to 150°C during the entire thermal desorption procedure for experiments involving nitric oxide.

LEED/Auger Procedure

Low energy electron diffraction (LEED) and Auger electron spectroscopy (AES) are useful complementary techniques for analysis of catalytic surfaces. Auger analysis of catalyst samples will yield detailed information concerning the atomic composition of the surface region. In addition, it is often possible to determine the chemical state of adsorbates via line shape analysis. On the other hand, LEED analysis will yield information concerning the surface symmetry of the substrate and adsorbate, if it forms an ordered overlayer. Precise measurements of diffracted beam intensities versus beam voltage can be used to determine the surface structure of adsorbate overlayers. In addition, LEED patterns can be used to calibrate Auger signals assuming a homogeneous distribution of the adsorbate. This study utilized both LEED and Auger analysis to develop a cleaning procedure, and to examine catalyst-adsorbate and adsorbate-adsorbate interactions.

The LEED/Auger experiments were performed in a standard ultra-high vacuum system (Varian, Model 981-2000), which was pumped with a 200 liter/sec ion pump. This system was equipped with a 4-grid LEED optics, for LEED analysis, and a cylindrical mirror analyzer (Varian, Model 981-2707) (CMA), for Auger electron detection. Auger electron spectra were recorded in the derivative mode (i.e., d N(E)/dE) using a phase sensitive detection method employing a lock-in amplifier (Princeton Applied Research, Model 128A/90), at a frequency of 17 kHz with a modulation voltage of 5 volts peak to peak. A co-axial electron gun (Varian, Model 981-2713) was used to excite the core holes, operating at a beam energy of 2 keV and a beam current of 0.5μ amps. The Rh(100) sample was mounted on a rotatable offset precision x,y,z manipulator (Varian, Model 981-2523). A continuous thermocouple tungsten/5% rhenium, tungsten/26% rhenium was mechanically mounted between the crystal sample and an indirect resistive heater. This arrangement allowed the sample to be heated in the range 300 to 1500 K. In addition, a ion gun (Varian, Model 981-2043) was available for the purpose of cleaning the sample. The LEED patterns were obtained using the 4-grid LEED optics (Varian, Model 981-0127) at energies between 50 and 250 eV, and were recorded using high speed Polaroid film.

The ultra-high vacuum system was attached to a gas manifold, via a variable leak valve (Granville-Phillips, Model 203-012). This system was pumped with LN_2 trapped mercury diffusion pumps and contained numerous storage bulbs containing gas used for cleaning the sample, and for adsorption experiments.

Materials

The oxygen (99.995%), nitrogen (99.998%), argon (99.9995%), hydrogen (99.998%), and carbon dioxide (99.998%) were obtained, in 1 liter glass bulbs with break seals, from the Linde Division of the Union Carbide Corporation, and were used without further purification. The nitric oxide (98.5%) was obtained in a lecture bottle, also from the Linde Division. Mass spectrometer analysis showed the major impurities to be other oxides of nitrogen, carbon monoxide, nitrogen, and a trace amount of argon. This gas was then vacuum distilled and loaded into 1 liter pyrex bulbs with break seals. Subsequent mass analysis showed no significant impurities. The carbon-13 monoxide was obtained from the Mound Laboratory Division of the Monsanto Corporation, and had a 99% enrichment of carbon-13. The ^{13}CO (98%) contained 2% of argon gas and no other detectable impurities; this gas was used without further purification. The hydrogen used for cleaning purposes during the LEED/Auger experiments was purified by diffusion through Pd/25% Ag.

RESULTS AND DISCUSSION

There is great difficulty in establishing the mechanism of a heterogeneous catalytic reaction. There are two main reasons for this difficulty. First, the surface of most catalysts is not uniform, either geometrically or energetically. This fact leads to coverage dependent heats of adsorption and coverage dependent interactions between adsorbates, in reacting systems. There is no known way to predict in advance the importance of these effects, and this requires a somewhat arbitrary choice of an adsorption isotherm, typically of the Langmuir type. This adsorption isotherm is the basis of the second difficulty with heterogeneous catalytic kinetics. In particular, there is no known method capable of directly measuring the concentration of the reacting species under typical reaction conditions. The reason for this problem lies directly with the fact that heterogeneous chemical reactions occur on a surface, and the concentration of reacting species is quite low ($\sim 10^{15}$ molecules/cm^2), by comparison with the concentration of the catalyst ($\sim 10^{22}$ molecules/cm^3), and the reacting gas phase ($\sim 10^{19}$ molecules/cm^3). This leads to great difficulty in detecting reaction intermediates and establishing reaction mechanisms. In short, these difficulties necessitate a multi-technique approach to the elucidation of a heterogeneous reaction mechanism. This study was such an investigation, and utilized steady-state kinetics, over a wide variation in initial conditions, to establish the global kinetics, and low energy electron diffraction (LEED), Auger electron spectroscopy (AES), and thermal desorption spectroscopy (TDS), to characterize the catalyst surface. Finally, a reaction mechanism will be developed which is consistent with all of these results.

Surface Characterization

As discussed above, the catalyst surface was characterized with a series of LEED/Auger and TDS experiments. The objectives of these experiments include the establishment of a cleaning procedure, and the characterization of the adsorption-desorption properties of the reactants and products, of the reaction between nitric oxide and carbon monoxide. Several systematic studies of the adsorption-desorption properties of individual small molecules (i.e., NO, CO, H_2, O_2, N_2, etc.) on well-characterized rhodium surfaces have been reported previously (6-10,20). The purpose of this investigation is to verify these results, and fill the voids that exist with respect to nitric oxide adsorption-desorption characteristics on the Rh(100) single crystal surface.

As described previously, a cut and polished Rh(100) single crystal was mounted on an offset manipulator, and placed in the LEED/Auger system. After the usual pump-down and bake-out, an initial Auger spectrum, shown in Fig. 4(a), revealed surface contamination by phosphorus, sulfur, and boron. This result is fairly typical and numerous cleaning procedures have been reported to obtain a clean rhodium surface (7,9,10,55, 56). The exact procedure used in this investigation initially involved high temperature bombardment by reactive ion beams. In particular, the sulfur contaminant was removed by cycles of high temperature hydrogen ion bombardment (1000 eV, 500°C, 20 minutes), followed by annealing the sample (1000°C, 10 minutes). Such a procedure is unique in the sense

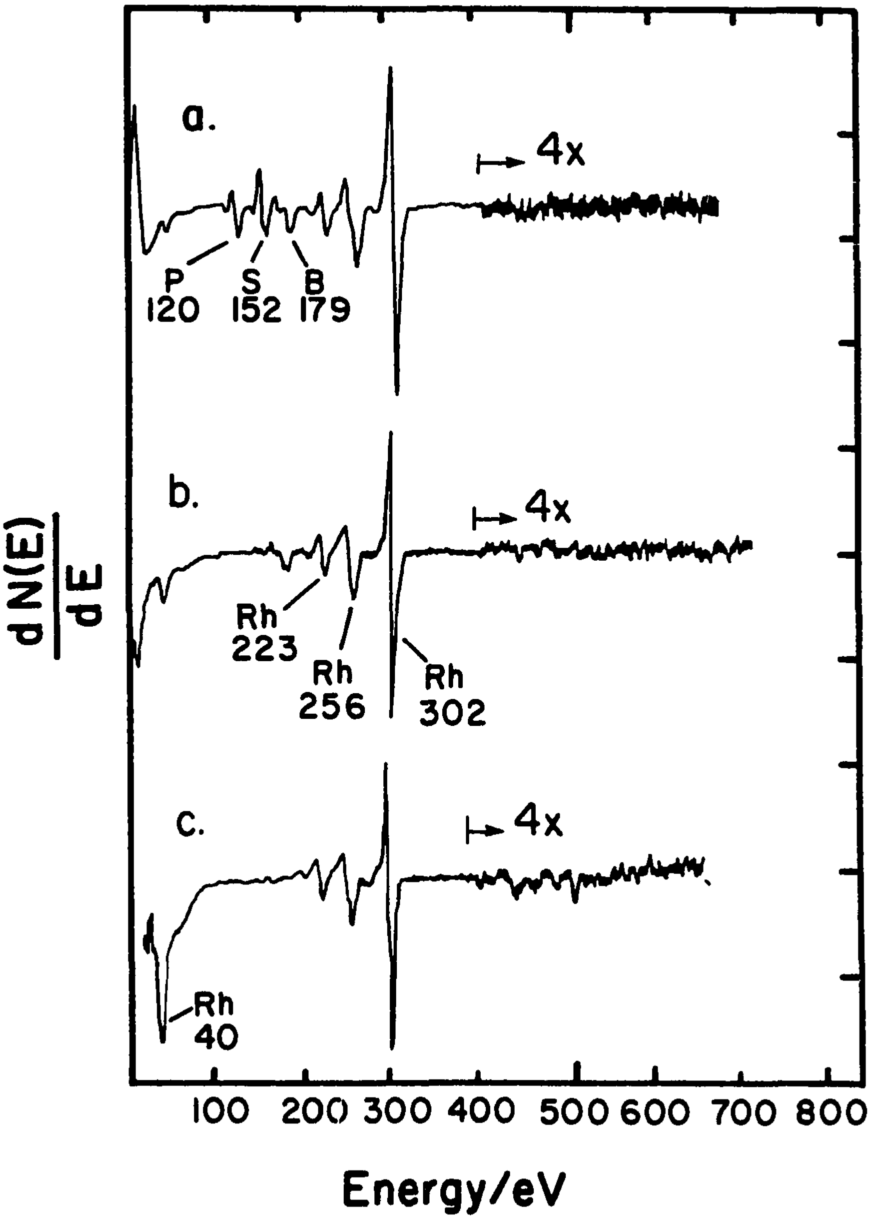

Figure 4. Auger spectra of Rh(100) surface during cleaning procedure: (a) initial Auger spectrum; (b) Auger spectrum after H_2 and O_2 bombardment; (c) Auger spectrum of clean Rh(100)

that ion bombardment cleaning is usually achieved via a physical process (i.e., momentum transfer), with an argon ion beam sputtering away the undesired contaminants. Unfortunately, the substrate lattice is damaged somewhat by this process, by ion implantation and the sputtering of the substrate itself. Since the mass of the impinging particle is much less for hydrogen than for argon, the lattice bombardment damage is greatly reduced, and the sulfur contaminant is selectively removed. This technique has been used previously for the removal of carbon, sulfur, and oxygen surface contaminants from steel surfaces (57). Phosphorus was similarly removed, via cycles of high temperature oxygen ion bombardment (1000 eV, 500°C, 10 minutes), followed by annealing the sample (1000°C, 10 minutes). This procedure yielded a relatively clean surface, contaminated only with boron, as illustrated by the rhodium Auger lines at 40, 223, 256, and 302 eV, shown in Fig. 4(b).

The boron contaminant could be detected via its Auger line at 179 eV and was extremely resistant to the above cleaning procedures. The surface boron contaminant could be removed via numerous cycles of argon ion bombardment (3 keV, 25°C, 60 minutes), followed by high temperature annealing (1000°C, 10 minutes). During this procedure, several experimental results were observed concerning this boron impurity. Namely, boron segregates to the surface from the bulk at temperatures greater than about 750°C. In addition, the boron initially formed a (3 x 1) ordered overlayer as described in Figs. 5(a)-(c). As boron was depleted from the bulk, it then segregated to a lesser extent and formed a (3 x 3) ordered overlayer, as described in Figs. 6(a)-(c). Once segregated

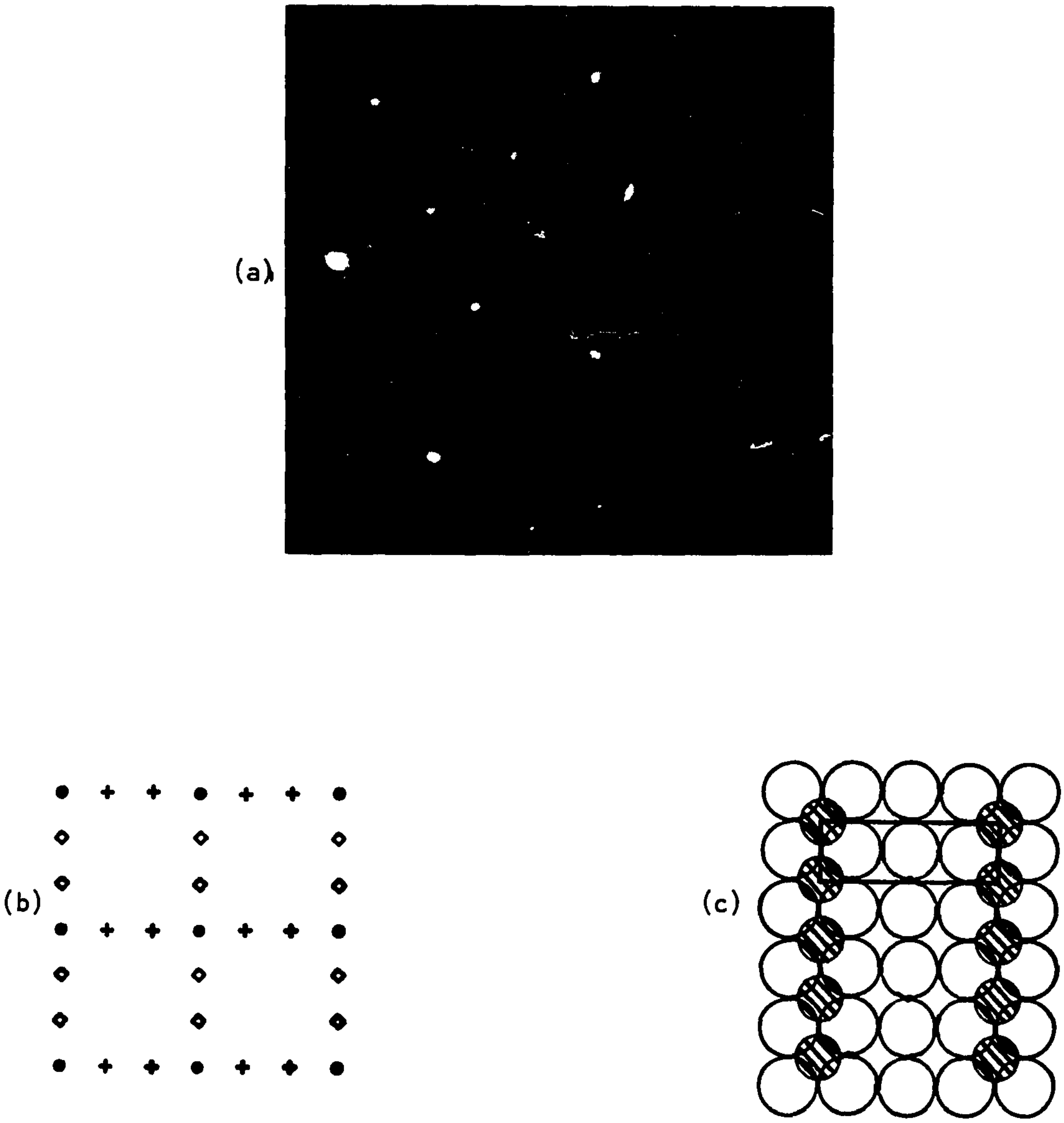

Figure 5. LEED pattern (a) observed for ordered boron overlayer at 167 eV, illustrating diffraction from two domains, (3 x 1)-B; (b) schematic of diffraction spots from Rh substrate ●, and the two domains of boron, ◇ and +; (c) possible surface structure of boron ordered overlayer illustrating new unit cell

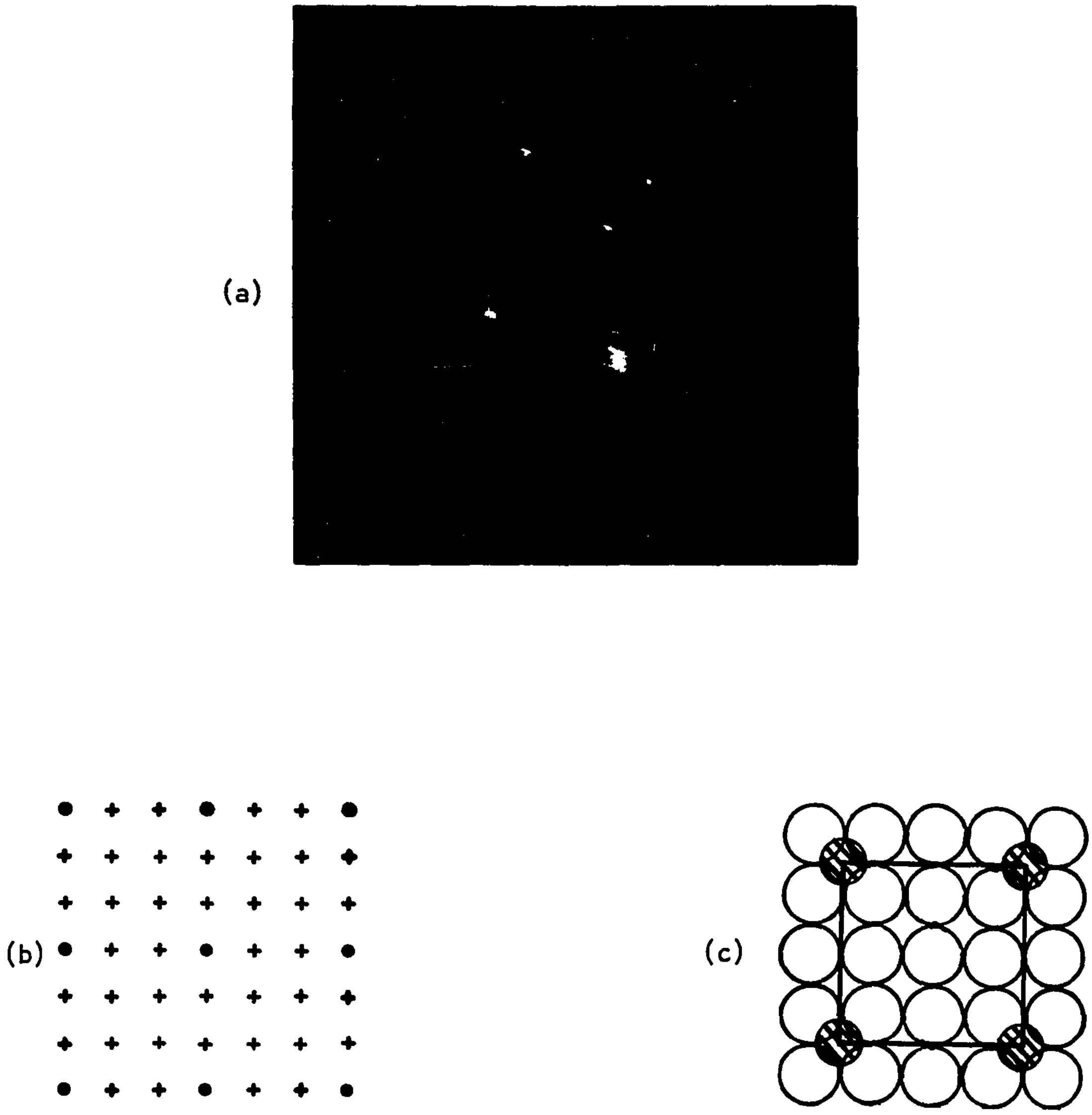

Figure 6. LEED pattern (a) observed at 69 eV for boron ordered overlayer after additional cleaning, (3 x 3)-B; (b) schematic of diffraction spots from the Rh substrate ●, and the boron ordered overlayer +; (c) possible surface structure of boron ordered overlayer illustrating new unit cell

to the surface, this boron could be reversibly oxidized (1.3×10^{-3} Pa O_2, 500°C, 1 minute), and then reduced by high temperature flashing (1000°C, 5 minutes). This procedure is illustrated in Figs. 7(a)-(c). The boron oxide formed, most probably BO_2^- (25,56), could be identified via its characteristic Auger peak at 171 eV, as shown in Fig. 7(b). This Auger peak represents a chemical shift, of approximately 8 eV, from the normal position of elemental boron, which has an Auger peak at 179 eV, as shown in Figs. 7(a) and 7(c). Countless cycles of argon bombardment and high temperature annealing greatly reduced, but did not eliminate, the segregation of boron from the bulk.

A clean surface, however, could be reproducibly prepared in the following manner. After the above mentioned cycles of argon ion bombardment and high temperature annealing, a clean surface could be prepared using a single cycle of argon ion bombardment (3 keV, 25°C, 3.4 μA, 60 minutes), followed by a high temperature flash to repair the lattice bombardment damage (500°C, 30 seconds). The surface produced in this manner exhibited no detectable impurities, as shown by the Auger spectrum in Fig. 4(c), and displayed a sharp (1 x 1) LEED pattern, as described in Figs. 8(a)-(c). This clean surface was stable, provided the sample temperature remained below 750°C in vacuum, at which temperature significant amounts of boron once again segregated to the surface. For all of the subsequent LEED/Auger experiments, a clean surface was prepared in this manner and the sample temperature remained below 750°C.

The first set of LEED/Auger experiments involved the characterization of the adsorption-desorption properties of the individual reactants.

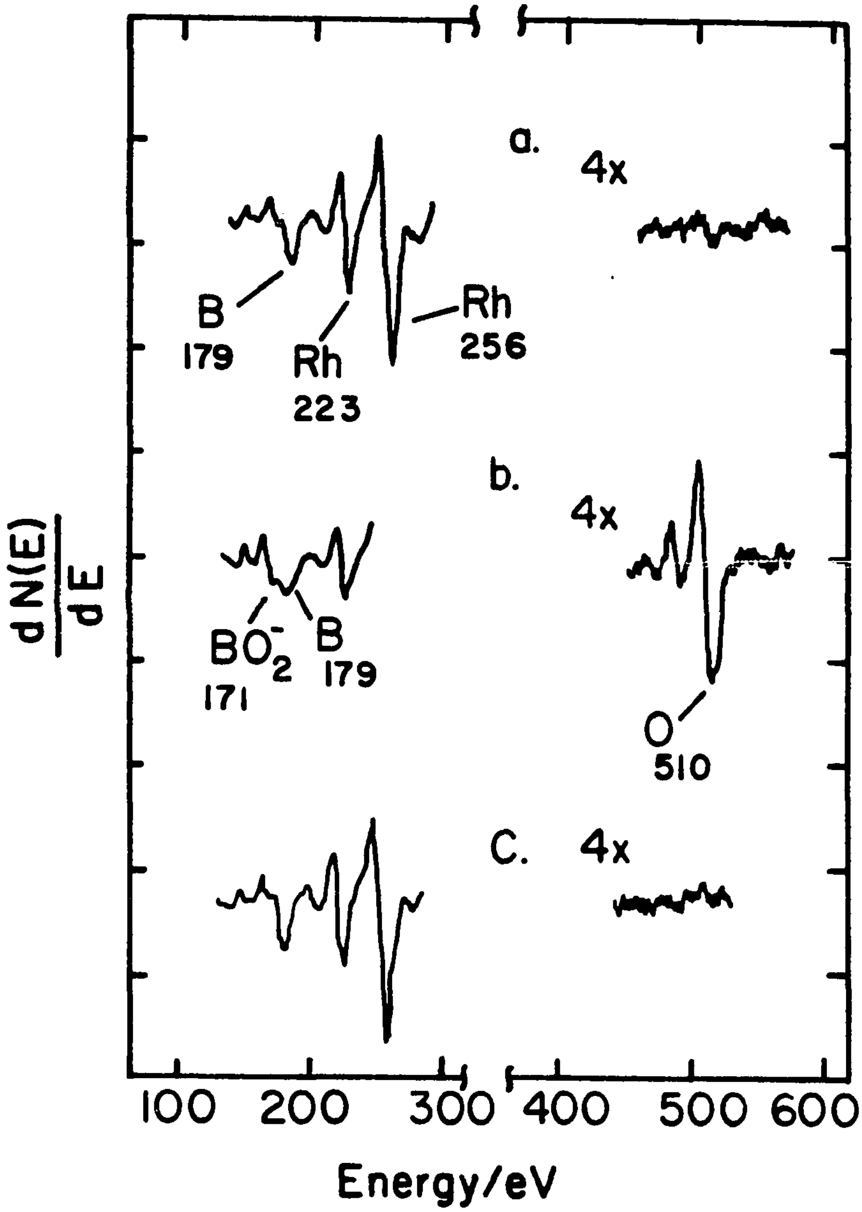

Figure 7. Auger spectra recorded during surface boron oxidation illustrating (a) elemental boron contaminant; (b) Auger spectrum after oxidation illustrating BO_2^- surface species via Auger peak at 171 eV; (c) Auger spectrum of reduced boron after high temperature annealing

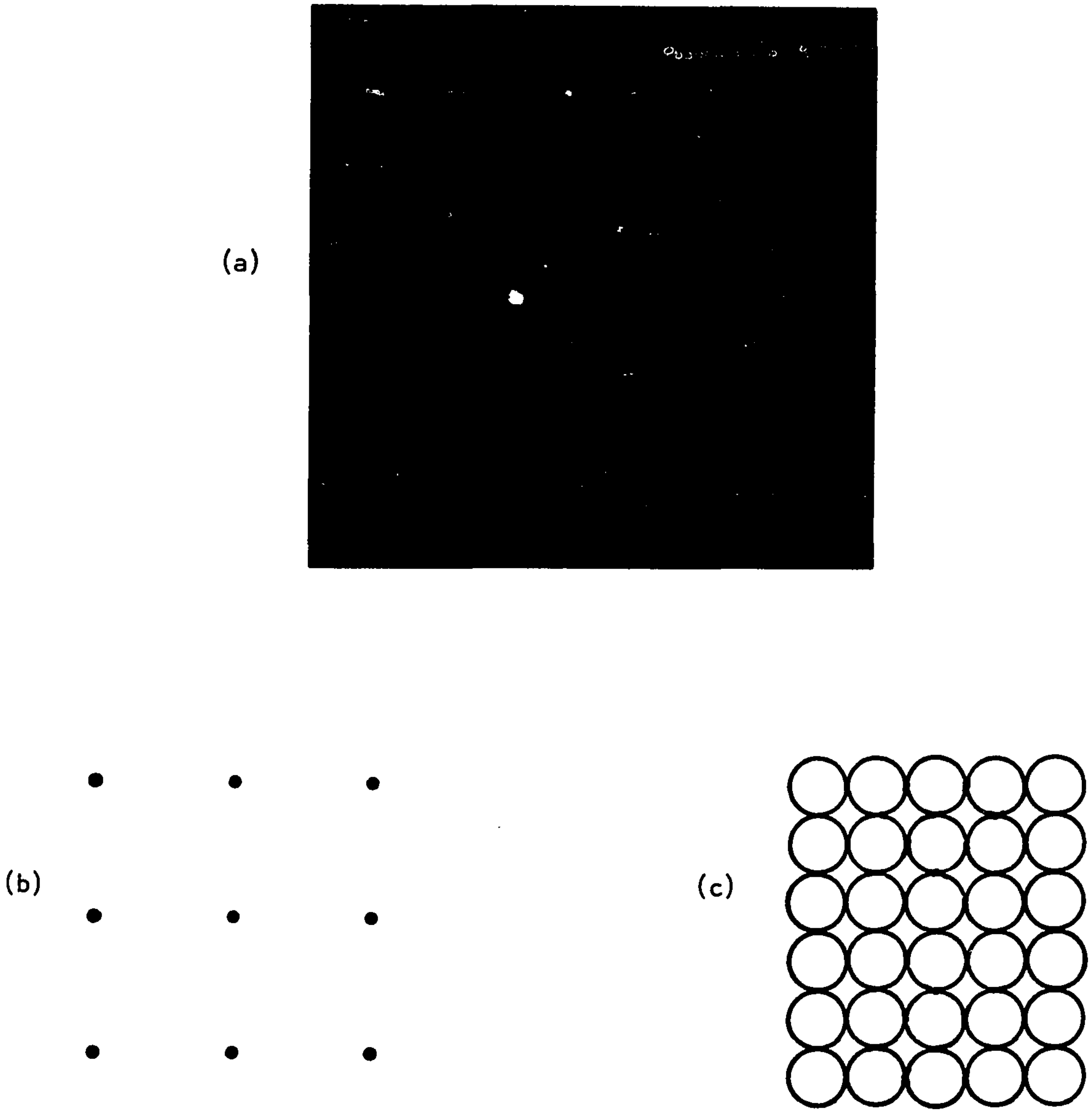

Figure 8. Clean Rh(100) surface illustrating: (a) (1 x 1) LEED pattern at 91 eV; (b) schematic of diffraction pattern from Rh substrate ●; (c) ideal surface structure of clean Rh(100)

Auger analysis of the adsorption of carbon monoxide gave results similar to those reported previously by Castner et al. (7) and, thus, will not be discussed here. It is noteworthy to mention that no conclusive evidence for carbon monoxide dissociation was observed during this investigation. Dissociation of carbon monoxide induced by the probing electron beam was observed, and this effect has been reported previously (28). Nitric oxide adsorbs with a high sticking coefficient, and at saturation forms a c(2 x 2) ordered overlayer, as described in Figs. 9(a)-(c). This ordered overlayer has also been reported by Castner et al. (7). In an effort to characterize the thermal stability of this intermediate, a step-wise heating experiment was performed on this nitric oxide overlayer. This experiment was accomplished by heating the sample to successively higher temperatures for 10 minutes; the Auger spectra were recorded at room temperature. The results of this procedure are shown in Fig. 10. As illustrated in this figure, the nitric oxide adsorbate is relatively stable up to 200°C, showing only a small drop in coverage, as indicated by the small drop in Auger peak intensity. This small drop is most likely due to molecular nitric oxide desorption occurring at approximately 400 K. At approximately 300°C, a precipitous drop in the nitrogen peak intensity occurs, while the oxygen Auger peak remains relatively unaffected. At about 600°C, the oxygen Auger peak decreases likewise, and is essentially zero at 700°C. These results indicate the competition between two processes, namely molecular nitric oxide adsorption-desorption, according to Eq. (24), and nitric oxide dissociation followed by nitrogen desorption, according

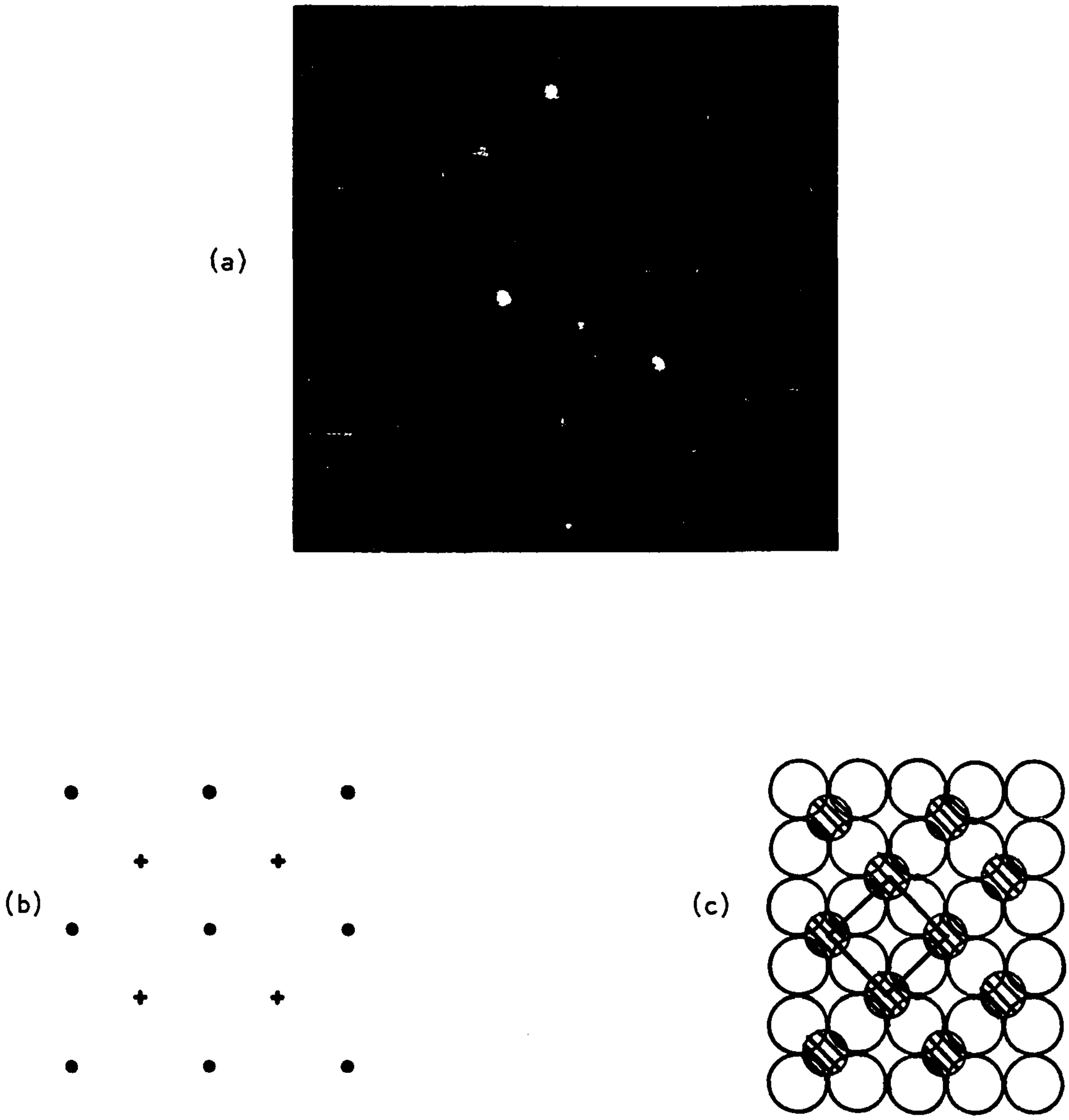

Figure 9. LEED pattern (a) of nitric oxide adsorbate at 91 eV; (b) schematic of diffraction spots from Rh substrate ●, and NO ordered overlayer +; (c) possible surface structure of NO ordered overlayer illustrating new unit cell

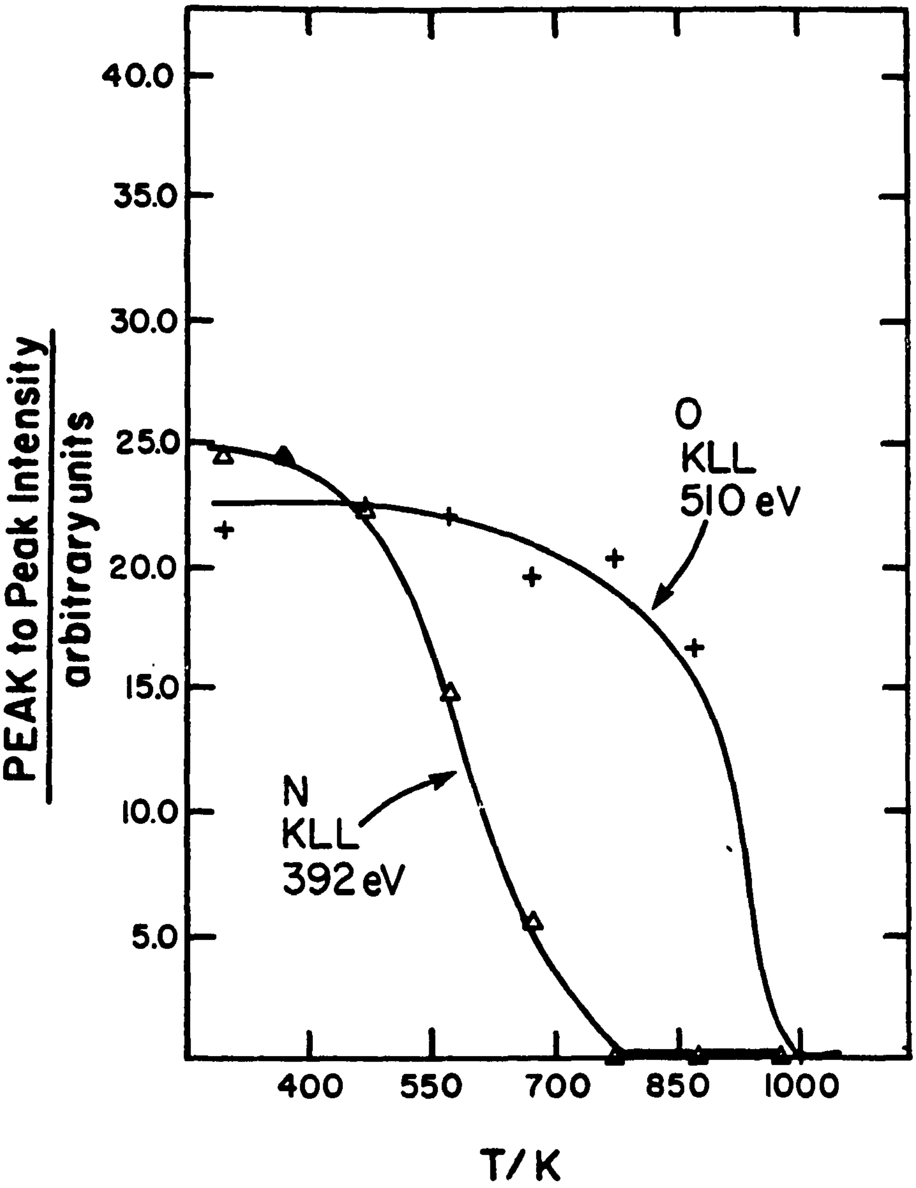

Figure 10. Thermal stability of adsorbed nitric oxide as determined using the N and O KLL Auger peaks

to Eqs. 25 and 26. The oxygen adsorbate could either desorb, according to Eq. 27, or diffuse into the bulk, a process previously reported to

$$\mathrm{NO\ (g)} + * \Longleftrightarrow \mathrm{NO\ (ads)} \tag{24}$$

$$\mathrm{NO\ (ads)} + * \longrightarrow \mathrm{N(ads)} + \mathrm{O\ (ads)} \tag{25}$$

$$2\ \mathrm{N\ (ads)} \longrightarrow \mathrm{N_2\ (g)} + 2\ * \tag{26}$$

$$2\ \mathrm{O\ (ads)} \longrightarrow \mathrm{O_2\ (g)} + 2\ * \tag{27}$$

occur (7,33). These results are in general agreement with the nitric oxide adsorption results reported previously (6-10,20).

The interaction of nitrogen and carbon dioxide likewise follows results published previously (6-10,20). The adsorption of carbon dioxide produced the expected c(2 x 2) ordered overlayer, and most probably represents dissociative adsorption into adsorbed carbon monoxide and oxygen. Although nitrogen does not normally adsorb to rhodium surfaces, previous authors (35) have reported adsorption of thermally activated nitrogen. All attempts to adsorb nitrogen in this manner failed, most likely due to the relatively low temperature of the thoriated-iridium activation source.

In an effort to examine the state of the catalyst under reaction conditions, a co-adsorption experiment was performed with a 1:1 mixture of NO/CO at 688 K, and a total pressure of 8×10^{-3} Pa. The result of this procedure is shown in Eq. 28. The range of coverages reported here represents the two methods used to record the Auger spectra. The figures in the left-hand column represent the calculated coverages, if the gas phase is removed first and then the substrate is reduced to

$$\begin{array}{c} (1 \times 1) \\ \mathrm{Rh} \end{array} \xrightarrow[\substack{688\ \mathrm{K} \\ 5\ \mathrm{minutes}}]{\substack{8 \times 10^{-3}\ \mathrm{Pa} \\ \mathrm{NO/CO}\ \ 1:1}} \begin{array}{ll} & c(2 \times 2) \\ \mathrm{O\ (ads)} & 0.08\text{-}0.05\ \text{monolayers} \\ \mathrm{N\ (ads)} & 0.09\text{-}0.20\ \text{monolayers} \\ \mathrm{C\ (ads)} & 0.21\text{-}0.13\ \text{monolayers} \end{array} \tag{28}$$

room temperature, prior to recording the Auger spectra. The figures on the right represent the reverse of that process prior to the Auger experiment. These coverages were calculated utilizing published sensitivities (58), and are based upon the peak intensity of the C, O, and N KLL Auger lines, relative to the Rh MNN Auger line at 302 eV. The absolute calibration was based on the oxygen KLL Auger peak of the 0.25 monolayer p(2 x 2) oxygen ordered overlayer. Several points should be made at this time concerning the results of this experiment. First, the surface contains a significant amount of adsorbed nitrogen and, second, the surface is not extensively oxidized under these reaction conditions. It has been concluded by previous workers (6,10) that the surface coverage by nitrogen was negligible, during the reduction of nitric oxide with carbon monoxide. These conclusions were based upon nitric oxide adsorption at room temperature, and a total pressure in the 1.3×10^{-5} Pa range, followed by heating of the sample in vacuum. The present Auger experiment involves NO/CO co-adsorption at 688 K, in the 1.3×10^{-3} Pa range.

The surface of the catalyst was further characterized with a series of thermal desorption experiments. It should be stressed at this time that the thermal desorption work was performed in the same system used for the steady-state kinetic experiments, as shown in Fig. 1. This system is separate from the LEED/Auger instrument. In general, the surface of the catalyst was cleaned using the cleaning procedure developed for the steady-state kinetic experiments, as discussed in a previous section. A series of carbon monoxide thermal desorption spectra, as a function of ^{13}CO exposure, are shown in Figs. 11 and 12. At exposures less than 1.0 L, carbon monoxide desorbs in a first order process with a peak maximum at 425 K. At higher exposures, on the order of 5.0 L, a low temperature desorption peak is observed at about 373 K. The Rh(100) surface reaches saturation coverage of carbon monoxide at about 2.0 L, as shown in Fig. 13. The high temperature peak represents molecular adsorption at an atop site, while the low temperature shoulder indicates population of the surface by a bridge-bonded species. Assuming first order desorption kinetics for the desorption peak at 425 K, and a pre-exponential factor (ν) of 10^{13} Hz, with a heating rate (β) of 10.7 K/sec, the heat of desorption for the atop species was calculated using Eq. 29 (59). The result of this calculation is compared with previous results

$$\frac{\Delta H}{R\,T_{max}^{2}} = \frac{\nu}{\beta} \exp\left(\frac{-\Delta H}{R\,T_{max}}\right) \qquad (29)$$

in Table 1. The carbon monoxide desorption peak shapes are virtually identical to those reported by Castner et al. (7). In addition, those authors report a binding energy difference of 4 kcal/mole between the linear atop and bridge-bonded species. This difference, as measured by the 5.0 L desorption peak shown in Fig. 12(d), was calculated to be 3.2 kcal/mole for this study. The reason for the discrepancy in the absolute value for the heat of desorption is not clear. It is note-

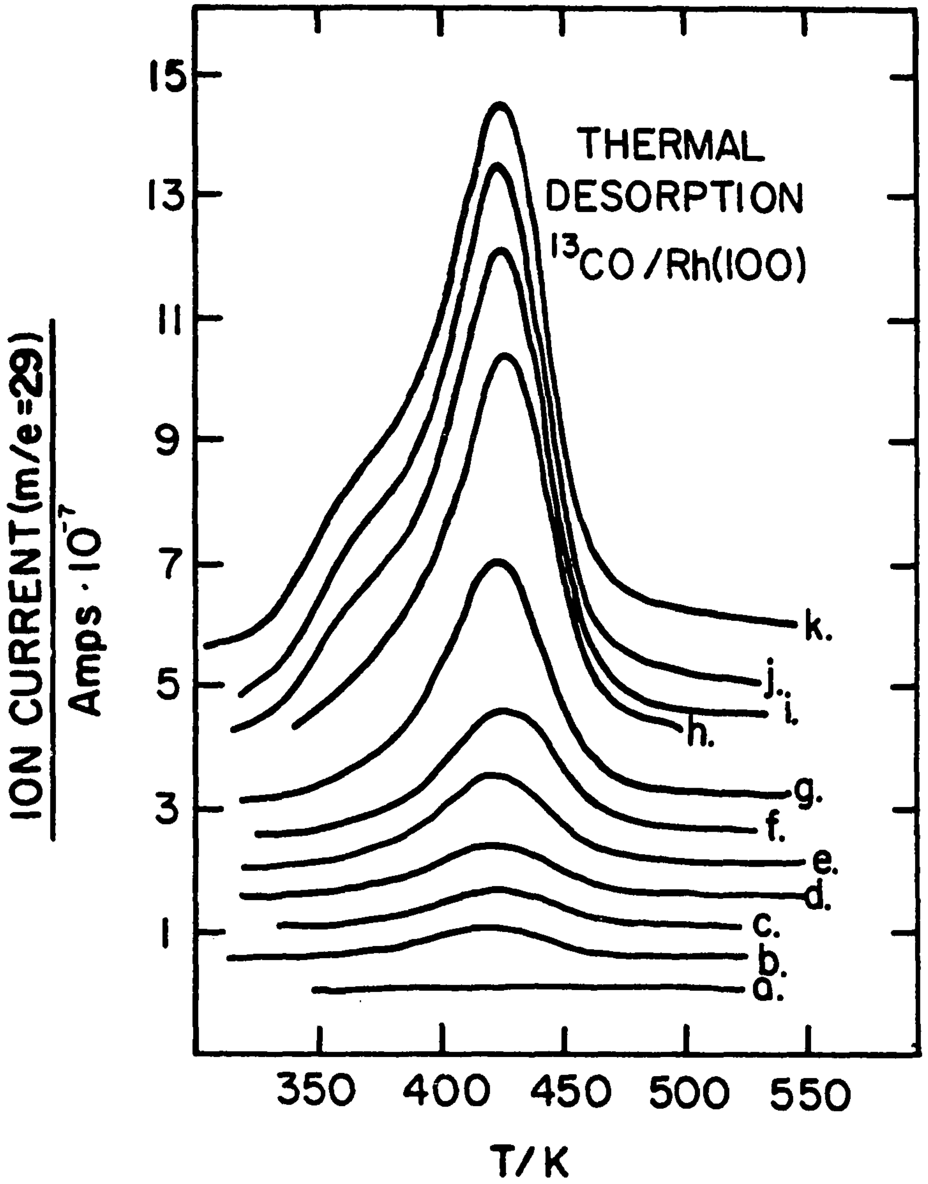

Figure 11. ^{13}CO thermal desorption spectra recorded with a heating rate β = 10.7 K/sec after various ^{13}CO exposures at 300 K: (a) background; (b) 0.01 L; (c) 0.02 L; (d) 0.05 L; (e) 0.10 L; (f) 0.22 L; (g) 0.50 L; (h) 1.02 L; (i) 2.02 L; (j) 5.20 L; (k) 10.1 L; curves have been shifted upward slightly for greater clarity

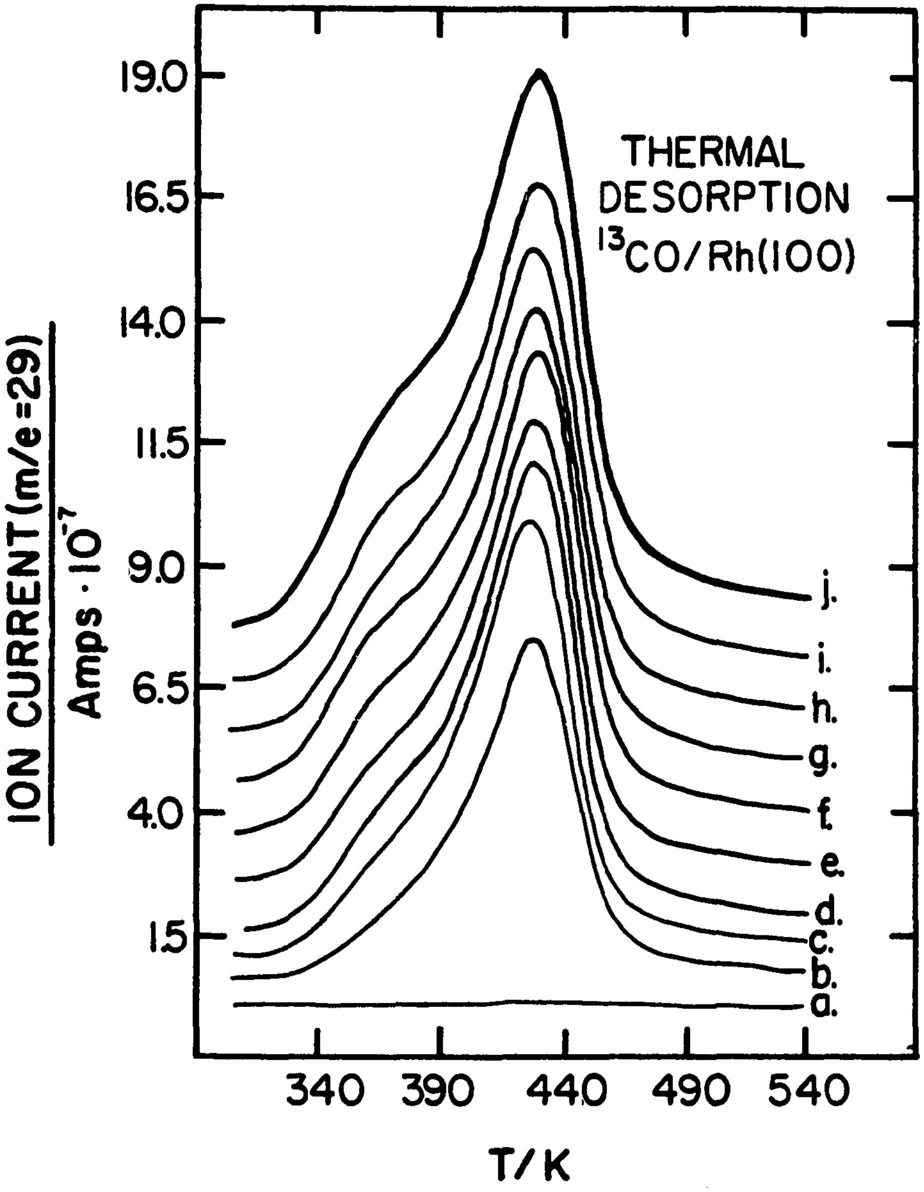

Figure 12. ^{13}CO thermal desorption spectra recorded with a heating rate β = 10.7 K/sec after various exposures with ^{13}CO at 300 K: (a) background; (b) 1.01 L; (c) 2.01 L; (d) 5.10 L; (e) 10.05 L; (f) 20.0 L; (g) 51.8 L; (h) 101.4 L; (i) 201.9 L; (j) 533 L; curves have been shifted upward slightly for better clarity

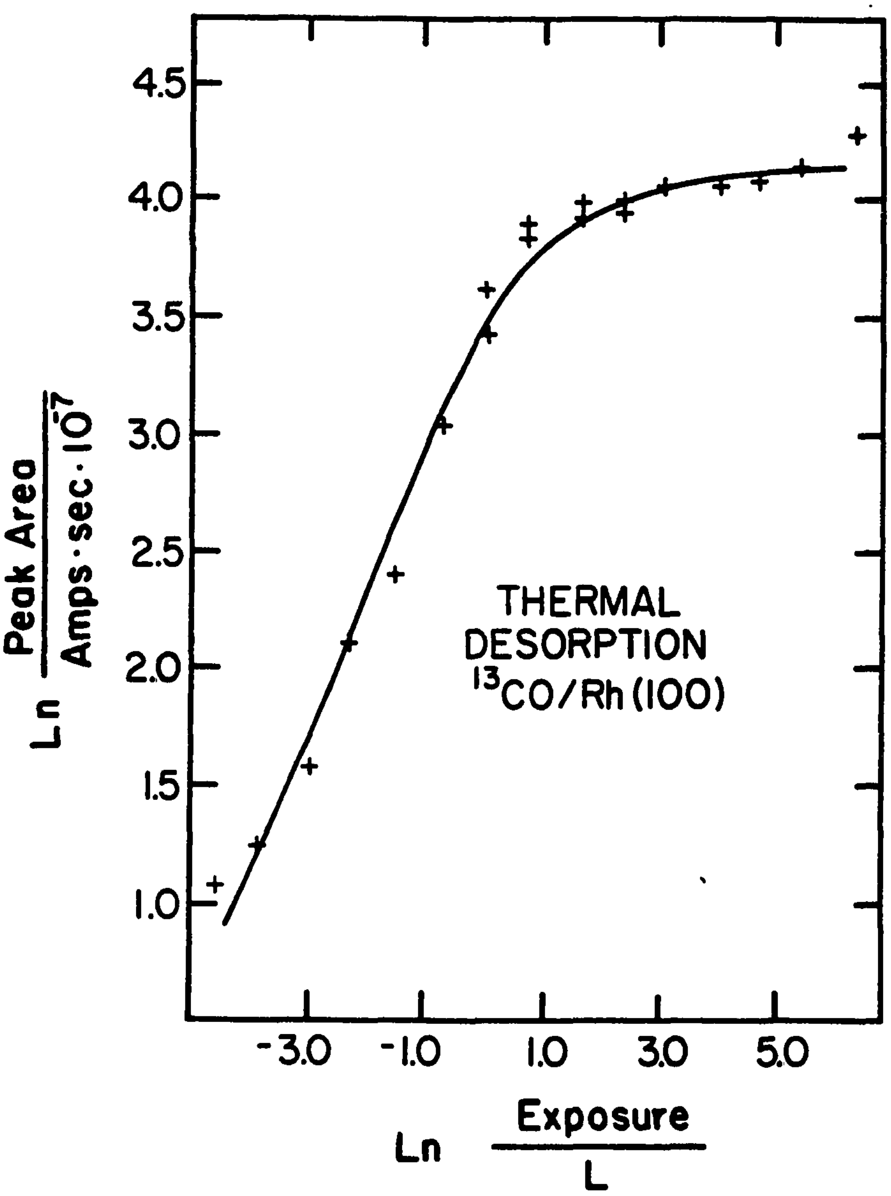

Figure 13. ^{13}CO desorption peak area-exposure relationship illustrating saturation exposure of about 2.0 L

worthy to mention that no evidence for the dissociation of carbon monoxide on the Rh(100) surface was observed.

Table 1. Carbon monoxide heat of desorption on various rhodium single crystal surfaces ($\nu = 10^{13}$ Hz)

Surface Orientation	Heat of Desorption (kcal/mole)	Reference
100	25.5	This work
100	29	7
110	29.7	8
111	31	7
polycrystalline wire	31.9	24

A series of thermal desorption experiments were performed to elucidate the adsorption-desorption characteristics of nitric oxide. The desorption peaks observed after a 0.11 L NO exposure of the catalyst surface are shown in Fig. 14. Nitric oxide desorption is somewhat more complex than that of carbon monoxide, however, several features are readily apparent after a close examination of Fig. 14. First, a large amount of the adsorbed nitric oxide desorbs in a molecular NO peak at 392 K. As mentioned previously, nitric oxide interacts strongly with the interior walls of well-baked UHV systems. This results in low pumping speed, which subsequently broadens the molecular nitric oxide desorption peak. In addition to this peak, two peaks with m/e = 28 are observed, a large desorption peak at 436 K, and a broad peak between 523 and 660 K. Due to the overlap of CO and N_2 at m/e = 28, it is necessary to rely on the respective cracking fragments for the determination of the identity of the m/e = 28 desorption peaks. It is clear,

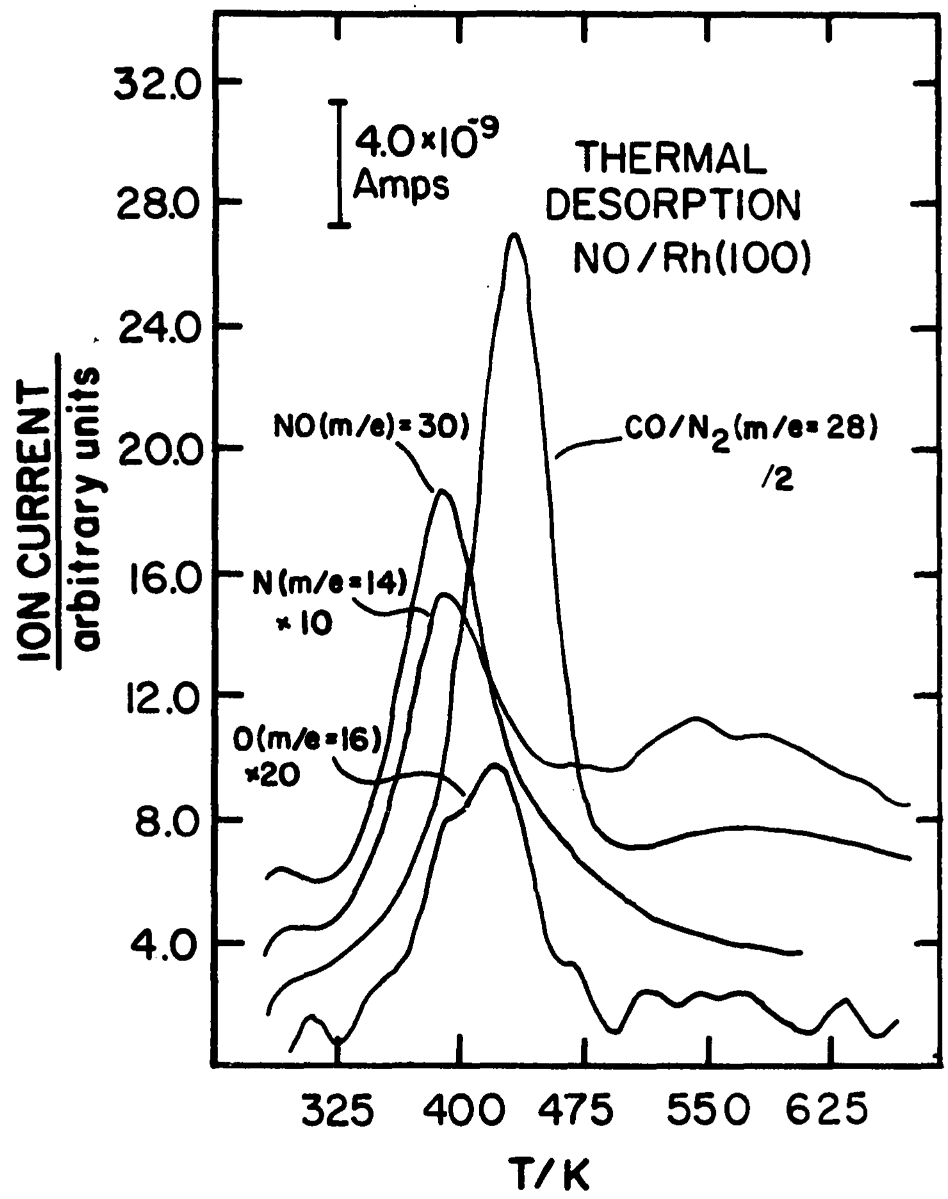

Figure 14. NO (m/e = 30), CO/N_2 (m/e = 28), N (m/e = 14), and O (m/e = 16) desorption spectra recorded after a 0.11 L NO exposure at 315 K and with a heating rate of β = 11.5 K/sec

after an examination of the atomic nitrogen peak at m/e = 14, that the m/e = 28 peak at 436 K represents carbon monoxide desorption from the sample. The calculated heat of desorption for the 436 K desorption peak, in Fig. 14, is 26.1 kcal/mole, which compares quite favorably with the heat of desorption of carbon monoxide of 25.5 kcal/mole, calculated from the results in Figs. 11 and 12. In addition, a peak area calculation of the 436 K desorption peak in Fig. 14, indicates that this feature is the result of an exposure of less than 0.008 L of carbon monoxide, which occurs due to the adsorption of background carbon monoxide gas. This is based upon the exposure-peak area relationship shown in Fig. 13. The broad m/e = 28 peak, between 523 and 625 K, clearly represents an increase in the partial pressure of molecular nitrogen, since both the m/e = 14 and m/e = 28 signals exhibit maxima in this region. Molecular nitrogen desorption peaks have been reported previously at 523 K for the Rh(110) surface (8), and a broad peak between 480 and 650 K for polycrystalline rhodium wire (6). The peak shape of the m/e = 14 desorption peak, between 523 and 625 K, is similar to the result from the polycrystalline wire. The amount of molecular nitric oxide desorbing from the polycrystalline wire surface was quite small, whereas the amount of molecular nitrogen desorbing from this wire surface was quite large (6). The situation for nitric oxide desorption from the Rh(100) surface, as shown in Fig. 14, is the reverse of that reported for the polycrystalline wire surface. It is clear, therefore, from these results, that the majority of the adsorbed nitric oxide desorbs as molecular nitric oxide at 392 K, during the temperature flash.

A series of nitric oxide desorption spectra, as a function of exposure, are shown in Fig. 15. The corresponding dependence of the desorption peak areas, also as a function of exposure, is shown in Fig. 16. Nitric oxide desorbs in a first order desorption peak with a peak maximum at 401 K. Assuming as before, a pre-exponential factor of 10^{13} Hz, this peak corresponds to a heat of desorption of 24.0 kcal/mole, as calculated using Eq. 29. This nitric oxide adsorption state saturates at about a 2.0 L exposure, as shown in Fig. 16. The heat of desorption for molecular nitric oxide from polycrystalline rhodium wire was reported to be 25 kcal/mole (6), and this compares quite favorably with the corresponding value for the Rh(100) surface calculated in this study. Due to the generally low signal and high background intensity, an order analysis of the molecular nitrogen desorption peak between 523 and 660 K was not possible.

These results complement those reported earlier for nitric oxide adsorption on polycrystalline rhodium wire (6), stepped rhodium single crystal surfaces, namely the Rh(331) (9,10) and Rh(755) (9), and the corrugated Rh(110) (8) single crystal surface. Thermal desorption results for the Rh(100) surface have not been reported previously. The general results of the above authors, for nitric oxide adsorption on these rhodium surfaces, are dissociative adsorption at low exposures (i.e., <1.0 L), and molecular adsorption at higher exposures (i.e., >1.0 L). In general, thermal desorption spectra from these polycrystalline, stepped, and corrugated surfaces indicate that very little molecular nitric oxide desorbs, even after a saturation exposure. For example,

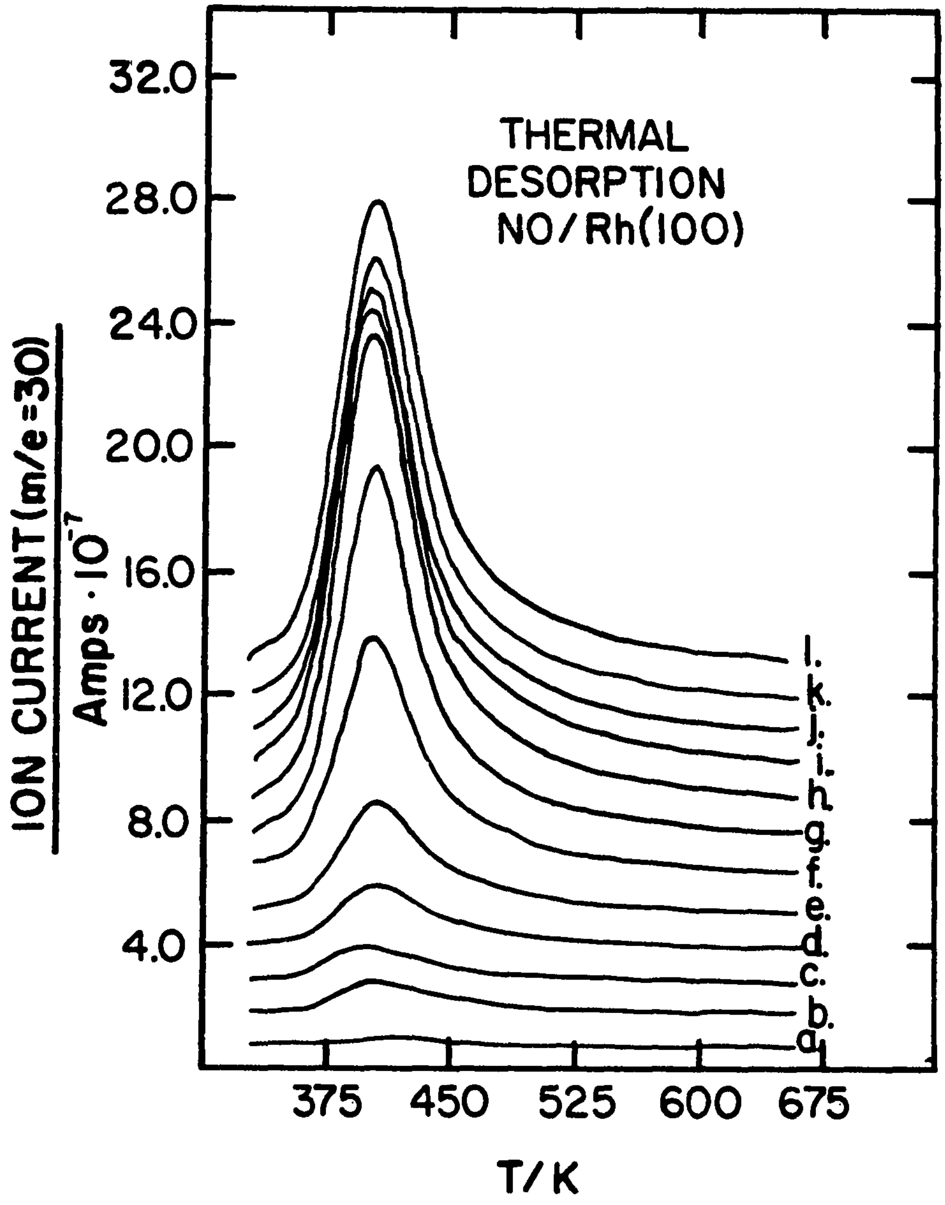

Figure 15. NO thermal desorption spectra recorded with a heating rate β = 11.6 K/sec after various NO exposures at 315 K: (a) background; (b) 0.01 L; (c) 0.02 L; (d) 0.104 L; (e) 0.21 L; (f) 0.51 L; (g) 0.99 L; (h) 1.99 L; (i) 5.00 L; (j) 10.1 L; (k) 19.9 L; (l) 49.8 L; curves have been shifted upward slightly for greater clarity

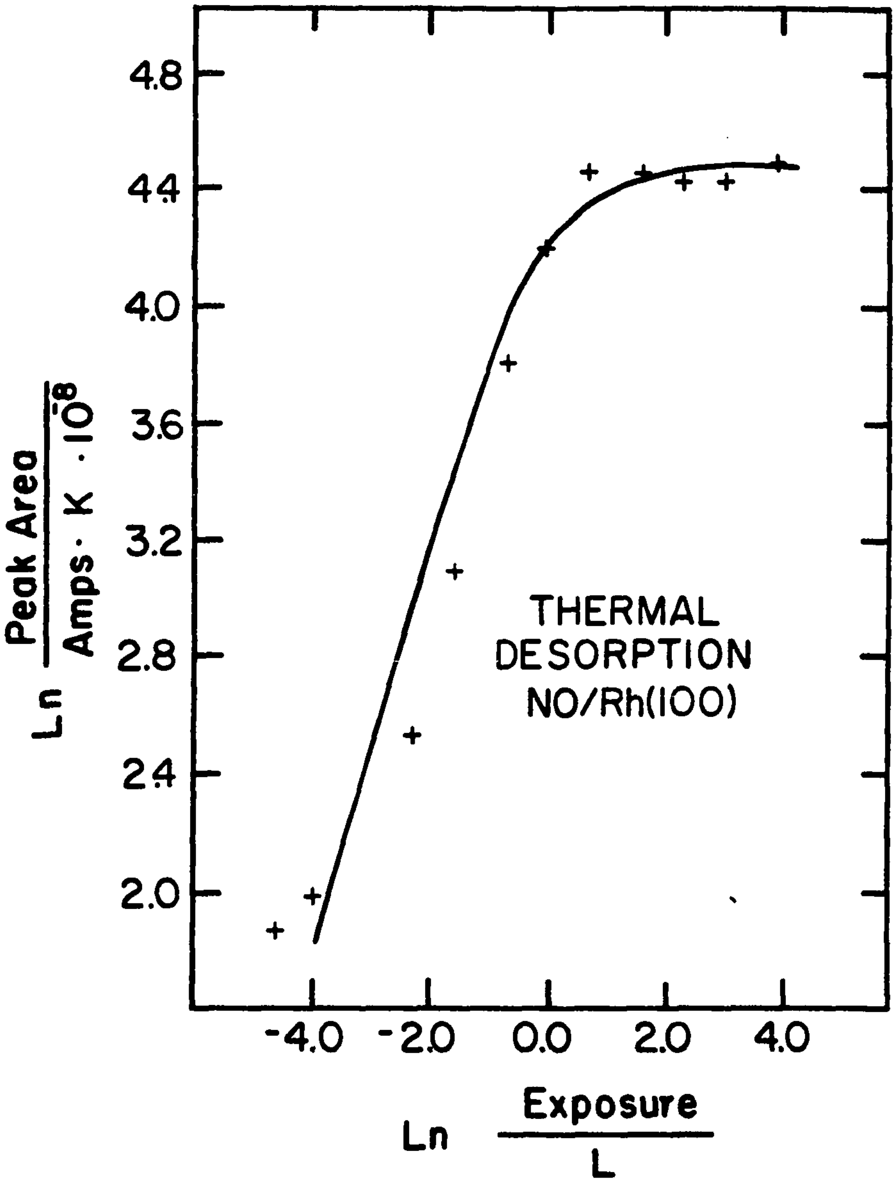

Figure 16. NO desorption peak area-exposure relationship illustrating saturation exposure of 2.0 L

no molecular nitric oxide desorbs during thermal desorption experiments on the Rh(110) surface for exposures less than 0.5 L, yet as shown in Fig. 15(b), a molecular nitric oxide peak is observed after only a 0.01 L exposure on the Rh(100) surface. This lack of a molecular NO desorption peak for the stepped, corrugated, and polycrystalline surfaces, is due primarily to dissociation that occurs during the flash, presumably according to equations 24 through 27. These results indicate that two competing processes are occurring on these rhodium surfaces, namely molecular nitric oxide adsorption-desorption as shown in Eq. 24, and nitric oxide dissociation as shown in Eq. 25. The relative rates of these two processes will depend upon the surface coverage, temperature, and structure. As discussed previously, periodic trends developed by Benziger (19), Broden et al. (17), and Miyaszki and Yasumori (18), place rhodium on the dividing line between molecular and dissociative nitric oxide adsorption. It is expected, therefore, that surface geometry would have an effect on the ability of rhodium surfaces to dissociate nitric oxide. In particular, one would expect that the more energetic surfaces (i.e., stepped, kinked, corrugated, and polycrystalline) would exhibit a greater tendency to dissociate nitric oxide, as compared to the smooth, low index Rh(100) surface. Therefore, the results reported in this study follow the expected plane-to-plane variation for nitric oxide adsorption on rhodium metal.

Finally, a comparison of Figs. 10 and 14 clearly illustrates the competition between nitric oxide molecular adsorption-desorption and surface dissociation. In particular, Fig. 10 clearly indicates primarily nitric oxide dissociation, as the temperature is increased in a step-wise manner, whereas Figs. 14 and 15 illustrate primarily molecular adsorption-desorption. It is clear that molecular desorption and surface dissociation are competing processes, and both the Auger and thermal desorption experiments illustrate evidence for the occurrence of each process. For example, thermal desorption results shown in Fig. 14 indicate a molecular nitrogen desorption peak at about 523 K, which is the same temperature as the precipitous drop in intensity of the nitrogen KLL Auger line. In a similar fashion, the intensity of the nitrogen KLL Auger line exhibits a small decrease in intensity between 373 and 473 K, corresponding favorably with the molecular nitric oxide desorption peak, shown in Fig. 14, at 392 K. Evidently the slow step-wise heating procedure used for the experiment described in Fig. 10 favors the dissociation process, but the rapid temperature rise used during the thermal desorption procedure favors molecular desorption.

The adsorption-desorption properties of carbon dioxide follow the same pattern as reported by Castner et al. (7). In particular, no carbon dioxide was detected desorbing from the Rh(100) surface, even after exposures of 100 L. Only carbon monoxide was detected during the thermal desorption experiments, indicating dissociative adsorption according to Eq. 30. A series of desorption spectra as a function of exposure are

$$CO_2\ (g) + 2{*} \longrightarrow CO\ (ads) + O\ (ads) \qquad (30)$$

shown in Fig. 17, and the corresponding dependence of peak area as a function of exposure is shown in Fig. 18. Both of these figures show features virtually identical to the carbon monoxide desorption results

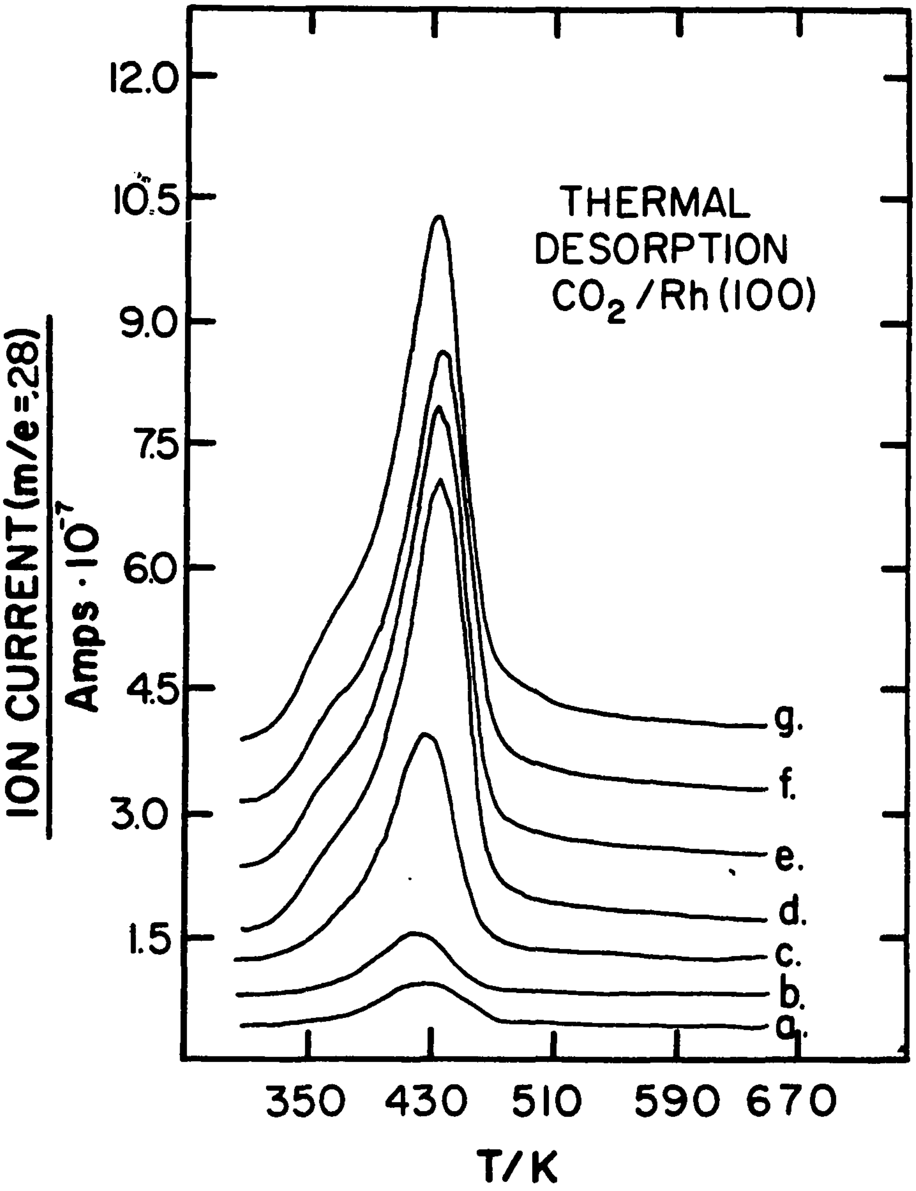

Figure 17. CO (m/e = 28) desorption spectra recorded with a heating rate β = 11.6 K/sec after various CO_2 (m/e = 44) exposures at 300 K: (a) 0.01 L; (b) 0.10 L; (c) 1.00 L; (d) 9.85 L; (e) 19.8 L; (f) 50.0 L; (g) 99.8 L; curves have been shifted upward slightly for greater clarity

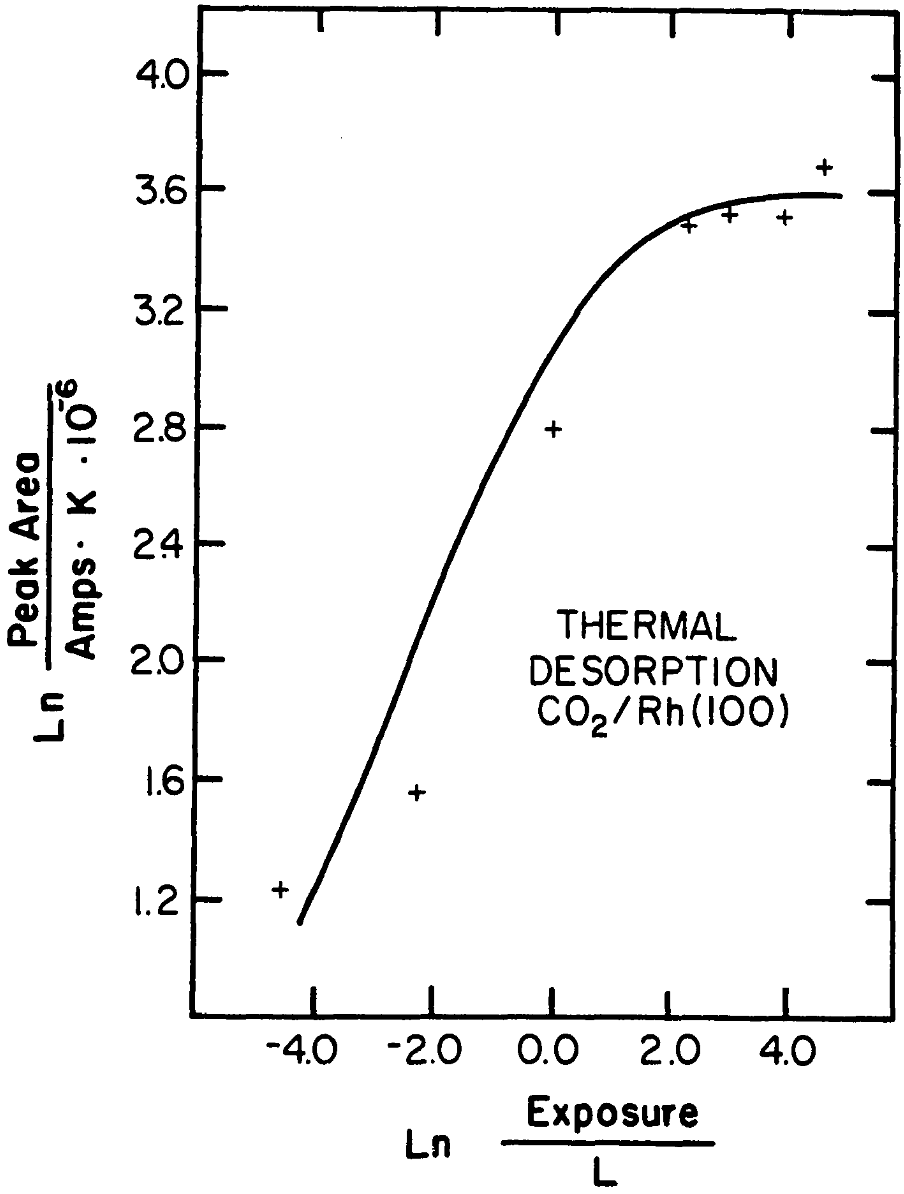

Figure 18. CO desorption peak area-exposure relationship following CO_2 exposure illustrating saturation at 10 L

shown in Figs. 11-13, except that a 5-fold higher exposure, for CO_2 versus CO, is necessary for both the appearance of the low temperature shoulder and for saturation exposure. The desorption peak at 428 K, shown in Fig. 17, follows first order desorption kinetics, and indicates a heat of adsorption of 25.4 kcal/mole, calculated assuming a pre-exponential of 10^{13} Hz using Eq. 29. This value is identical to that calculated previously for carbon monoxide desorption. It is noteworthy to mention that the adsorbed oxygen, produced according to Eq. 30, was not subsequently observed in the desorption spectra as O_2, but preferred to diffuse into the bulk. This oxygen diffusion effect has been a common experience during adsorption-desorption studies of oxygen-containing species on rhodium surfaces (7,33).

Although nitrogen does not generally adsorb on rhodium surfaces, adsorption has been observed after thermal activation of gas phase molecular nitrogen (35). All attempts to adsorb nitrogen in this manner failed, most probably due to the low temperature of the thoriated-iridium ion gauge filament used for the thermal activation, and a lack of a line-of-site geometry between the filament and the crystal sample. For this reason, thermal desorption spectra for molecular nitrogen adsorption could not be obtained.

Several conclusions can be made at this point, with respect to the reduction of nitric oxide with carbon monoxide on the Rh(100) single crystal surface. First, the carbon monoxide reactant is expected to interact with this surface in a purely molecular fashion, serving simply to reduce some surface oxygen species, produced by the interaction of nitric oxide with the catalyst surface. In other words, the mechanism of the NO/CO process probably does not involve dissociation of adsorbed carbon monoxide. This would be consistent with the thermal desorption and Auger experiments. The interaction of nitric oxide with the catalyst surface under reaction conditions is not clear, at this point. It is apparent that both molecular and dissociated nitric oxide should play a role in the NO/CO process, however, the relative amount of each is not clear. The amount of dissociation is expected to depend upon the gas phase composition, and the result of the interactions between the adsorbed species on the catalyst surface, under reaction conditions. In addition, the products typically produced, namely N_2 and CO_2, are expected to have little effect upon the reaction rate as measured in this study. This is clear because molecular nitrogen simply will not adsorb to the catalyst surface under reaction conditions and, thus, will desorb quickly once formed during the NO/CO reaction. In addition, since the steady-state kinetic study will be concerned with intial rates, the amount of carbon dioxide produced will be quite small. Thermal desorption results clearly indicate that the sticking coefficient of CO_2 is smaller than the sticking coefficient of either carbon monoxide or nitric oxide. Therefore, once the CO_2 product is produced in the gas phase, it will not be able to effectively compete for surface sites in the large partial pressure background of NO and CO. For this reason, it is expected that the CO_2 produced during the kinetic measurements will not inhibit the initial reaction rate. As described in a previous section, the reaction rate initially determined in the steady-state reaction system was quite low and irreproducible using a cleaning procedure of simply annealing the sample, or heating the sample in oxygen. This effect is most likely due to the segregation of boron to the surface, which acts as a surface poison, blocking active sites and inhibiting surface diffusion. From the Auger results, it was determined that both high temperature annealing and oxidation promote boron surface segregation. Finally, the Auger experiment of a simulated 1:1 reaction mixture indicated that the surface of the catalyst is not extensively oxidized, under these reaction conditions.

Kinetic Results

The steady-state kinetics of nitric oxide reduction with carbon monoxide was studied over a wide range of initial conditions. The objectives of this investigation were to establish the reactant and product orders, over a wide variation in partial pressures, and to examine the temperature dependence of the reaction rate. This wide variation in initial conditions is necessary in heterogeneous kinetics, because reactant orders are necessarily a function of partial pressure. In keeping with the practical applications of this study, with respect to automotive exhaust catalysis, it should be noted that the partial pressures of NO and CO present in a typical exhaust stream (i.e., 1.3 and 670 Pa, respectively) are in the range of this study (5). In addition, the steady-state kinetic data was collected at 688 K, which is also in the temperature range of automobile exhausts (5). From the determination of reaction orders, together with the surface characterization results, a consistent mechanism for the reduction of nitric oxide with carbon monoxide will be developed.

The reaction rate as a function of carbon monoxide partial pressure, at a constant nitric oxide partial pressure of 57.5 Pa and a constant reaction temperature of 688 K, is shown in Fig. 19. As expected, the carbon monoxide order is a function of carbon monoxide partial pressure. In particular, the carbon monoxide order is approximately first order in the partial pressure range from 1.3 to 5.0 Pa. Between 5.0 and 54.0 Pa, the order with respect to carbon monoxide gradually decreases to zero, and finally between 54.0 and 250 Pa, the carbon monoxide order is inverse first order. This dependence on carbon monoxide partial pressure is typical of Langmuir-Hinshelwood heterogeneous kinetics. In particular, the first order dependence in the observed reaction rate in the low pressure region is the result of increasing amounts of adsorbed CO, relative to the adsorbed NO, leading to a corresponding increase in reaction rate. On the other hand, the inverse first order dependence, in the observed reaction rate in the high pressure region, is the result of CO blocking the sites necessary for NO adsorption, thus decreasing the reaction rate.

The reaction rate as a function of nitric oxide partial pressure, at the constant carbon monoxide partial pressure of 44.0 Pa and a constant reaction temperature of 688 K, is shown in Fig. 20. The nitric oxide order plot illustrates a behavior very similar to that of the carbon monoxide order plot. In particular, the order with respect to nitric oxide is 1.5, in the partial pressure range between 1.5 and 20 Pa, gradually decreasing to zero order, and finally decreasing to approximately inverse first order between 400 and 1800 Pa. The nitric oxide

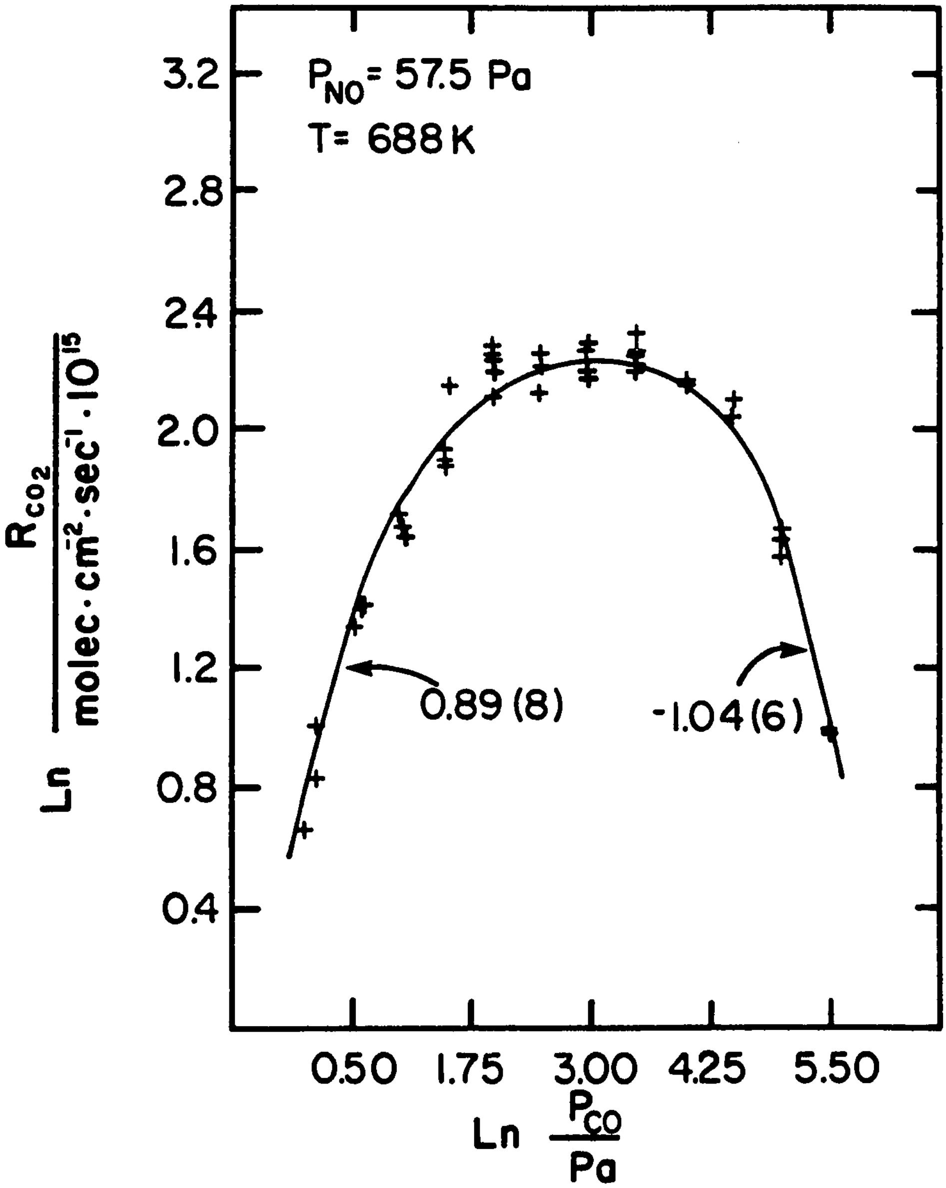

Figure 19. Carbon monoxide order plot determined using a constant nitric oxide pressure of 57.5 Pa at 688 K. The numbers shown represent limiting orders for the high and low pressure regions with errors in the last place given in parentheses

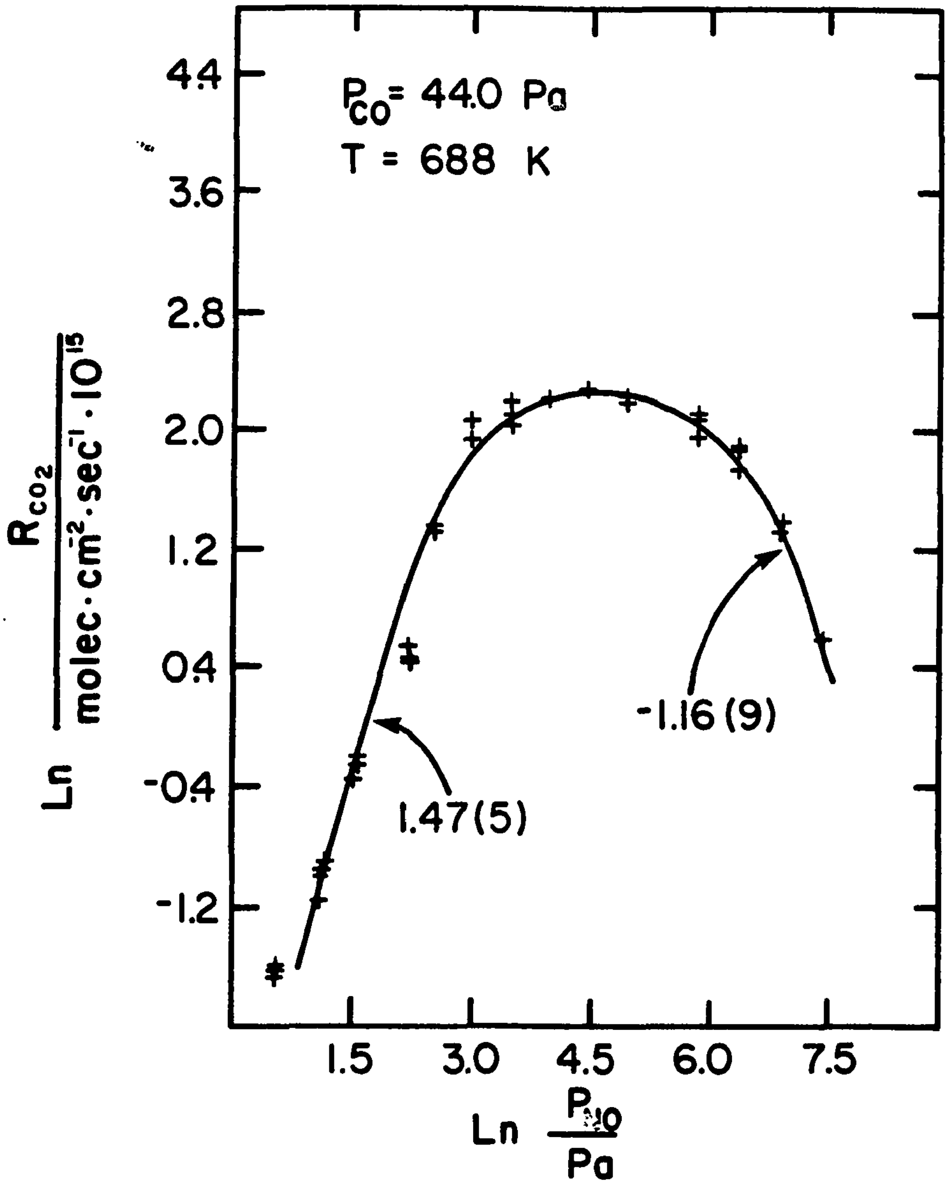

Figure 20. Nitric oxide order plot determined using a constant carbon monoxide pressure of 44.0 Pa at 688 K, limiting orders are shown as in Fig. 19

order plot together with the carbon monoxide order plot implies that the reduction of nitric oxide with carbon monoxide follows Langmuir-Hinshelwood kinetics.

The dependence of the reaction rate, as a function of the partial pressure of each of the reaction products, was determined; these data are shown in Figs. 21 and 22. The reaction order with respect to the partial pressure of nitrogen is zero, over the partial pressure range between 1-200 Pa, as expected since molecular nitrogen will not chemisorb on the catalyst surface under reaction conditions. In other words, the molecular nitrogen produced during the reduction of nitric oxide with carbon monoxide desorbs rapidly and does not inhibit the rate of reaction. In a similar fashion, the order with respect to carbon dioxide is also zero, over the partial pressure range 1-200 Pa. This is also the expected result, since carbon dioxide would not be able to compete effectively for surface sites, in the presence of carbon monoxide and nitric oxide. These two order plots imply that under these reaction conditions, the elementary reaction steps directly involved in the formation of reaction products are essentially irreversible.

The temperature dependence of the reaction rate is shown in Fig. 23, in the form of a standard Arrhenius plot. The temperature behavior of the reaction rate does not produce a straight line on the Arrhenius plot, and this is not unusual for a heterogenous catalytic reaction (60). The slope of a tangent to this curve, at any given temperature, is proportional to the apparent activation energy of this process. In particular, the apparent activation energy at 688 K (i.e., the

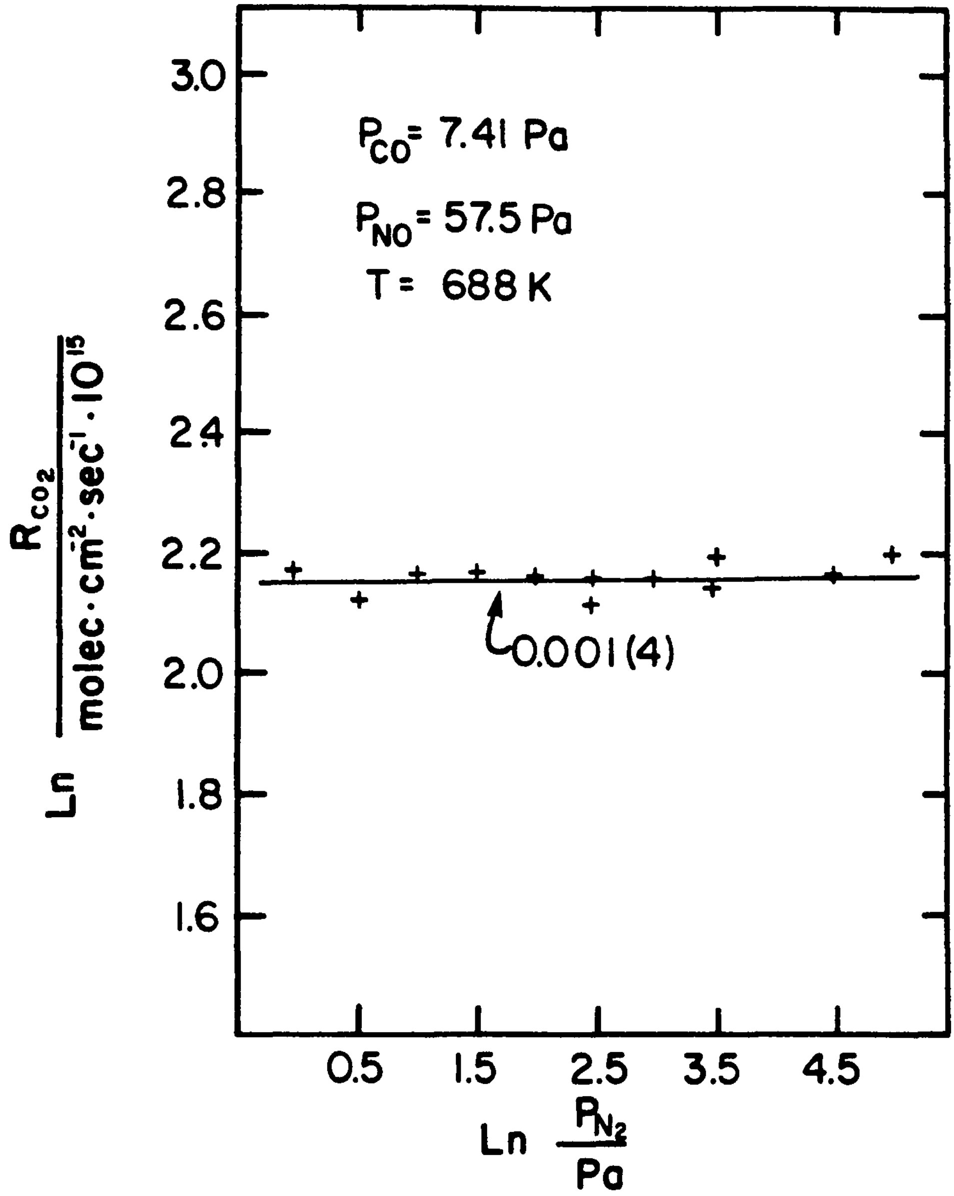

Figure 21. Nitrogen order plot determined using a constant carbon monoxide pressure of 7.41 Pa and a constant nitric oxide pressure of 57.5 Pa at 688 K. The number shown (with error estimate) indicates zeroth order as calculated by a linear least squares fit of the rate data

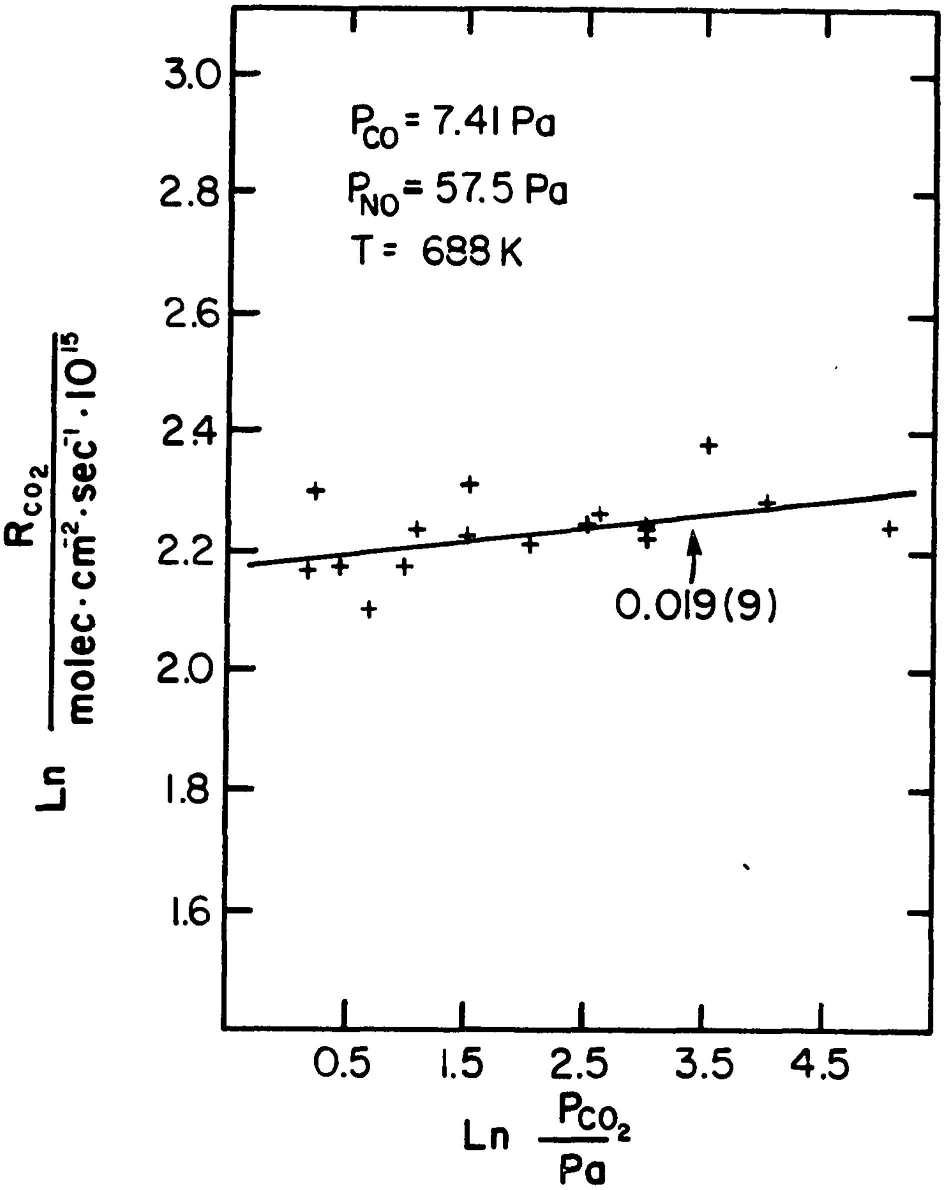

Figure 22. Carbon dioxide order plot determined using a constant carbon monoxide pressure of 7.41 Pa and a constant nitric oxide pressure of 57.5 Pa at 688 K. The number shown (with error estimate) indicates zeroth order as calculated by a linear least squares fit of the rate data

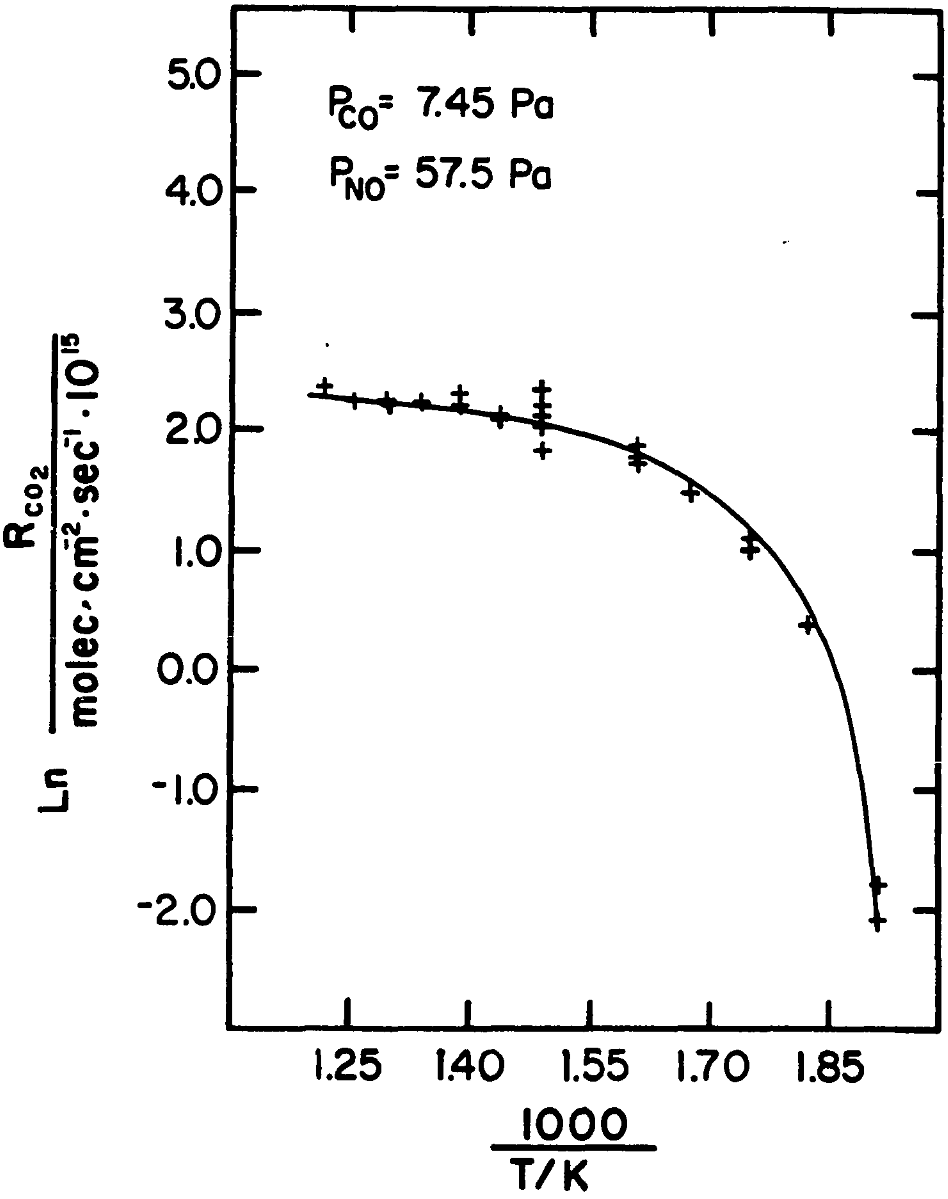

Figure 23. Temperature dependence of reaction rate using a constant carbon monoxide pressure of 7.45 Pa and a constant nitric oxide pressure of 57.5 Pa

temperature used for the collection of the reactant/product order plots) is approximately 3.2 kcal/mole. As temperature decreases, the apparent activation energy increases at constant initial gas phase composition. This effect is primarily due to the inability of nitric oxide to displace carbon monoxide at these lower temperatures. A similar effect has been reported for the NO/CO reaction on polycrystalline rhodium wire (6).

Mechanistic Considerations

It is clear that in order to develop a complete understanding of the reduction of nitric oxide with carbon monoxide a multi-technique approach is required. This investigation utilized numerous techniques to elucidate mechanistic details from which a consistent mechanism was developed.

As a starting point for examining the proposed mechanism of the NO/CO process, it is useful to consider a recently proposed mechanism, as given in Eqs. 31-35 (10). This mechanism has been supported by AES,

$$\mathrm{CO\ (g)} + * \Longleftrightarrow \mathrm{CO\ (ads)} \qquad (31)$$

$$\mathrm{NO\ (g)} + * \Longleftrightarrow \mathrm{NO\ (ads)} \qquad (32)$$

$$\mathrm{NO\ (ads)} + * \xrightarrow{\text{slow}} \mathrm{N\ (ads)} + \mathrm{O\ (ads)} \qquad (33)$$

$$2\ \mathrm{N(ads)} \xrightarrow{\text{fast}} \mathrm{N_2\ (g)} + 2\ * \qquad (34)$$

$$\mathrm{CO\ (ads)} + \mathrm{O\ (ads)} \xrightarrow{\text{fast}} \mathrm{CO_2\ (g)} + 2\ * \qquad (35)$$

TDS, and HREELS results on the Rh(331) single crystal surface (10). In particular, a HREELS spectrum, taken after a 1.0 L NO exposure and subsequent flash to 450 K, revealed the existence of a surface oxide via the Rh-O energy loss peak at 520 cm^{-1}. The absence of surface nitrogen after this procedure was confirmed with AES. These results imply that under the conditions of this experiment (i.e., ultra-high vacuum and 450 K), Eq. 34 is a fast process. Relative rate measurements on polycrystalline rhodium wire clearly illustrate that the NO/CO process, to produce N_2 and CO_2, is slower than the CO/O_2 process to produce CO_2 (6,24). Assuming that both of these processes proceed via a step similar to Eq. 35, then step 33 would be rate limiting for this mechanism of the NO/CO process. The rate law for this mechanism would then be given by:

$$\text{Rate} = \frac{d\,P_{CO_2}}{dt} = k_{33}\,[NO]_{*}[*] \qquad (36)$$

where [*] denotes the concentration of vacant active sites, and $[NO]_{*}$ denotes the fractional surface coverage of adsorbed nitric oxide. Utilizing the site balance given in Eq. 37, and applying the usual

$$1.0 = [*] + [CO]_{*} \rightarrow [NO]_{*} + [N]_{*} + [O]_{*} \qquad (37)$$

steady-state assumptions, the reaction rate equation in terms of the reactant partial pressures can be derived, and is given in Eq. 38. This mechanism is supported primarily by spectroscopic evidence at a total pressure in the 6.7×10^{-5} Pa range. There are currently no steady-state kinetic data which support this mechanism.

$$\frac{d\,P_{CO_2}}{dt} = \frac{k_{33}K_{32}P_{NO}}{\left(1.0 + K_{31}P_{CO} + K_{32}P_{NO} + \left(\frac{K_{32}k_{33}}{2\,k_{34}}\right)^{1/2} P_{NO}^{1/2} + \frac{K_{32}k_{33}}{K_{31}k_{35}}\frac{P_{NO}}{P_{CO}}\right)^2} \qquad (38)$$

A close examination of Eq. 38 indicates that the order with respect to carbon monoxide depends upon the partial pressure of carbon monoxide, at constant partial pressure of NO. In particular, the CO order should vary between +2.0 at low P_{CO}, and -2.0 at high P_{CO}. The nitric oxide order changes in a similar fashion between +1.0 at low P_{NO}, and -1.0 at high P_{NO}, at constant P_{CO}. A comparison between the limiting orders predicted by Eq. 38 and the limiting orders as observed in this kinetic study, shown in Figs. 19 and 20, clearly demonstrates an inconsistency. In particular, the 3/2 order with respect to nitric oxide, at low P_{NO} and constant P_{CO}, suggests that the mechanism of the reduction of nitric oxide with carbon monoxide is more complex than the mechanism given in Eqs. 31-35. In addition, the direct reaction between

$$\text{CO (ads)} + \text{NO (ads)} \longrightarrow CO_2\text{ (g)} + \text{N (ads)} + * \qquad (39)$$

$$2\text{ N (ads)} \longrightarrow N_2\text{ (g)} + 2\,* \qquad (40)$$

adsorbed CO and NO as described in Eqs. 39 and 40 also implies a nitric oxide order which varies as a function of P_{NO} between +1.0 and -1.0. This mechanism is also not consistent with the observed kinetic orders, as shown in Figs. 19 and 20.

It is well-known that for supported rhodium catalysts, at lower temperatures, the products of the NO/CO process include carbon dioxide, nitrous oxide, and nitrogen (15,61,62). Thus, it would be reasonable to include a nitrous oxide intermediate in the NO/CO process, as given in Eqs. 41-46. Assuming a steady-state formalism, together with the site

$$\mathrm{CO\ (g)} + * \Longleftrightarrow \mathrm{CO\ (ads)} \tag{41}$$

$$\mathrm{NO\ (g)} + * \Longleftrightarrow \mathrm{NO\ (ads)} \tag{42}$$

$$2\ \mathrm{NO\ (ads)} \Longleftrightarrow \mathrm{N_2O\ (ads)} + \mathrm{O\ (ads)} \tag{43}$$

$$\mathrm{N_2O\ (ads)} + \mathrm{CO\ (ads)} \longrightarrow \mathrm{N_2\ (g)} + \mathrm{CO_2\ (g)} + 2\ * \tag{44}$$

$$\mathrm{O\ (ads)} + \mathrm{NO\ (ads)} \longrightarrow \mathrm{NO_2\ (ads)} + * \tag{45}$$

$$\mathrm{NO_2\ (ads)} + \mathrm{CO\ (ads)} \longrightarrow \mathrm{CO_2\ (g)} + \mathrm{NO\ (g)} + 2\ * \tag{46}$$

balance given in Eq. 47, the rate equation can be easily derived as given in Eq. 48. The parameters given in this equation, namely A, B, G, E,

$$1.0 = [*] + [\mathrm{CO}]_* + [\mathrm{NO}]_* + [\mathrm{N_2O}]_* + [\mathrm{NO_2}]_* + [\mathrm{O}]_* \tag{47}$$

$$\mathrm{Rate} = \frac{d\,P_{CO_2}}{dt} = \frac{F\,P_{NO}^{3/2}\,P_{CO}^{1/2}}{\left(1.0 + A\,P_{CO} + B\,P_{NO} + G\,P_{NO}^{3/2}/P_{CO}^{1/2} + E\,P_{CO}^{1/2}\,P_{NO}^{1/2}\right)^2} \tag{48}$$

and F, represent collections of rate and equilibrium constants, as given by Eqs. 49-53.

$$A = K_{41} \tag{49}$$

$$B = K_{42} \tag{50}$$

$$G = \left(\frac{K_{42}^3 K_{43} k_{45}}{K_{41} k_{44}}\right)^{1/2} + \left(\frac{K_{42}^3 K_{43} k_{44} k_{45}}{K_{41} k_{46}^2}\right)^{1/2} \qquad (51)$$

$$E = \left(\frac{K_{41} K_{42} K_{43} k_{44}}{k_{45}}\right)^{1/2} \qquad (52)$$

$$F = (K_{41} K_{42}^3 K_{43} k_{44} k_{45})^{1/2} \qquad (53)$$

The limiting orders predicted by Eq. 48 with respect to nitric oxide for the low and high partial pressure extremes are +3/2 and -3/2, respectively. These limits are consistent with the experimental order plot shown in Fig. 20, assuming, of course, that the high partial pressure limit was not reached experimentally. Similarly, the limiting orders with respect to carbon monoxide, predicted by Eq. 48, namely +3/2 to -3/2, are also consistent with the experimental order plot given in Fig. 19, assuming once again that the extremes were not reached experimentally. The final test of the compatibility of the rate equation given in Eq. 48, and the experimental reaction rate data, would be a parametric fit of the data to the rate equation.

The complexity of Eq. 48 requires the fitting procedure to be accomplished via a nonlinear least squares analysis. The algorithm used to fit Eq. 48 to the experimental data has been described by Haskell and Jones (63), and simply consists of a nonlinear least squares analysis based upon grid minimization. During the fitting procedure, it was determined that the values of the terms in the denominator containing the partial pressure variables were large compared to 1.0. This fact forces Eq. 48 to be rearranged, as shown in Eq. 54, with the loss of a degree of freedom.

$$R_{CO_2} = \frac{P_{NO}^{3/2}\, P_{CO}^{1/2}}{\left(\frac{A}{F^{1/2}} P_{CO} + \frac{B}{F^{1/2}} P_{NO} + \frac{G}{F^{1/2}} \frac{P_{NO}^{3/2}}{P_{CO}^{1/2}} + \frac{E}{F^{1/2}} P_{CO}^{1/2}\, P_{NO}^{1/2}\right)^2} \qquad (54)$$

The best obtainable fit of Eq. 54, with chemically reasonable values (i.e., positive values) for the fitting parameters, is given in Figs. 24 and 25, for the carbon monoxide and nitric oxide order plots, respectively. The numerical values of the fitting parameters used for the calculated curves, shown in Figs. 24 and 25, are shown in the left-hand column of Table 2. As shown in these figures, the mechanism developed in Eqs. 41-46 quite adequately models the experimental data over the entire range of initial conditions, except in the limit of high nitric oxide partial pressure. In general, however, the model is quite satisfactory in the sense that it fits the experimental rate data.

Table 2. Values of the constants used to fit the experimental order plots to the derived steady-state rate laws

Constant	Value Determined for the Best Fit to Equation 54 ($sec^{\frac{1}{2}}$ $molecule^{-\frac{1}{2}}$ cm)	Value Determined for the Best Fit to Equation 65 ($sec^{\frac{1}{2}}$ $molecule^{-\frac{1}{2}}$ cm)
$A/F^{1/2}$	5.78×10^{-9}	5.78×10^{-9}
$B/F^{1/2}$	4.62×10^{-9}	4.63×10^{-9}
$G/F^{1/2}$	4.26×10^{-10}	3.57×10^{-10}
$E/F^{1/2}$	0.0	0.0
$H/F^{1/2}$	---	1.08×10^{-12}

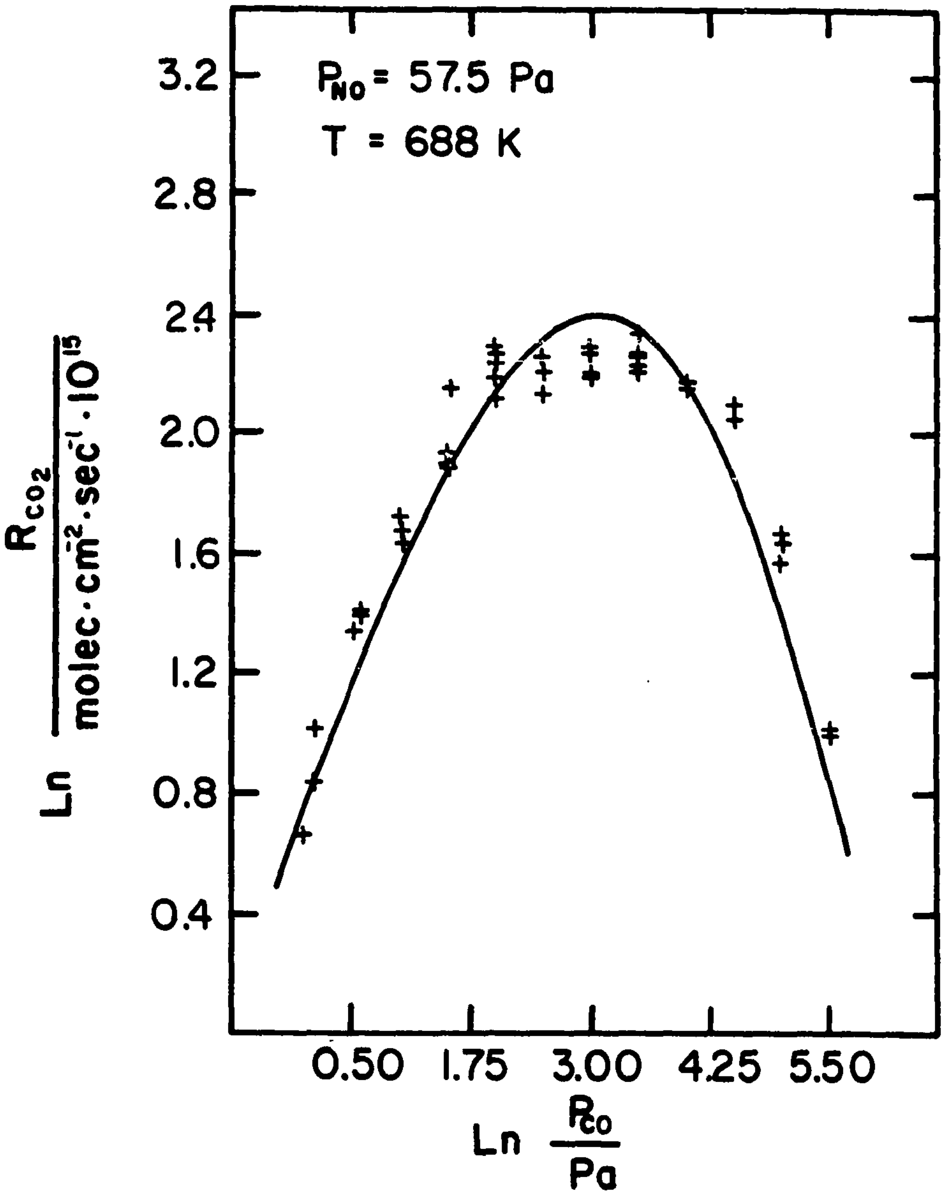

Figure 24. Theoretical fit of carbon monoxide order plot to Eq. 54. The parameter values used for the calculated curve are given in Table 2

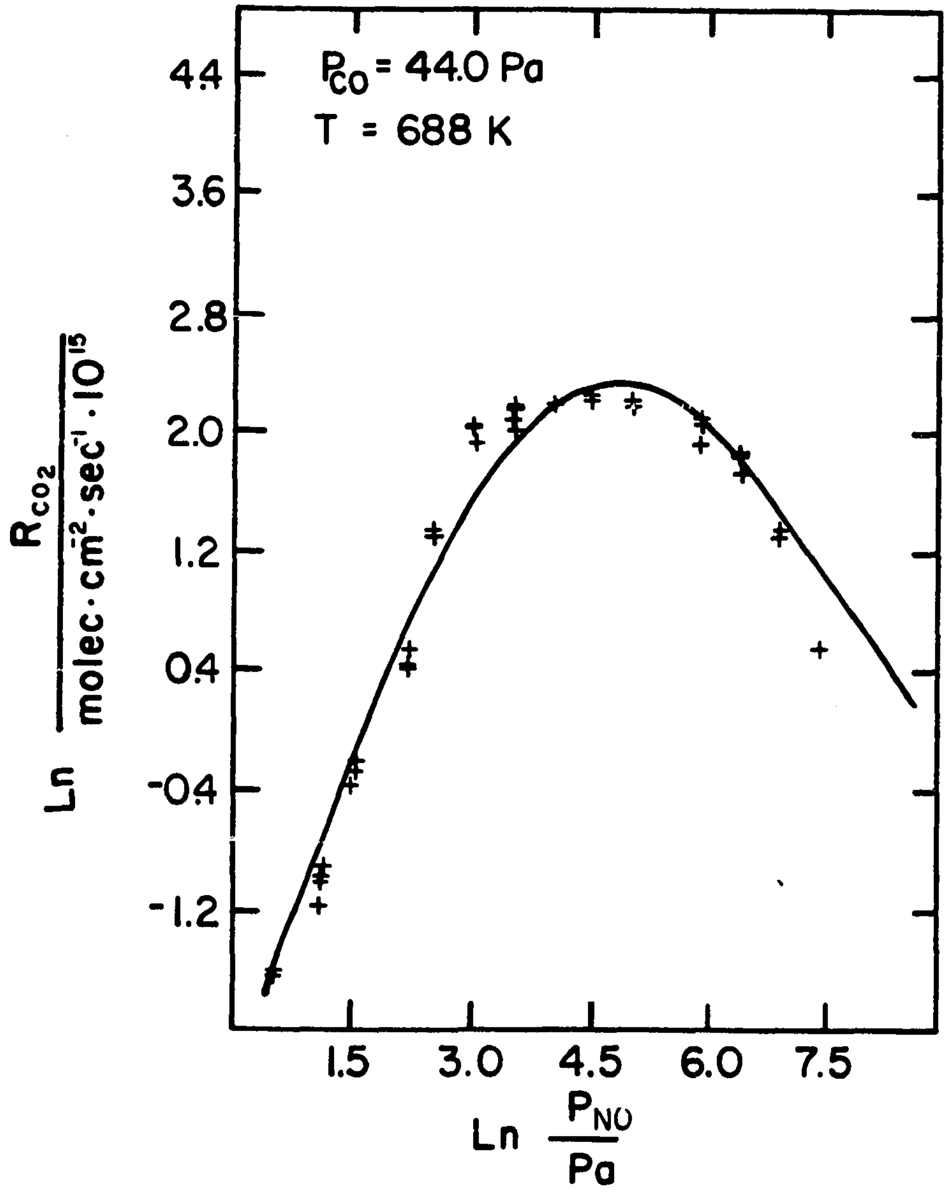

Figure 25. Theoretical fit of nitric oxide order plot to Eq. 54. The parameter values used for the calculated curve are given in Table 2

The physical significances of the parameter values and of Eq. 54 are not obvious. The fact that the terms in the denominator are large compared to 1.0 indicates that the number of vacant active sites is quite small under reaction conditions. This is primarily due to the large flux of reactant molecules impinging on the surface ($\sim 10^{21}$ molecules/sec cm^2), as compared to the total number of active sites available ($\sim 10^{15}$ atoms/cm^2). Each remaining term in the denominator is proportional to the concentration of a reaction intermediate, as given in Eqs. 55-58. From the values given in the left-hand column of Table 2,

$$\frac{\underset{*}{[CO]}}{[*]} = A\, P_{CO} \tag{55}$$

$$\frac{\underset{*}{[NO]}}{[*]} = B\, P_{NO} \tag{56}$$

$$\frac{\underset{*}{[N_2O]}}{[*]} + \frac{\underset{*}{[NO_2]}}{[*]} = G\, \frac{P_{NO}^{3/2}}{P_{CO}^{1/2}} \tag{57}$$

$$\frac{\underset{*}{[O]}}{[*]} = E\, P_{CO}^{1/2}\, P_{NO}^{1/2} \tag{58}$$

it is clear that the surface is covered primarily by adsorbed molecular carbon monoxide and nitric oxide. Due to the number of steps in the reaction mechanism (i.e., 6 steps which yield 6 constants, 3 equilibrium constants and 3 rate constants), it is impossible to solve explicitly for any of the thermodynamic or kinetic constants in the proposed mechanism, via the values of the fitting parameters. It is possible to calculate a ratio of equilibrium constants, as shown in Eq. 59. In particular, this ratio corresponds to the quotient of the equilibrium constant for CO adsorption by that for NO adsorption.

$$\frac{K_{41}}{K_{42}} = \frac{A/F^{1/2}}{B/F^{1/2}} = 1.25 \tag{59}$$

It is possible to theoretically estimate this ratio using a simple Langmuir competitive adsorption model (i.e., adsorption without adsorbate-adsorbate interactions and without chemical reaction). The equilibrium constants are given by Eqs. 60 and 61. The rate constant for Langmuir adsorption can be calculated using the kinetic theory of gases as shown in Eq. 62, where N_a is Avogadro's number, n_o is the surface atom density, M_i is the molecule weight of the i^{th} component of the gas phase, S_i is the sticking coefficient of the i^{th} component, and T is the absolute temperature of the gas phase (64). The rate constant for desorption is given by Eq. 63, where A is the pre-exponential factor, typically assumed to be 10^{13} Hz, and E_{d_i} is the activation energy of

$$K_{41} = \frac{k_{a_{CO}}}{k_{d_{CO}}} \tag{60}$$

$$K_{42} = \frac{k_{a_{NO}}}{k_{d_{NO}}} \tag{61}$$

$$k_{a_i} = \frac{S_i\, N_a}{n_o} (2\pi\, M_i\, R\, T)^{-1/2} \tag{62}$$

$$k_{d_i} = A\, e^{-E_{d_i}/RT} \tag{63}$$

desorption. As a first approximation, $k_{a_{CO}} = k_{a_{NO}}$, and utilizing the heat of desorption as determined from TDS experiments, shown in Figs. 11 and 15, the ratio of these equilibrium constants can be calculated as shown in Eq. 64. The agreement of this value to that determined from

$$\frac{K_{41}}{K_{42}} = \frac{k_{d_{NO}}}{k_{d_{CO}}} = 3.0 \tag{64}$$

the fitting parameters is quite good, in light of the assumptions made during the calculation of the value given in Eq. 64.

As mentioned previously, the mechanistic model described in Eqs. 41-46 does not adequately fit the dependence of the reaction rate at high nitric oxide partial pressures. From an empirical point of view, the reaction rate decreases in this region faster than the theory predicts. Thus, a higher order P_{NO} term would be necessary in the denominator of Eq. 54, for the theory to appropriately model the experimental data. Such an equation is given by:

$$R_{CO_2} = \frac{P_{NO}^{3/2}\, P_{CO}^{1/2}}{\left(\frac{A}{F^{1/2}} P_{CO} + \frac{B}{F^{1/2}} P_{NO} + \frac{G}{F^{1/2}} \frac{P_{NO}^{3/2}}{P_{CO}^{1/2}} + \frac{E}{F^{1/2}} P_{CO}^{1/2}\, P_{NO}^{1/2} + \frac{H}{F^{1/2}} P_{NO}^{2}\right)^2} \tag{65}$$

where the $H/F^{1/2}\, P_{NO}^2$ term has been added in the denominator. Such a term would arise as the result of the addition of Eq. 66 to the reaction

$$2\ \mathrm{NO\ (ads)} \Longleftrightarrow \underset{*}{(\mathrm{NO})_2} + * \qquad (66)$$

mechanism given in Eqs. 41-46, where H would consequently be as shown in Eq. 67. This intermediate might have the form described in Eq. 68. This surface structure has been supported previously by Ibach and Lehwald (65) using HREELS, although these results are a subject of controversy (66). The best obtainable fit of the experimental data to Eq. 65 is shown in Figs. 26 and 27, and the values of the fitting parameters are shown in Table 2. As shown in Fig. 26, the fit of the carbon monoxide order plot is essentially identical to the fit shown in Fig. 24, however, the fit of Eq. 65 to the nitric oxide order plot indicates significant improvement in the high NO partial pressure region. This was expected since Eq. 65 was designed to have this effect. In addition, the existence of the intermediate given in Eq. 68 is debatable. Alternately, the breakdown of the kinetic model, given in Eqs. 41-46, at high nitric oxide partial pressures might be the result of adsorbate-adsorbate interactions.

$$H = K_{66}\, K_{42}^{2} \qquad (67)$$

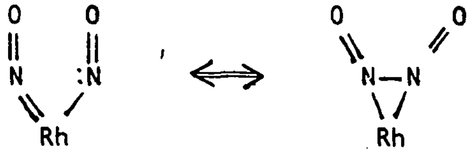

(68)

This mechanism is also consistent with the surface characterization results. In particular, the thermal desorption analysis of carbon monoxide implies that under reaction conditions, a molecular adsorption-

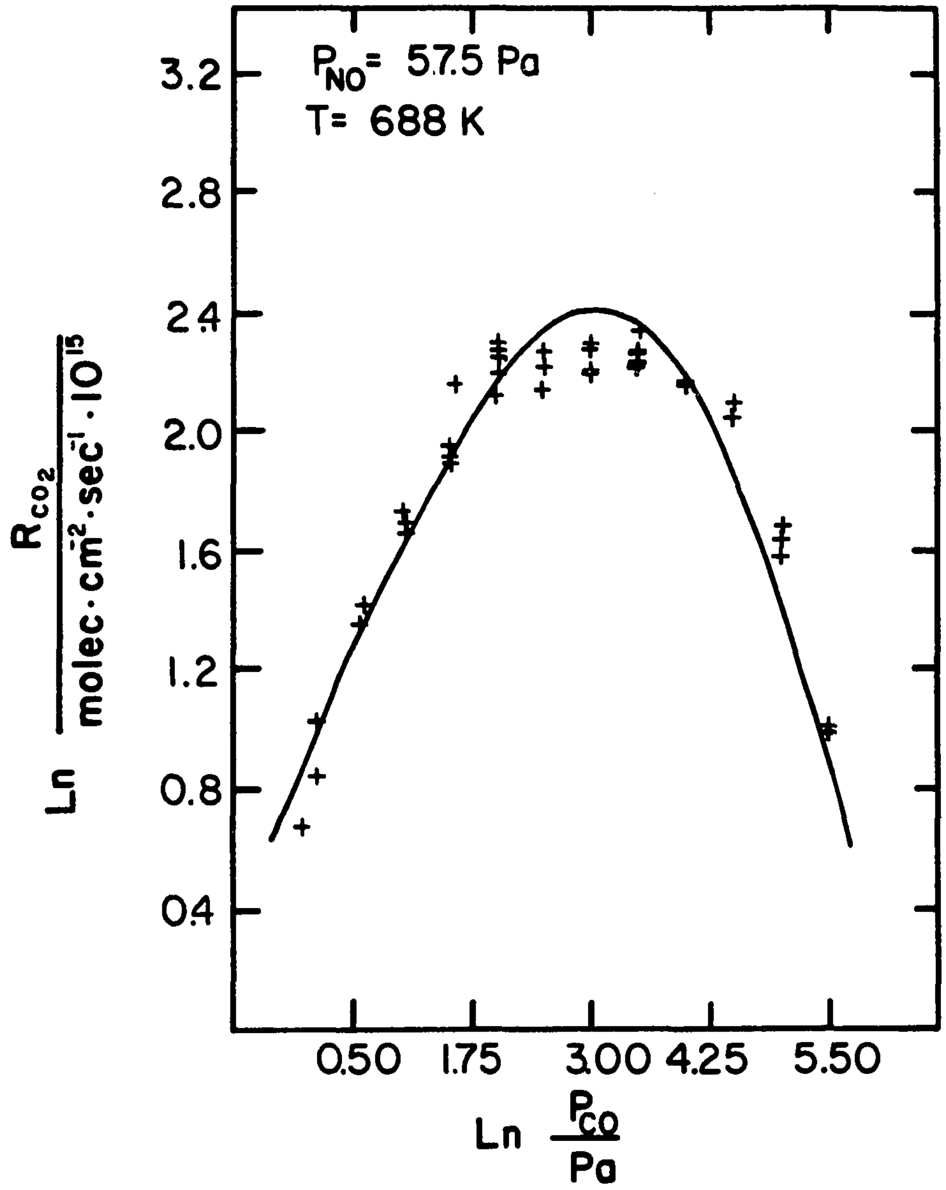

Figure 26. Theoretical fit of carbon monoxide order plot to Eq. 65. The parameter values used for the calculated curve are given in Table 2

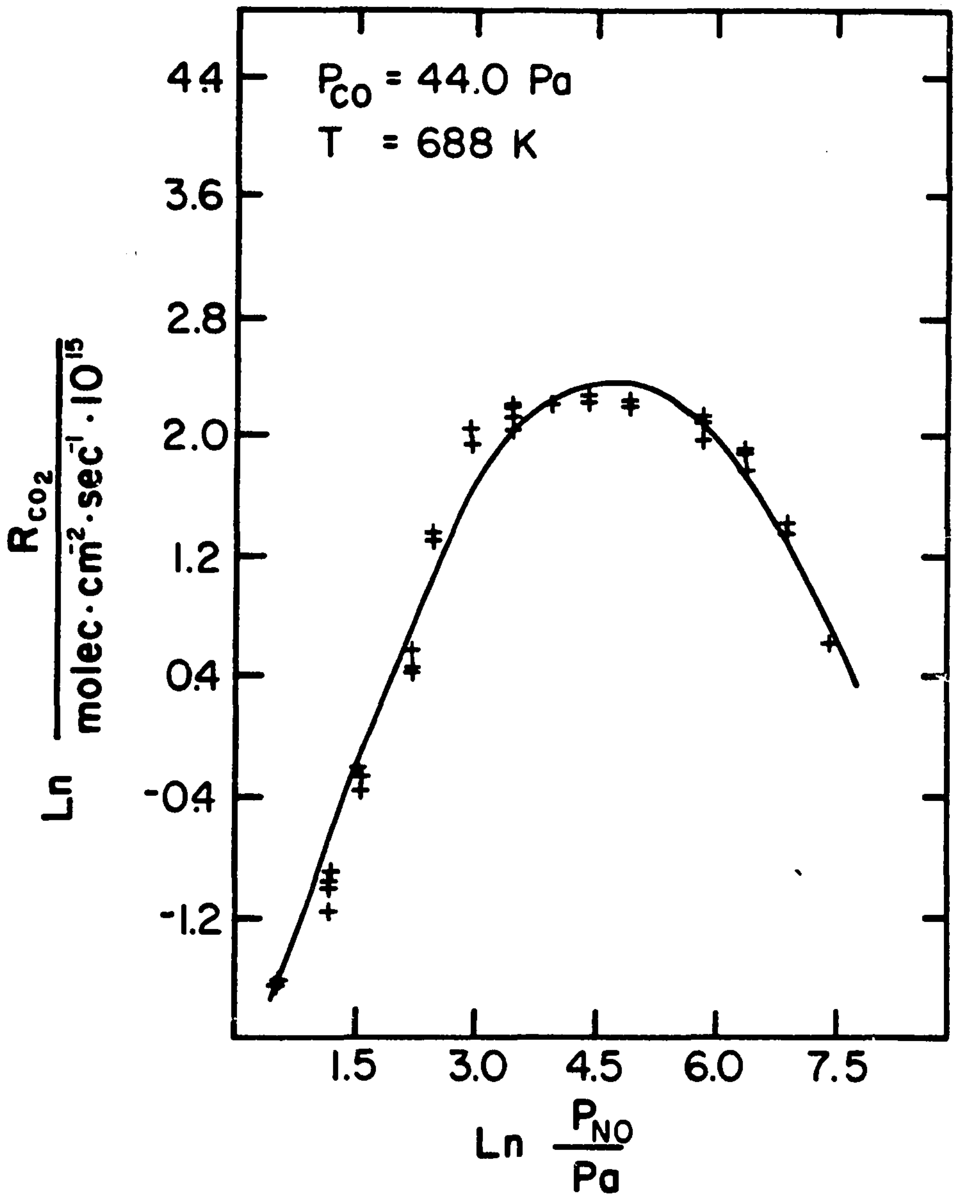

Figure 27. Theoretical fit of nitric oxide order plot to Eq. 65. The parameter values used for the calculated curve are given in Table 2

desorption equilibrium would prevail. This is indeed the case in the proposed mechanism according to Eq. 41. In other words, carbon monoxide does not dissociate under these reaction conditions. In addition, Auger experiments, described previously, suggested that the catalyst surface was not extensively oxidized under reaction conditions. The concentration of adsorbed oxygen as a function of the reactant partial pressures is given in Eq. 58. Since the value for the parameter E determined during the fitting procedure was essentially zero, then the concentration of adsorbed oxygen as predicted by the kinetic model is also zero, in agreement with the Auger results. These results are in disagreement with earlier results which indicate that adsorbed oxygen plays an important role in the NO/CO process (6,10). This is primarily due to the fact that the earlier studies were performed at a total pressure of approximately 6.7×10^{-5} Pa. The flux of reactant molecules to the surface at this pressure is low enough that the fraction of vacant active sites is relatively high. This permits the dissociation of nitric oxide to occur according to Eq. 69. Under the reaction conditions

$$\mathrm{NO\ (ads)} + * \longrightarrow \mathrm{N\ (ads)} + \mathrm{O\ (ads)} \qquad (69)$$

of this study, however, the reactant partial pressures are relatively high (i.e., 13 Pa) and the fraction of vacant active sites is quite low. This would clearly inhibit the dissociation of nitric oxide. Thus, it is not surprising that the kinetic data collected in this investigation cannot be described by the mechanism proposed earlier for the low pressure studies.

A determination of the rate limiting step of this reaction is not possible from the steady-state reaction data collected during this investigation. The reason for this fact lies within the proposed mechanism. In particular, the rate law given in Eq. 48 can be derived by assuming any of the irreversible steps (i.e., Eqs. 44, 45, or 46) in the mechanism as rate limiting. Therefore, this analysis cannot determine the rate limiting step of this reaction mechanism. This model, however, does imply the irreversibility of reaction steps given in Eqs. 44, 45, and 46. The irreversibility of Eqs. 44 and 46 is supported directly by the experimental product order plots, shown in Figs. 21 and 22. These order plots illustrate a zeroth order dependence of the reaction rate with respect to each product and, therefore, steps 44 and 46 must be irreversible. The irreversibility of step 45 lacks any direct experimental evidence. However, if Eq. 45 is established as an equilibrium process, the resulting rate law does not model the experimental data in an acceptable manner.

Throughout this discussion an asterisk has been used to denote a catalytic active site. While the exact nature of this site cannot be determined from the experimental evidence presented here, it is useful to examine possible structures of the reaction intermediates. Assuming an active site to be a single rhodium atom, then reasonable structures can be postulated for each of the reaction intermediates, as given in Eqs. 70-74. As shown in Eq. 70, carbon monoxide can adsorb in two possible sites, namely the linear atop site or the bridge-bonded site. These two sites correlate well with the TDS results discussed in the

CO (ads)

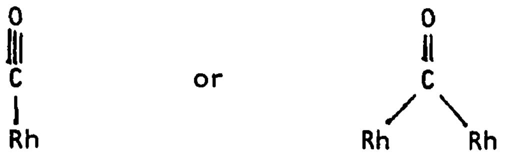

(70)

NO (ads)

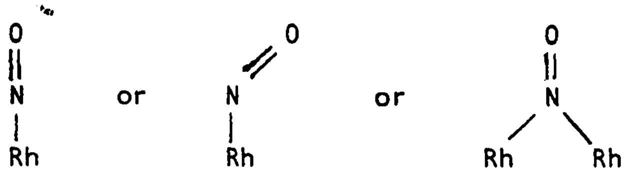

(71)

O (ads)

(72)

N_2O (ads)

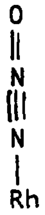

(73)

NO_2 (ads)

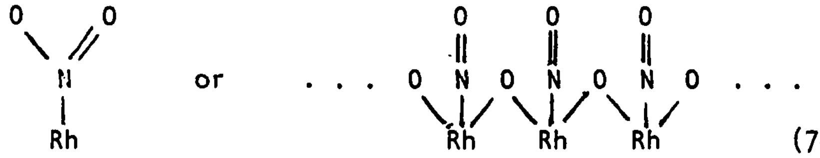

(74)

previous section, and with LEED/Auger, HREELS, and IR results widely reported in the literature (7,8,14,20,24,27-30). The adsorption of nitric oxide on the Rh(331) surface has been recently studied by Dubois et al. (10). These authors reported evidence using HREELS for both the bent and linear nitrosyls with the predominant species being the bent configuration; these are shown in Eq. 71. Several other geometries of nitric oxide bonding to transition metal surfaces have been reported previously, including a bridge-bonded species and the formation of surface NO^- and NO^+ species (11,14,15,65,66). In the work discussed above, Dubois et al. (10) commented that HREELS results for the Rh(111) surface suggested the formation of at least five different adsorbed nitric oxide species. Oxygen adsorption on rhodium surfaces has been studied by numerous authors (7,9,24,25,33,56), and the bonding geometries shown in Eq. 72 have been proposed. Reasonable structures for the nitrous oxide and nitrogen dioxide species are shown in Eqs. 73 and 74. It is noteworthy to mention that the formation of adsorbed nitrous oxide and nitrogen dioxide species have been observed via IR after the interaction of carbon monoxide and nitric oxide on Rh/Al_2O_3 (14). Thus, it seems quite reasonable to include these intermediates in the reduction of nitric oxide with carbon monoxide on the Rh(100) surface.

The mechanism presented in Eqs. 41-46 is consistent with both the steady-state kinetic and surface characterization results. This kinetic model is relatively simple, however, it is probably not unique. The fact that the derived rate law is consistent with the experimental data provides only a necessary, but not sufficient, condition that this model is the correct mechanism. The mechanism proposed in Eqs. 41-46 is indeed remarkable, in that it fits experimental results collected over three orders of magnitude change in reactant partial pressure. It should be noted, however, that the criterion of a clean surface for the steady-state kinetic, and thermal desorption experiments, was necessarily that which gave a high and reproducible rate of reaction. A reproducible reaction rate, however, does not necessarily imply a perfectly clean surface. The cleaning procedure used during the steady-state kinetic study (i.e., 12.0 Pa H_2, 415°C, 10 minutes, followed by 650°C, 10 minutes) would be expected to remove most surface contaminants so that impurities should not have significantly affected the kinetic order determinations.

CONCLUSIONS AND SUGGESTIONS FOR FUTURE RESEARCH

The reduction of nitric oxide with carbon monoxide was studied using numerous techniques including steady-state reaction kinetics, Auger electron spectroscopy, low energy electron diffraction, and thermal desorption spectroscopy. In the reactant partial pressure range between 1 and 1800 Pa, the reaction between carbon monoxide and nitric oxide was selective towards production of carbon dioxide and molecular nitrogen. The initial reaction rate at 688 K varied between 10^{15} and 10^{16} molecule cm^{-2} sec^{-1}, depending upon the initial gas phase composition. The kinetic orders for each of the reactants and products were determined over a partial pressure change of several orders of magnitude. In particular, the carbon monoxide order, at constant nitric oxide partial pressure, varied from +1 to -1 as the partial pressure of carbon monoxide was increased. In a similar fashion, the nitric oxide order, at constant carbon monoxide partial pressure, varied from +3/2 to approximately -1 as the partial pressure of nitric oxide was increased. This dependence of reactant orders clearly indicates that the NO/CO process proceeds via a Langmuir-Hinshelwood mechanism, involving a rate limiting reaction between two adsorbed species. The kinetic order with respect to the reaction products, namely N_2 and CO_2, was determined to be zero over the product partial pressure range between 1 and 200 Pa. This result indicates that the elementary reaction steps directly involved with product formation are essentially irreversible, under the reaction conditions studied. The temperature dependence of the reaction rate indicated an apparent activation energy of 3.2 kcal/mole at 688 K. In addition, this activation energy increased with decreasing temperature, due to the inability of nitric oxide to displace carbon monoxide at temperatures lower than approximately 500 K.

Surface characterization results indicated that carbon monoxide molecularly adsorbed, at 300 K with a high sticking coefficient, on the Rh(100) surface in two different sites, namely the linear atop and bridge-bonded site. The linear atop species desorbed with first order kinetics, with an activation energy of desorption of 25.5 kcal/mole. The bridge-bonded species also desorbed with first order kinetics, with an activation energy of 22.3 kcal/mole. No evidence was found for dissociative carbon monoxide adsorption. Nitric oxide molecularly adsorbed at 300 K with a high sticking coefficient on the Rh(100) surface, with an activation energy of desorption of 24.0 kcal/mole. Thermal desorption spectra, taken at a heating rate of 11.6 K/sec, illustrated primarily molecular desorption, with a peak temperature of 401 K. On the other hand, Auger results demonstrated that the nitric oxide adsorbate undergoes surface dissociation, if the Rh(100) surface is heated in a slow step-wise fashion. These results indicate that nitric oxide molecular adsorption-desorption and surface dissociation are competing processes on the Rh(100) surface. Thermal desorption spectra taken after CO_2 adsorption illustrated only CO desorption. This indicated that a dissociation process was occurring, most probably upon adsorption. The CO desorption peak, observed after CO_2 adsorption, behaved in the same way as the CO desorption peak observed after CO adsorption, except that a 5-fold higher CO_2 exposure was necessary for saturation.

The surface characterization and steady-state kinetic results were modeled by a Langmuir-Hinshelwood reaction between molecularly adsorbed carbon monoxide and an adsorbed nitrous oxide or nitrogen dioxide species. A rate law was derived from the proposed mechanism utilizing the standard steady-state approximations. This rate law fit the experimental kinetic data over a three order of magnitude change in reactant partial pressure, except in the limit of high nitric oxide partial pressure. A slight modification to the mechanism allowed even this region of the data to be fit successfully.

Future investigations of the reduction of nitric oxide with carbon monoxide might include HREELS analysis of a catalyst surface after exposure to reaction conditions similar to those used in this study (i.e., 10 Pa, 688 K). This could be accomplished using a high pressure isolation cell contained within a HREELS spectrometer. In order to more fully characterize the effect of surface structure on reaction mechanism, a steady-state kinetic study of the NO/CO process on the Rh(110) or Rh(331) surface would be invaluable.

LITERATURE CITED

1. B. Harrison, M. Wyatt and K. G. Gough, in Catalysis (The Royal Society of Chemistry, Burlington House, London, 1982), Vol. 5, Chap. 4.

2. E. Robinson, J. Air Pollut. Control Assoc. 20, 303 (1970).

3. A. Amirnazmi and M. Boudart, J. Catal. 39, 383 (1975).

4. W. F. Egelhoff, Jr., in The Chemical Physics of Solid Surfaces and Heterogeneous Catalysis, edited by D. A. King and Woodruff (Elsevier Scientific Publishing Company, New York, 1982). Vol. 4, Chap. 9.

5. J. Wei, Advances in Catalysis 24, 57 (1975).

6. C. T. Campbell and J. M. White, Appl. Surf. Sci. 1, 347 (1978).

7. D. G. Castner, B. A. Sexton and G. A. Somorjai, Surf. Sci. 71, 519 (1978).

8. R. J. Baird, R. C. Ku and P. Wynblatt, Surf. Sci. 97, 346 (1980).

9. D. G. Castner and G. A. Somorjai, Surf. Sci. 83, 60 (1979).

10. L. H. Dubois, P. K. Hansma and G. A. Somorjai, J. Catal. 65, 318 (1980).

11. F. Solymosi and J. Sarkany, Appl. Surf. Sci. 3, 68 (1979).

12. M. L. Unland, J. Catal. 31, 459 (1973).

13. S. De Cheveigne, S. Gauthier and J. Klein, Surf. Sci. 114, L21 (1982).

14. H. Arai and H. Tominaga, J. Catal. 43, 131 (1976).

15. V. Rives-Arnau and G. Munuera, Appl. Surf. Sci. 6, 122 (1980).

16. M. Shelef, Catal. Rev.-Sci. Eng. 11, 1 (1975).

17. G. Broden, T. N. Rhodin, C. Brucker, R. Benbow and Z. Hurych, Surf. Sci. 59, 593 (1976).

18. E. Miyazaki and I. Yasumori, Surf. Sci. 57, 755 (1976).

19. J. B. Benziger, Appl. Surf. Sci. 6, 105 (1980).

20. L. H. Dubois and G. A. Somorjai, Surf. Sci. 91, 514 (1980).

21. F. Solymosi and A. Erdohelyi, Surf. Sci. 110, L630 (1981).

22. R. M. Kroeker, W. C. Kaska and P. K. Hansma, J. Catal. 57, 72 (1979).

23. C. T. Campbell, S. K. Shi and J. M. White, Appl. Surf. Sci. 2, 382 (1979).

24. C. T. Campbell and J. M. White, J. Catal. 54, 289 (1978).

25. L. H. Dubois, J. Chem. Phys. 77, 5228 (1982).

26. P. A. Thiel, E. D. Williams, J. T. Yates and W. H. Weinberg, Surf. Sci. 84, 54 (1979).

27. R. J. Koestner, M. A. Van Hove and G. A. Somorjai, Surf. Sci. 107, 439 (1981).

28. J. T. Yates, E. D. Williams and W. H. Weinberg, Surf. Sci. 91, 562 (1980).

29. D. G. Castner, L. H. Dubois, B. A. Sexton and G. A. Somorjai, Surf. Sci. 103, L134 (1981).

30. J. T. Yates, E. D. Williams and W. H. Weinberg, Surf. Sci. 115, L93 (1982).

31. R. A. Marbrow and R. M. Lambert, Surf. Sci. 67, 489 (1971).

32. V. V. Gorodetskii and B. E. Nieuwenhuys, Surf. Sci. 105, 299 (1981).

33. P. A. Thiel, J. T. Yates, Jr. and W. H. Weinberg, Surf. Sci. 82, 22 (1979).

34. L. H. Dubois and G. A. Somorjai, Surf. Sci. 88, L13 (1979).

35. V. J. Mimeault and R. S. Hansen, J. Phys. Chem. 70, 3001 (1966).

36. G. C. Bond, Catalysis by Metals (Academic Press, Inc., London, 1962), p. 373.

37. H. Wise and M. F. Frech, J. Chem. Phys. 20, 22 (1952).

38. E. R. S. Winter, J. Catal. 22, 158 (1971).

39. E. R. S. Winter, J. Catal. 34, 440 (1974).

40. T. P. Kobylinski and B. W. Taylor, J. Catal. 33, 376 (1974).

41. K. C. Taylor, in The Catalytic Chemistry of Nitrogen Oxides, edited by R. L. Klimisch and J. G. Larson (Plenum Press, New York, 1975), p. 173.

42. H. S. Gandhi and M. Shelef, J. Catal. 40, 312 (1975).

43. K. C. Taylor and R. L. Klimisch, J. Catal. 30, 478 (1974).

44. T. Iizuka and J. Lunsford, J. Molec. Cat. 8, 391 (1980).

45. M. F. Brown and R. D. Gonzalez, J. Catal. 44, 477 (1976).

46. F. Solymosi, L. Volgyesi and J. Sarkany, J. Catal. 54, 336 (1978).

47. S. Dushman, Scientific Foundations in Vacuum Techniques, edited by J. M. Lafferty (John Wiley & Sons, New York, 1962), 2nd edition.

48. R. G. Musket, W. McLean, C. A. Colmenares, D. M. Makowiecki and W. J. Siekhaus, Appl. Surf. Sci. 10, 143 (1982).

49. E. E. Quick, Ph.D. Thesis, Iowa State University, 1979 (unpublished).

50. K. C. Taylor and J. C. Schlatter, J. Catal. 63, 53 (1980).

51. P. A. Zhdan, G. K. Boreskov, A. I. Boronin, A. P. Schepelin, W. F. Egelhoff, Jr. and W. H. Weinberg, Appl. Surf. Sci. 1, 25 (1977).

52. C. M. Comrie, W. H. Weinberg and R. M. Lambert, Surf. Sci. 57, 619 (1976).

53. R. Ku, N. A. Gjostein and H. P. Bonzel, Surf. Sci. 64, 465 (1977).

54. A. Vavere, Ph.D. Thesis, Iowa State University, 1979.

55. A. Vavere and R. S. Hansen, J. Catal. 69, 158 (1981).

56. S. Semancik, G. L. Haller and J. T. Yates, Appl. Surf. Sci. 10, 546 (1982).

57. R. Bouwman, J. B. van Mechelen and A. A. Holscher, J. Vac. Sci. Technol. 15, 91 (1978).

58. L. E. Davis, N. C. MacDonald, P. W. Palmberg, G. E. Riach and R. E. Weber, Handbook of Auger Electron Spectroscopy (Physical Electronics Division of Perkin-Elmer, Inc., Eden Prairie, Minnesota, 1976).

59. P. A. Redhead, Vacuum 12, 203 (1962).

60. C. N. Satterfield, Heterogeneous Catalysis in Practice (McGraw-Hill, New York, 1980), Chap. 3.

61. T. Iizuka and J. Lundsford, J. Molec. Cat. 8, 391 (1980).

62. J. R. Hardee, Ph.D. Thesis, Rice University, 1978.

63. K. H. Haskell and R. E. Jones, Brief Instructions for Using the Sandia Mathematical Subroutine Library (Sandia National Laboratory, Albuquerque, New Mexico, 1978), Report No. SAND77-1441, Chap. 8.

64. A. W. Adamson, Physical Chemistry of Surfaces (John Wiley & Sons, New York, 1976), Chap. 15.

65. H. Ibach and S. Lehwald, Surf. Sci. 76, 1 (1978).

66. J. L. Gland and B. A. Sexton, Surf. Sci. 94, 355 (1980).

ACKNOWLEDGEMENTS

The author would like to express sincere appreciation to Dr. Robert S. Hansen for his guidance and support during his graduate school career. The author especially appreciates the numerous discussions concerning the development of this research project, and of scientific research in general.

Sincere appreciation is extended to the countless number of professors, graduate student associates, and numerous technicians for a vast amount of invaluable advice and assistance. The author would like to especially thank Lesley Swope for the typing of this dissertation.

The author would like to thank his parents, sisters, and brother for their never ending encouragement and support during his graduate and undergraduate years. Finally, the author would like to thank his wife, Shelley, for her overwhelming amount of patience, encouragement, and support during his graduate school years.

APPENDIX

Table 3. Experimental steady-state kinetic data measured for the nitric oxide order plot on Rh(100) at 688 K, with P_{CO} = 44.0 Pa

P_{NO} Pa	Rate x 10^{-14} molec/cm^2 sec	P_{NO} Pa	Rate x 10^{-14} molec/cm^2 sec	P_{NO} Pa	Rate x 10^{-14} molec/cm^2 sec
1.64	1.98	8.92	17.3	86.8	93.1
1.65	1.99	12.0	39.0	86.8	96.4
1.73	2.03	12.1	37.2	143.0	92.3
2.96	3.83	12.2	38.7	143.3	88.6
3.00	3.17	19.8	77.6	348.5	70.1
3.05	3.77	19.9	78.5	348.7	82.3
3.05	3.72	20.0	70.0	348.8	79.2
3.06	3.86	32.6	90.0	589.0	65.9
3.19	4.12	32.7	76.6	589.6	57.2
4.58	7.08	32.7	88.1	589.6	64.2
4.68	7.79	32.8	82.4	980.8	37.5
4.71	8.25	32.8	75.7	982.0	37.4
8.84	15.4	52.9	90.5	982.0	39.6
8.87	15.7	53.0	90.3	1644.5	17.8

Table 4. Experiental steady-state kinetic data measured for the carbon monoxide order plot on Rh(100) at 688 K, with P_{NO} = 57.5 Pa

P_{CO} Pa	Rate x 10^{-15} molec/cm^2 sec	P_{CO} Pa	Rate x 10^{-15} molec/cm^2 sec	P_{CO} Pa	Rate x 10^{-15} molec/cm^2 sec
0.99	1.94	7.40	9.54	32.7	9.61
1.11	2.30	7.45	9.35	32.7	10.23
1.13	2.75	7.46	8.96	32.8	9.24
1.68	3.81	12.0	8.38	53.8	8.71
1.80	4.04	12.1	9.09	53.9	8.55
1.83	4.08	12.1	9.54	53.9	8.69
2.71	5.55	19.7	8.96	88.5	7.71
2.79	5.34	19.7	9.65	88.7	8.10
2.84	5.15	19.8	8.83	88.7	7.71
4.37	6.88	19.9	9.86	146.1	4.81
4.41	6.66	20.2	9.87	146.3	5.12
4.45	6.58	32.4	9.12	146.3	5.10
4.60	8.54	32.6	9.51	146.5	5.30
7.30	9.83	32.6	9.64	240.8	2.71
7.33	8.26	32.6	9.06	241.0	2.75
7.38	8.89	32.7	9.04		